Helium droplets in intense laser fields studied with XUV fluorescence spectroscopy

Dissertation
zur Erlangung des Doktorgrades
an der Fakultät für Mathematik, Informatik und Naturwissenschaften
Fachbereich Physik
der Universität Hamburg

vorgelegt von

Malte Sumfleth

Hamburg

2023

Gutachter/innen der Dissertation:	Priv. Doz. Dr. habil. Tim Laarmann Prof. Dr. Markus Drescher
Zusammensetzung der Prüfungskommission:	Priv. Doz. Dr. habil. Tim Laarmann Prof. Dr. Markus Drescher Prof. Dr. Franz Xaver Kärtner Dr. Michael Martins Prof. Dr. Daniela Pfannkuche
Vorsitzende/r der Prüfungskommission:	Prof. Dr. Daniela Pfannkuche
Datum der Disputation:	01.11.2023
Vorsitzender Fach-Promotionsausschuss PHYSIK:	Prof. Dr. Günter H. W. Sigl
Leiter des Fachbereichs PHYSIK:	Prof. Dr. Wolfgang J. Parak
Dekan der Fakultät MIN:	Prof. Dr.-Ing. Norbert Ritter

Eidesstattliche Versicherung / Declaration on oath

Hiermit versichere ich an Eides statt, die vorliegende Dissertationsschrift selbst verfasst und keine anderen als die angegebenen Hilfsmittel und Quellen benutzt zu haben.

Hamburg, den April 1, 2023

Unterschrift des Doktoranden

Zusammenfassung

Im Rahmen dieser Arbeit wurde die XUV-Fluoreszenzspektroskopie verwendet, um die Energieabsorption und Dissipation in laser-getriebenen Helium-Nanoplasmen in der Wechselwirkung mit intensiven Infrarot-Laserpulsen zu untersuchen. Im Gegensatz zu typischen Plasmen aus atomarem Helium, erlaubt die Clusterumgegebung die energetische Abregung auch mittels Dreikörper-Rekombination im Nanoplasma. Der Anteil der Dreikörperrekombination nimmt zu, je besser die Bedingungen für resonantes Heizen des Nanoplasmas erfüllt sind. Dies wurde für Cluster und große Helium-Tropfen mit einer durchschnittlichen Größe zwischen 1.2×10^5 Atomen and 1.6×10^{10} Atomen vermessen. Bei Verwendung der größten Cluster mit einer Durchschnittsgröße oberhalb von 2.6×10^9 Atomen und 180 fs langen Pulsen wird erstmals ein extrem breitbandiges XUV Cluster Kontinuumsspektrum beobachtet. Das neuartige Kontinuumssspektrum erstreckt sich von einer Photonenenergie von 21 eV bis hin zu 70 eV, wobei diese Angaben durch die maximale Wellenlängenempfindlichkeit des verwendeten Spektrometers limitiert sind. Bei Verwendung deutlich kürzerer Pulse bei einer Zentralwellenlänge von 2060 nm mit einer Pulsdauer von nur 50 fs tritt dieses Kontinuumsspektrum bereits bei deutlich kleineren Clustern ab einer durchschnittlichen Größe von 7.5×10^6 Atomen auf. Die Hypothese ist, dass das Kontinuum auf einer Zeitskala kürzer als die Pulslänge des Treiberlasers und damit innerhalb eines relativ intakten Clusters generiert wird.

Abstract

In this work, XUV fluorescence spectroscopy was used to study energy absorption and dissipation in laser-driven helium nanoplasms interacting with intense infrared laser pulses. In contrast to typical plasmas of atomic helium, the cluster environment allows energetic de-excitation by means of three-body recombination in the nanoplasma. The amount of three-body recombination increases the better the conditions for resonant heating of the nanoplasma are met. This was measured for clusters and large helium droplets with an average size between 1.2×10^5 atoms and 1.6×10^{10} atoms. Using the largest clusters with an average size above 2.6×10^9 atoms and 180 fs long pulses, an extremely broadband XUV cluster continuum spectrum is observed for the first time. The novel continuum spectrum ranges from a photon energy of 21 eV to 70 eV, although these figures are limited by the maximum wavelength sensitivity of the spectrometer used. Using much shorter pulses at a central wavelength of 2060 nm with a pulse duration of only 50 fs, this continuum spectrum already appears in much smaller clusters starting at an average size of 7.5×10^6 atoms. The hypothesis is that the continuum is generated on a time scale shorter than the pulse length of the driving laser and thus within a relatively intact cluster.

Contents

Chapter 1

Introduction

The interaction of nanoparticles with strong laser fields has enjoyed tremendous attention from researchers throughout the last couple of decades [1, 2, 3, 4]. Numerous studies have investigated energy deposition and redistribution processes in atomic and molecular clusters situating them between atoms and bulk matter with dimensions down to a few nanometers. Using cluster beams as a target material combines the advantages of solid state density of individual particles with low target density in the laser-matter interaction volume. This experimental scheme creates well-defined conditions for studying the energetics and dynamics of nanoplasma formation and its relaxation across a large range of excitation energies from the infrared (IR) with laser wavelengths $\lambda > 1\,\mu$m [5], across the vacuum ultraviolet (VUV) [6, 7, 8, 9] and extreme ultraviolet (XUV) spectral range [10, 11] towards hard x-rays with wavelengths $\lambda < 10$ nm [12, 13].

Massive electron excitation and ionization generates a deep mean-field potential on the order of keV energy confining the plasma electrons. Incredible electron temperatures are reached via different energy absorption mechanisms of the quasifree plasma electrons, which mainly depend on the laser pulse parameters and the cluster size. Efficient energy deposition results in the ejection of hot electrons [14], highly charged [15] and energetic ions [16], as well as x-ray emission from the nanoplasma [17]. Even nuclear fusion reactions from explosions of femtosecond laser-heated deuterium clusters have been observed experimentally [18].

The optimization of secondary electron, ion, x-ray or pulsed neutron sources towards applications requires detailed knowledge on the evolution of the electronic properties of matter in the expanding nanoplasma driven by the Coulomb forces of ions and the hydrodynamic pressure of hot electrons. Experimental studies flanked by theoretical calculations show that electron thermalization to the bottom of the plasma potential is fast. It takes place on a femtosecond timescale due to the bulk-density conditions and is accompanied by isotropic emission of low-energy (thermal) electrons [19]. During the nanoplasma expansion the binding en-

ergy of the quasifree electrons gradually shifts upwards forming a delocalized energy band close to the ionization continuum. In this phase, electron-correlation-driven energy transfer processes have to be considered [20]. In parallel, because of the mean-field potential upshift and the resulting increase in the interatomic Coulomb barriers, localized states of individual He^{2+} ions recover in case of fully ionized He nanoplasma [21]. Thereby, various additional energy relaxation channels open-up triggered by quasifree electron-ion recombination processes on the picosecond to nanosecond time scale including radiative decay. This is where **the present fluorescence spectroscopy study comes into play to shed light on energy redistribution in laser-generated nanoplasma** [22].

Different types of recombination pathways are discussed in the literature [23]. In radiative recombination an electron recombines with an ion and its excess energy is released as a photon. Three-body recombination (TBR) processes involve two electrons and one ion. One of the two electrons recombines with the ion, while the other electron takes away the excess energy of the first electron. Dielectric recombination describes a variant, where the excess energy is taken up by a second electron already present in the ion, which gets lifted into an electronically excited state. Subsequently, the excited electron relaxes back into its ground state via radiative or Auger-decay. Noting in passing that there exist more complicated recombination processes, such as radiative dielectric recombination, where the radiative decay of the excited electrons happens simultaneously with the initial recombination. In this thesis, the focus lies on radiative recombination and three-body recombination, because the object of study is the recombination of quasifree electrons with He^{2+} forming He^{+} in the He nanoplasma evolution. Here, no other electrons exist in the ion that could participate in dielectric recombination or more complicated processes.

Investigations of the three-body recombination process started back in the 1960s [24] and resulted in the formulation of the so-called classical "bottle neck" model. The defining features of this model are: (a) the temperature dependence for the total recombination rate, which scales as $\propto T^{-9/2}$, and (b) the electronic state n' most likely being populated, because its ionization energy is comparable to the kinetic energy of the thermal quasifree electrons ($E_{n'} \propto k_B T$). However, for a "cold" plasma ($T < 1000\,\mathrm{K}$) the bottle neck model no longer applies. It neglects quantum effects, such as the increased de Broglie wavelengths of thermal electrons at the bottom of the plasma potential, which enhances the recombination probability and allows for the population of states with ionization energies significantly lower than the bottle neck prediction. Furthermore, in a low-temperature plasma high l-states of the same n are populated much more frequently compared to the bottle neck regime, where manly low l-states get populated as outlined in [25]. In the present work, I have applied XUV fluorescence spectroscopy to gain information on laser-generated helium nanoplasma dynamics. In agreement with previous studies

the experimental results underline the important role of three-body recombination processes in the energy dissipation during the helium nanoplasma expansion. The fluorescence data provide evidence that the population of electronically excited He^+ states in the transient nanoplasma follows the bottle neck model. Further insight is gained by comparing the fluorescence data recorded after ionizing the nanoplasma with laser pulses of 180 fs duration and 1030 nm central wavelength with data obtained with laser pulses of 50 fs duration and 2060 nm central wavelength. Despite both experimental scenarios belonging to the IR-regime of nanoplasma ignition, we find marked differences in the energetics and dynamics of laser-generated helium nanoplasmas.

Chapter 2

Theoretical Overview

2.1 Cluster formation

Generating helium clusters is a straightforward process. Helium gas with a purity $> 99.9999\%$ is kept inside the coldhead of a cryostat at a pressure P_0 and a stagnation temperature T_0 and is only allowed to leave the coldhead through a small nozzle (here of 5 µm diameter) into the vacuum chamber. There it adiabatically expands into the vacuum. Despite this simple procedure, helium shows rich dynamics that lead to the appearance of fundamentally different regimes of cluster formation, as a function of P_0 and T_0. The regimes can be best understood by looking at the pressure-temperature phase diagram of ^{4}He as displayed in Figure 2.1:

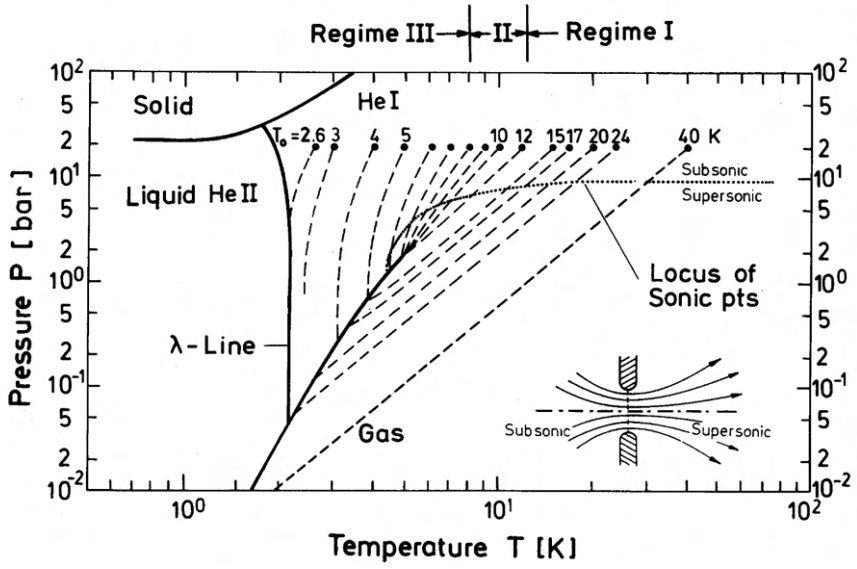

Fig. 2.1: Pressure-temperature phase diagram of ^{4}He with isentropes (- - -) for nozzle beam parameters starting from a stagnation pressure of $P_0 = 20\,\text{bar}$ and a range of temperatures T_0. The locus of sonic points (...) specifies the states of helium upon leaving the orifice. Taken from [26]

As can be seen in Figure 2.1, there are three regimes of cluster generation. In Regime I ($P_0 = 20\,\text{bar}$, $T_0 > 10\,\text{K}$) the dynamic is dominated by a simple gas-like

behaviour. Here, the helium gas simply cools down adiabatically until its isentrope reaches the gas-liquid separation line from the gas side and cluster generation starts by aggregation of individual atoms. In Regime II ($P_0 = 20\,\text{bar}$, $10\,\text{K} > T_0 > 8\,\text{K}$) the isentropes get close to the critical point ($T_C = 5.2\,\text{K}$, $P_C = 2.3\,\text{bar}$). This can lead to unusual behavior, since the correlation length becomes macroscopically large resulting in fluctuations in particle density [26]. In Regime III ($T_0 < 8\,\text{K}$) the isentropes all cross the phase separation line from the liquid side resulting in the liquid helium fragmenting into droplets due to cavitation and flashing. For temperatures $T_0 > 6\,\text{K}$ the locations of the sonic points in Figure 2.1 are downstream from the nozzle opening, while for temperatures $T_0 < 6\,\text{K}$ the expansion already becomes sonic within the nozzle and at even lower temperatures the helium reaches the phase separation line before leaving the nozzle. The result of that later scenario is the creation of an unstable liquid helium jet, which proceeds to break apart into individual droplets due to Rayleigh-instabilities. At the lowest temperatures $T_0 < 5\,\text{K}$ the emitted liquid jet becomes stable and only evaporation limits its lifetime.

2.2 Theoretical description of clusters

In order to understand and predict the energetics and dynamics of laser-cluster interactions, one has to employ a theoretical model for describing the cluster and its atomic constituents. Ideally, one utilizes a complete quantum mechanical description by solving the full time-dependent Schrödinger equation. However, such a model is not practically applicable to clusters, since the large number of involved ions and electrons result in computation requirements far exceeding current available performance. As such the cluster community has developed a hierarchy of models for describing cluster behavior [3]. Along this hierarchy subsequent models trade the capability to describe more minute and microscopic effects for reduced computational requirements, which allows the description of larger clusters exposed to strong laser fields.

2.2.1 The Hierarchy of models

For the smallest clusters one can utilize *ab initio* models such as configuration interaction or multi-configurational time-dependent Hartree-Fock approaches. Methods such as these can work with systems of a few tens of particles in a single clusters.

The simplification one performs in order to increase the maximum particle number is the elimination of the details due to many-body correlations and their impact in the form of an effective interaction acting on single-particle states. This leads to the time-depended density functional theory usually by coupling it with molecular

dynamics for the description of the ionic part of the cluster [27, 28, 29]. The size limits of such a model are clusters consisting of a few hundred atoms, which again require too much computational effort to describe strong excitations, since such a model neglects dynamical correlations caused by electron-electron collisions.

In order to address the needs of even larger systems, one next simplifies the orbital description of electrons by switching to a semi-classical model dealing with a one-body electron distribution or electron density and local currents. The loss of quantized electron structure and possible interference effects is often offset by the fact that for larger systems with narrow energy levels and higher excitations these effects have diminished importance. Models that employ this procedure are the Vlasov model and the Vlasov-Uehling-Uhlenbeck schemes [30, 31, 32].

The second to last step in this hierarchy is occupied by techniques employing classical molecular dynamics [33, 34, 35, 36, 37]. Here, both ions and free electrons are described via classical trajectories taking into account the classical field and many-particle correlations. Bound electrons are not explicitly propagated and ionization of them is treated via known barrier-suppression and above-threshold ionization rates. Such models can handle clusters with up to 10^6 particles and even treat the effects of high excitation levels induced by strong laser fields.

Finally, one resorts to rate equations and the so-called nanoplasma model [38, 39] to describe the largest and most highly excited clusters. Here, the irradiated clusters are assumed to be a quasi homogeneous plasma due to rapid ionization. This plasma is described by average values such as as temperature, density, radius, charge state of the ions and ionization rate.

The nanoplasma model applies to the vast majority of this work, since most of the clusters considered are too large to be efficiently described by any of the other methods.

2.3 Energy absorption by clusters

One of the characteristic features of clusters irradiated by laser light is their enormous ability to absorb energy from the light field. In order to understand this phenomena, we start by looking at the prevailing ionization pathways of atoms, molecules and larger condensed matter systems. Afterwards, we illuminate the prevailing mechanisms in clusters that allow ionized plasma electrons to further absorb photons.

2.3.1 Ionization

The basis for cluster ionization is built from processes known from atomic systems. The simplest procedure is of course the absorption of a single photon with an energy

larger than the ionization potential of the bound electron: $\hbar\omega_{ph} > E_{IP}$. This ionization path exists, when one uses XUV-light sources to irradiate the clusters as many studies did before [40, 41, 42]. Here, we employ infrared lasers, whose photons lack the necessary energy for single-photon ionization of helium atoms. The next step are multi-photon ionization (MPI) processes, where the energy of multiple photons is used together to ionize a single electron. Typical of MPI is that electrons can continue to absorb photons even beyond the number necessary to lift the electron into the continuum. Electrons emitted by this process commonly referred to above-threshold ionization (ATI) have multiple possible energies after ionization, each of which is separated by the energy of one additional absorbed photon. The process is displayed in Figure 2.2 a). Beyond MPI, there exists also optical-field ionization (OFI). This process can no longer be described by a pertubative model with countable number of photons as is the case for MPI. Instead, the electric field strength of the laser light is sufficient to bend the electrostatic potential of the nucleus. This allows electrons to tunnel out of their bound energy levels (see Figure 2.2 a)). The ionization rate for this mechanism is given by the Ammosov-Delone-Krainov (ADK) theory [43]. A sufficiently strong electric field is even capable of completely suppressing the potential barrier that keeps electrons in their atomic orbitals. The necessary intensity for barrier-suppression ionization (BSI) beyond which BSI takes place can be calculated according to the formula:

$$I_{BSI=} = \frac{\pi^2 c \epsilon_0^3 E_{IP}^4}{2e^6 q^2} = 4 \cdot 10^9 \frac{(E_{IP}[eV])^4}{q^2} [\frac{\mathrm{W}}{\mathrm{cm}^2}] \tag{2.1}$$

While the transition between MPI and OFI is characterized by the Keldysh-parameter [44]:

$$\gamma = \sqrt{\frac{E_{IP}}{2U_p}} \tag{2.2}$$

This parameter compares the ionization potential with the maximum kinetic energy $2U_p$ of an electron freely moving in the electric field of the laser. For $\gamma \leq 1$ OFI is dominant, since the energy of a free electron is comparable or larger than the binding energy of a bound electron. For $\gamma \gg 1$ MPI is the prevailing ionization process.

The first ionization mechanism one encounters when considering the case of more then a single atom is called charge- resonance-enhanced ionization (CREI) [45, 46]. Here, the interplay of the stark-shifted potentials of two atoms that are the right distance apart results in an increased ionization rate (see Figure 2.2 b)). This effect has also been observed for clusters much smaller than the ones considered in this work and is not expected to play a mayor role here. In order to properly describe ionization dynamics for clusters consisting of more than a few atoms, we have to split the ionization process into so-called inner and outer ionization [34]. The reason

is that after each electron leaving the cluster the net electric charge of the entire cluster increases by one elemental charge e. This leads to a stronger cluster potential that an electron would need to overcome in order to leave the cluster as a whole. This step is called the outer ionization. However, even in the case of a cluster potential too large to be overcome and therefore no more outer ionization taking place, inner ionization, where electrons get ionized from their bound orbitals around single atoms can still proceed. Electrons that were inner-ionized but can no longer be outer-ionized by the laser are called "quasifree" since they are no longer bound by their parent atom, but are still confined to the overall cluster. The electron populations, their relative energy states and the population transfer via inner and outer ionization is displayed in Figure 2.2 c).

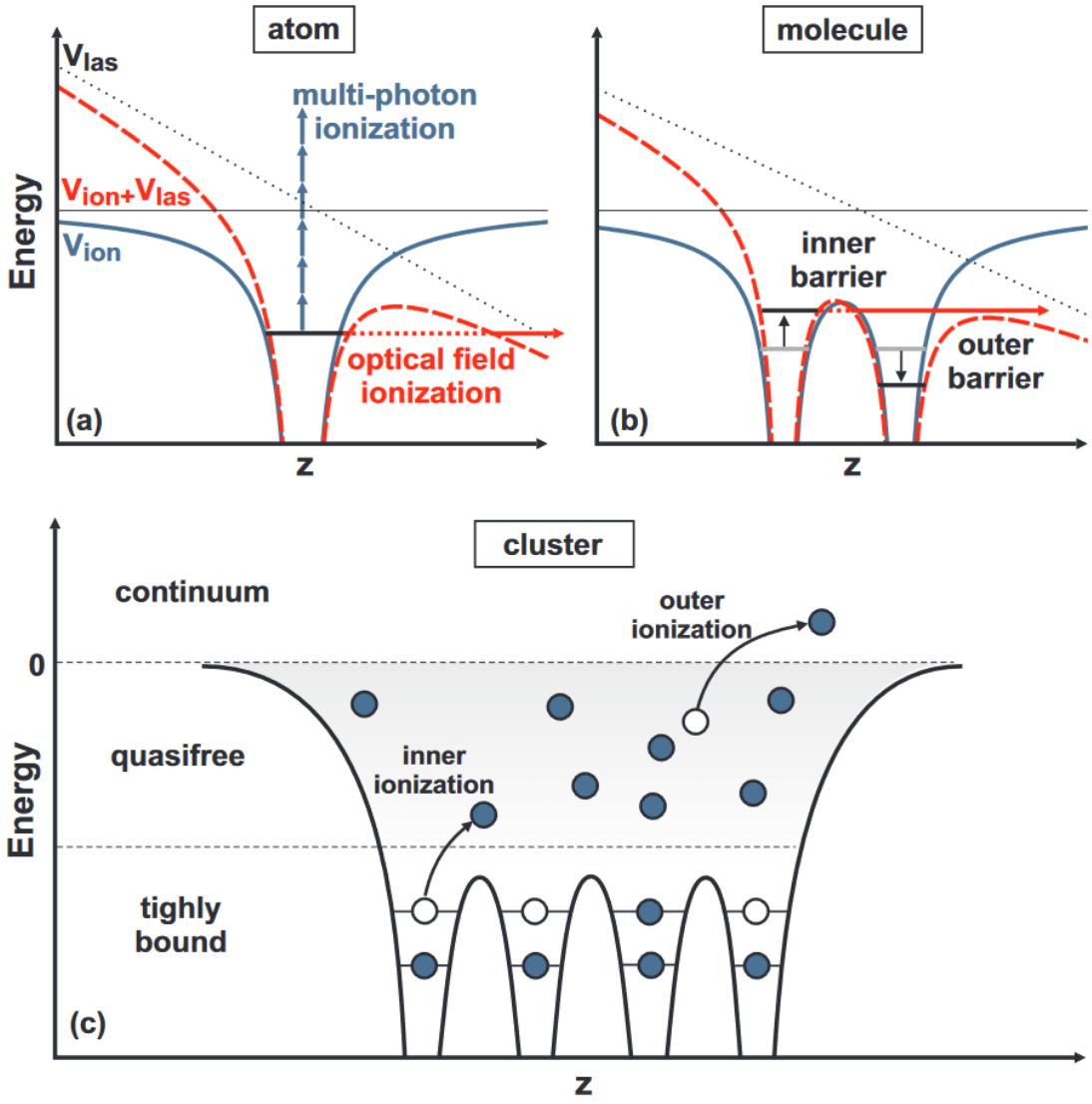

Fig. 2.2: Schematics showing the potential of the ion V_{ion}, the potential of the laser light added to the ion potential $V_{ion}+V_{las}$. a) shows the atomic case with both the multi-photon ionization and optical-field ionization pathways drawn as well. b) depicts the situation of the CREI mechanism in the case of a dimer of two atoms. c) draws the three populations of electrons (bound, quasifree and continuum), as well as the transfer between them via inner and outer ionization. Taken from [3]

The quasifree electrons can contribute to additional ionization events, since they stay in a high density centered around the cluster ion core, while continuing to absorb laser radiation. While they are accelerated due to the laser field, they transfer some of their kinetic energy to bound electrons via electron-impact ionization. This can lead to a positive feedback loop, where quasifree electrons inner ionize bound electrons, which become quasifree, which in turn add to the inner ionization rate due to increasing electron-impact ionization [33].

2.3.2 Heating mechanisms

After inner ionization, electrons continue to capture energy from the laser field and convert it into heat. The baseline for this process is inverse bremsstrahlung (IBS) [47]. The simplest case involves a single electron, ion and photon, all of which are embedded in the plasma environment. The heating rate per electron (dE/dt) is in this case:

$$\left\langle \frac{dE}{dt} \right\rangle_{IBS} = 2U_p \frac{\tau_{coll}\omega_{las}^2}{\tau_{coll}^2\omega_{las}^2 + 1} \tag{2.3}$$

with U_p the ponderomotive potential of the laser field, τ_{coll} the collisional relaxation time of the plasma and ω_{las} the angular frequency of the laser field. Since in the present work we will look at highly ionized clusters, we have to extend this model to account for collective motions of the quasifree electrons. This collective oscillation can be modeled via a surface plasmon called the Mie-Plasmon [48] with a given angular frequency $\omega_{Mie} = e(4\pi\epsilon_0 m_e r_s^3)^{-1/2}$ with e the elementary charge, ϵ_0 the vacuum permittivity, m_e the mass of the electron and r_s the Wigner-Seitz radius. Adding its effect to the above formula we obtain:

$$\left\langle \frac{dE}{dt} \right\rangle_{IBS} = 2U_p \frac{\tau_{coll}\omega_{las}^4}{\tau_{coll}^2(\omega_{Mie}^2 - \omega_{las}^2)^2 + \omega_{las}^2} \tag{2.4}$$

This formula encapsulates the important behavior that the addition of collective electron motion imprints onto the heating rate. First of all, in the case $\omega_{las} \gg \omega_{Mie}$ the formula simplifies back into the case of a single electron moving against the ionic background. Here, collective motion is negligibly small. In the second case of $\omega_{las} \ll \omega_{Mie}$ collective oscillations completely dominate the heating rate via IBS and for $\omega_{las} = \omega_{Mie}$ we see a spike in the heating rate caused by the collective oscillations being in resonance with the driving laser frequency [49, 50].

2.3.3 Cluster disintegration

Once ionization begins the irradiated cluster will also begin to expand. Two separate forces act on the cluster that increase its size. The first one is of hydrodynamic

nature. The high temperature of the electron part of the nanoplasma during the laser pulse interaction and afterward will push the electron density outwards. The negative charge density will then tug the positively charged ions along, which increases the overall cluster radius. Later on, the electrons thermalize with the ions, after which the expansion is driven by the ion temperature. The second force is a Coulomb explosion. Here, the laser driven outer ionization causes the overall charge of the cluster to become more and more positive. This of course leads to stronger and stronger repellent action between the ions pushing them further away and therefore increasing the cluster size.

For this work, the interplay of cluster expansion and electron heating rate is important. Because the cluster size increases, the Mie frequency ω_{Mie} continuously drops and transiently matches the laser frequency ω_{las}. During this resonance phase the cluster absorbs laser radiation extremely efficiently and rapidly heats up further, which in turn accelerates its expansion rate. The dynamic is displayed in Figure 2.3, where the expansion was simulated for argon clusters of 100-Å size after being subjected to 130 fs long pulses with 825 nm central wavelength. Here, one clearly sees how the expansion of the cluster is initially slow but steadily accelerating as the electron temperature rises during the laser pulse interaction. Once the initial electron density has dropped to the critical density, the resonant heating sets in (IBS), electron temperature and expansion rate increase tremendously.

There are two possible experimental scenarios to probe the resonant heating condition. In the first, the laser pulse that has a duration shorter than the time needed for the cluster to expand enough to meet the $\omega_{Mie} = \omega_{las}$ condition is stretched in time via placing additional dispersing elements in the optical beam path. Once the pulse duration is sufficiently long to include the point in time of resonant heating, one measures significantly increased electron temperatures or ion kinetic energies. This method is experimentally simple to implement, but the reduction in peak intensity leads to additional changes to the dynamics that need to be carefully separated from the resonant heating effect under investigation. To remedy this, the second method utilizes two individual pulses that are separated in time by a variable delay. The first pulse initiates ionization, heating and expansion. The second pulse then probes the conditions after a chosen time delay. If at the certain time the resonance condition is met, the resulting temperatures and energies far exceed those measured with different delays between the pulses, without the influence of changes in overall peak intensity.

After the laser pulse has passed the cluster and any heating dynamics have stopped, the expansion of the cluster still continues. This leads to a steady reduction in the temperature of the electrons due to adiabatic cooling. Eventually, the electron temperature has dropped far enough that electron-ion recombination sets in.

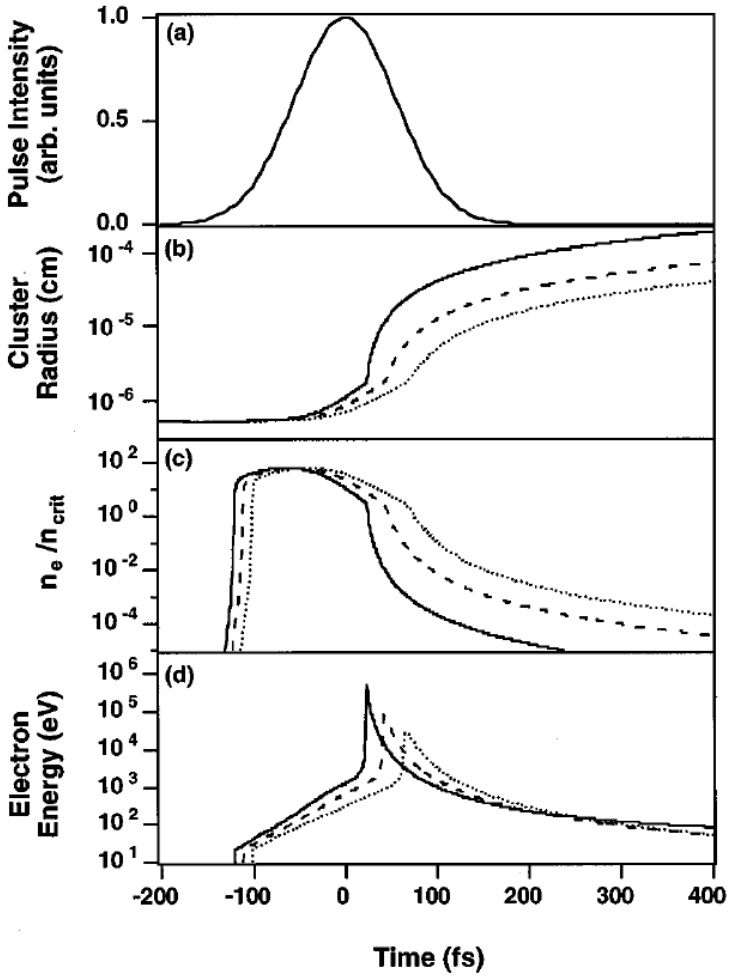

Fig. 2.3: Simulation of nanoplasma parameters for 100-Å argon clusters that are irradiated by 130 fs long pulses with a central wavelength of 825 nm at three different peak intensities: 0.5×10^{16} W/cm^2(dotted line), 1.0×10^{16} W/cm^2(dashed line) and 2.0×10^{16} W/cm^2(solid line). Displayed are: in a) the pulse intensity envelope, in b) the cluster size, in c) the ratio between electron density and critical density $n_{crit} = 1.6 \times 10^{21}$ cm^{-3} at which $\omega_{Mie} = \omega_{las}$ and in d) the energy of the ionized electrons. Taken from [38]

2.3.4 Recombination in a helium nanoplasma

Recombination describes the process by which free or quasifree electrons in a plasma recombine with an ion to form an atom or ion with reduced charge. In general, four types of recombination pathways are considered. The first one is radiative recombination. Here, an electron recombines with an ion and its excess energy is released as a photon. The second pathway is that of three-body recombination (TBR). This pathway involves two electrons and an ion. One of the two electrons recombines with the ion, while the other electron takes away the excess energy of the first electron. The third process is called dielectric recombination. Here, an electron recombines with an ion and its excess energy is taken up by a second electron already present in the ion, which gets lifted into an electronically excited state. Later on, the excited electron relaxes back into its ground state via radiative- or Auger-decay. The final energy dissipation pathway is a group of more complicated recombinations such as radiative dielectric recombination, where the radiative decay of the excited electrons happens simultaneously with the recombination, as well as other recombinations [51]. In the present work the focus is on the radiative recombination and three-body recombination, because the target is the recombination of quasifree electrons with He^{2+} forming He^{+}. Therefore, no other electrons exist in the ion that can participate in dielectric recombination or more complicated processes. In the following, we will look into radiative recombination and three-body recombination in more detail.

Radiative recombination

During radiative recombination a single electron recombines with an ion and releases its excess energy as a photon: $He^{2+} + e^{-} \rightarrow He^{+} + \gamma$. The theory by Stobbe et. al. [52] provides the distribution of n- and l-states that get populated by radiative recombination determined by the corresponding cross-sections. The results for the states of interest are tabulated in Table 2.1 with values for the recombination cross sections taken from [53].

Three-body recombination

During TBR an electron recombines with an ion and a second electron in the vicinity takes the excess energy away: $He^{2+} + 2e^{-} \rightarrow He^{+} + e^{-}$. Investigations of the TBR process started back in the 1960s [24] and resulted in the formulation of the classical "bottle neck" model. The defining features of this model are: (a) the temperature dependence for the total recombination rate, which scales as $\propto T^{-9/2}$, and (b) the electronic state n' most likely being populated, because its ionization energy is comparable to the kinetic energy of the thermal quasifree electrons ($E_{n'} \propto k_B T$).

n / l	0	1	2	3	4	5
1	1678					
2	491	1351				
3	248	770	891			
4	155	491	743	555		
5	108	345	569	611	335	
6	81.5	258	441	546	459	198

Tab. 2.1: The reduced radiative recombination cross section $(nE/Z^2E_0)\sigma_{nl}$ in units of $10^{-25}\,\mathrm{cm}^2$ is calculated in the limit of small electron energies according to theory of Stobbe. All data are taken from [53]

However, for a "cold" plasma ($T < 1000\,\mathrm{K}$) the bottle neck model no longer applies. It neglects quantum effects, such as the increased de Broglie wavelengths of thermal electrons at the bottom of the plasma potential, which enhances the recombination probability and allows for population of states with ionization energies significantly higher than the bottle neck prediction. Furthermore, in low-temperature plasma high l-states of the same n are populated much more frequently compared to the bottle neck regime, where manly low l-states get populated as outlined in [25].

2.4 Pulsed lasers

As described in the chapter above, the ionization step involves an electrical field strong enough to allow for tunnel ionization of individual atoms. This corresponds to intense light on the order of $10^{14}\,\frac{\mathrm{W}}{\mathrm{cm}^2}$ [43]. Such intensities can not be achieved by monochromatic "Continuous-Wave" (CW) lasers as shown by the following example: Let us assume we have a focus area of $A = 1\,\mu\mathrm{m}^2$. This would result in an required average power of the laser of $10^{14}\,\frac{\mathrm{W}}{\mathrm{cm}^2} \cdot A = 10^6\,\mathrm{W} = 1\,\mathrm{MW}$. This average power is orders of magnitude higher than what current CW-lasers are capable of delivering. As such, pulsed lasers have to be used to generate the helium nanoplasma, since they can reach the required intensity in the peak of their pulses, while showing a much smaller average power. The physics of laser pulses is briefly described in the following section.

2.4.1 General description

The electric field of a laser pulse as a function of time $E(t)$ can be written as $E(t) = A(t) \cdot e^{i(\omega_0 t + \phi(t) + \mathrm{CEP})}$. With $A(t)$ the envelope of the pulse, $\omega_0 t$ causing the oscillation of the electric field with the center frequency of the pulse ω_0, $\phi(t)$ the "temporal phase" and CEP being the "Carrier Envelope Phase". Such a pulse is displayed in Figure 2.4.

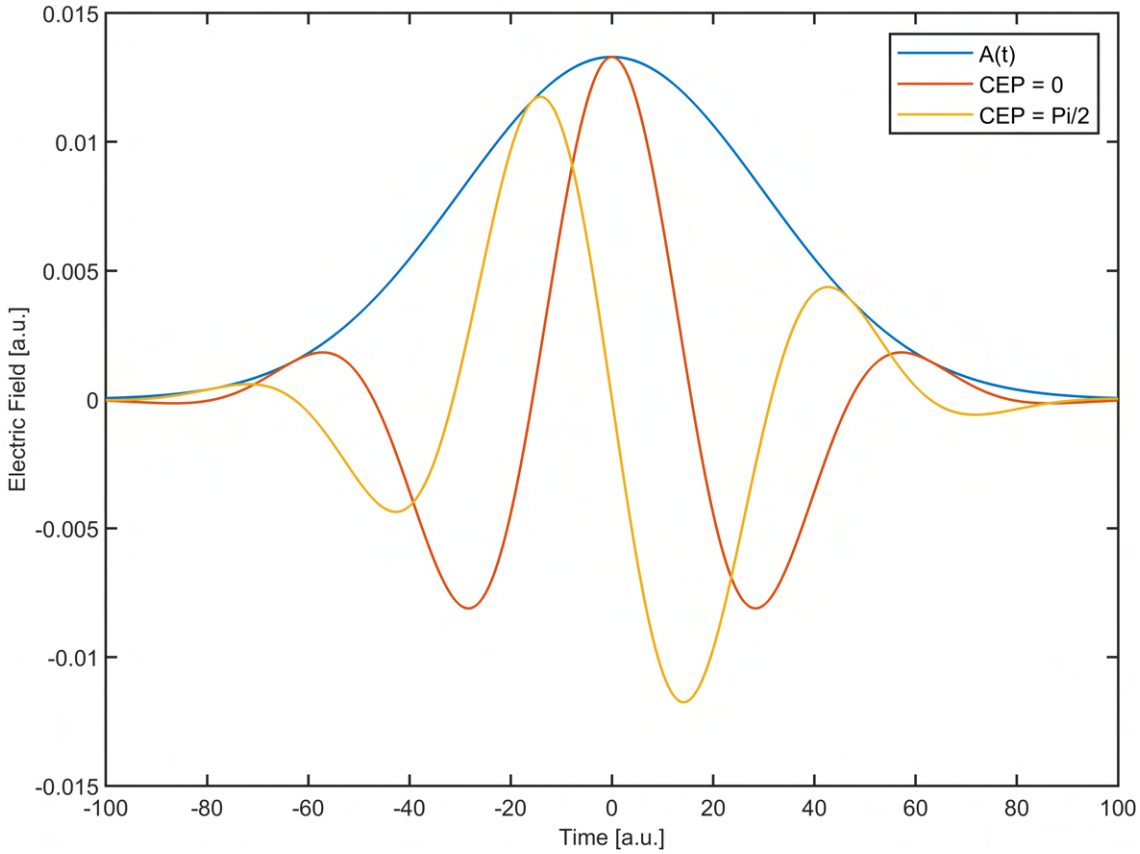

Fig. 2.4: Depiction of the carrier wave and its envelope $A(t)$ in blue. Underneath the electric field $E(t)$ with $\phi = 0$ and CEP $= 0$ in red and CEP $= \pi/2$ in orange.

As can be seen in Figure 2.4 the CEP introduces an offset between the maximum of the envelope and the center peak of the electric field distribution reducing the highest electric field strength in the pulse for any CEP value that is not an integer multiple of π. For pulses containing many oscillation of the electric field the CEP effect is negligible, while it can have dramatic effects on few-cycle pulses interacting with matter.

A complementary way of describing laser pulses is a formulation in the spectral domain. Such a description is of course linked to the time domain via the Fourier transformation $E(\omega) = \mathcal{F}(E(t))$. As such:

$$E(\omega) = A(\omega) \cdot e^{-i\Psi(\omega)} \tag{2.5}$$

With $A(\omega)$ being the spectral envelope and $\Psi(\omega)$ the spectral phase. $A(\omega)$ can be easily obtained for a given pulse, since its square $A(\omega)^2$ is the spectral intensity, which can be measured with a spectrometer. The spectral phase $\Psi(\omega)$ on the other hand is much harder to obtain experimentally, yet equally important for the generation of short pulses. Some spectral-phase retrival techniques exist [54, 55, 56], but those are not the focus of this work.

It is almost always more practical to describe the spectral phase not in its entirety,

but as a Taylor expansion resulting in:

$$\Psi(\omega) = CEP + GD \cdot (\omega - \omega_0) + \frac{GDD}{2!} \cdot (\omega - \omega_0)^2 + \frac{TOD}{3!} \cdot (\omega - \omega_0)^3 + ... \quad (2.6)$$

This description utilizes the fact that the spectrum and therefore $A(\omega)$ have a finite width, which naturally limits the number of terms in the expansion one has to consider. In the present work, it is sufficient to limit ourselves to the first four terms. The first of those is the CEP and it is identical to the CEP in the time-domain. The second term is the "Group Delay" GD. It results in a shift of the entire pulse forward or backward in time. The third term is the "Group Delay Dispersion" GDD. It is the first term that changes the shape of the pulse and therefore its duration. Its effect is displayed for an example pulse in Figure 2.5:

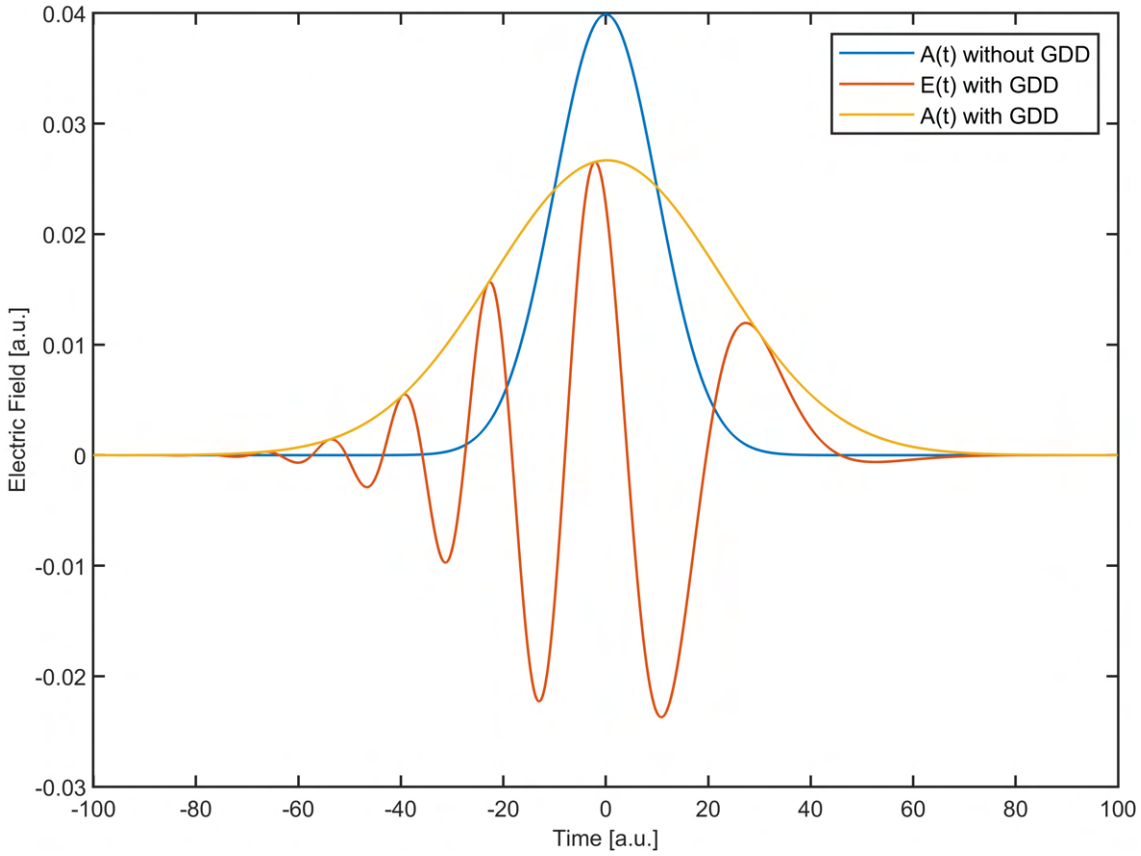

Fig. 2.5: Depiction of a laser pulse demonstrating the effect of a non-zero GDD term. Displayed is the envelope of the pulse without GDD term (blue), as well as the electric field (red) and envelope (yellow) of the same pulse after increasing the GDD.

By looking at Figure 2.5 one can see the two effects a non-zero GDD has. First of all, one observes a symmetric broadening of the pulse in time by comparing the envelope with and without GDD. Due to the conservation of energy this also results in a reduction of the peak of the electric field amplitude. The duration of a pules that is only effected by GDD can be calculated according to:

$$\tau = \tau_0 \cdot \sqrt{1 + (4\ln 2 \frac{\mathrm{GDD}}{\tau_0^2})^2} \tag{2.7}$$

with τ the resulting pulse duration and τ_0 the pulse duration, if there was no GDD.

The second effect is only visible by looking at the electric field with non-zero GDD. Here, it is apparent that the oscillations of the field no longer have a constant frequency. Instead the frequency decreases from left to right in Figure 2.5. This phenomenon is called "chirp" and is functionally identical to the effect of the same name for acoustic waves.

The last term in Equation 2.6 is the "Third Order Dispersion" TOD. Its effect is displayed for an example pulse in Figure 2.6:

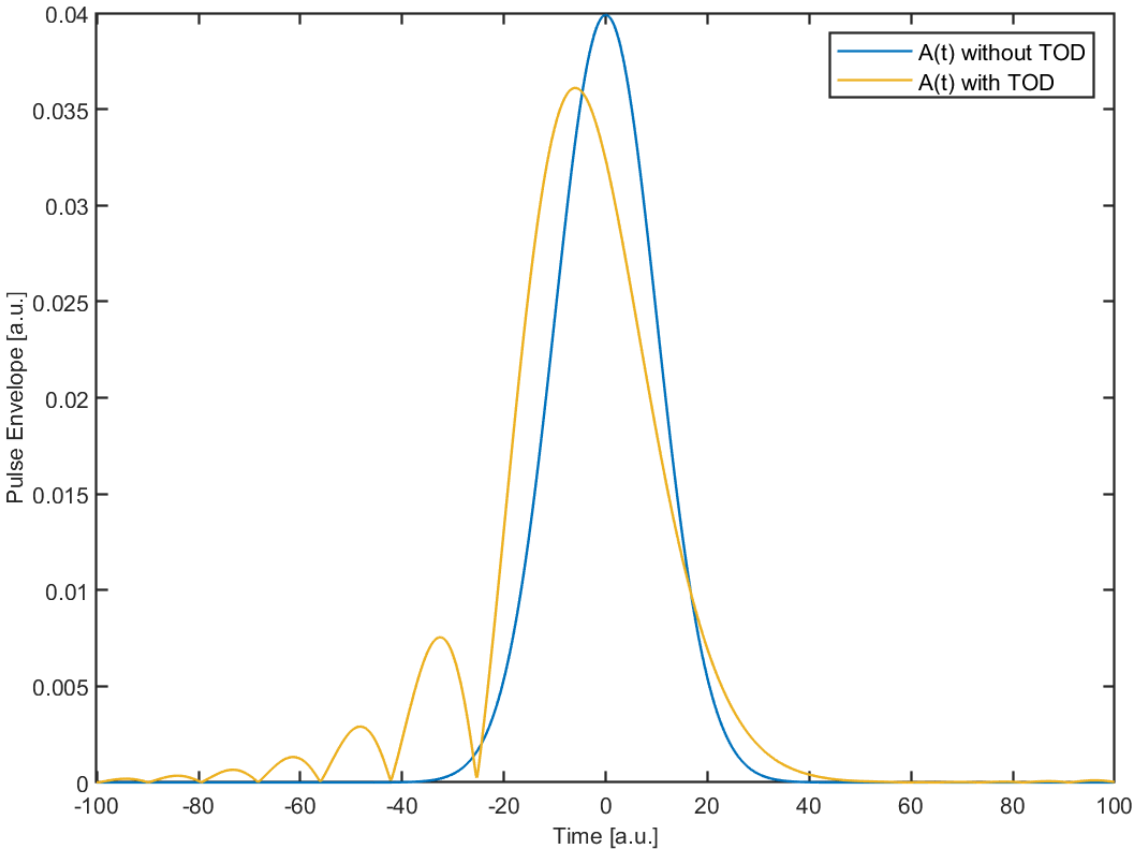

Fig. 2.6: Depiction of a laser pulse demonstrating the effect of a non-zero TOD term. Displayed is the envelope of the pulse without GDD (blue) and the envelope (yellow) of the same pulse after increasing the TOD.

The most important aspect of a non-zero TOD is the appearance of pre- or post-pulses and the asymmetric modulation of the main pulse. Since the pre- or post-pulses contain energy, the energy of the main pulse is reduced with increasing TOD. The consequence is a reduced maximum electric field strength.

With this information we know that in order to obtain the shortest pulses and therefore high electric field strength, we need the leading terms in the spectral

phase to be zero. Pulses that fulfill this condition are called "Fourier-limited" (FL) pulses. For such pulses the duration is exclusively determined by the envelope $A(\omega)$ according to:

$$\Delta t \cdot \Delta\omega = TBP \tag{2.8}$$

with Δt the time-duration of the pulse given as the "Full Width at Half Maximum" FWHM, $\Delta\omega$ the FWHM of the spectrum and therefore, also the FWHM of $A(\omega)$ and the "Time Bandwidth Product" TBP, which is a constant dimensionless number that depends on the general shape of $A(\omega)$. In this thesis, every envelope will be assumed gaussian.

In summary, the need for high enough electric field strength in order to start the ionization of clusters during helium nanoplasma formation imposes the need for short laser pulses that are Fourier-limited and show a sufficiently broad spectrum. Generating such pulses will be looked at in more detail in the next section.

2.4.2 Generation of short laser pulses

In order to generate the required short pulses at a central wavelength of $\lambda = 2$ µm a non-linear optics setup will be used and the utilized processes will be explained in the following subsections. At the heart of all optical processes lies the fact that an electric field $\boldsymbol{E}(t)$ induces a polarization $\boldsymbol{P}(t)$ in a material. This polarization in turn may generate electric fields of a different character. In a non-linear optics process, $\boldsymbol{P}(t)$ responds non-linearly to the input field $\boldsymbol{E}(t)$. This results in the output electric field to respond non-linearly to the input field as well. To better understand the non-linear response of $\boldsymbol{P}(t)$, we expand it in a Taylor series:

$$\begin{aligned}\boldsymbol{P}(t) = \epsilon_0(\chi^{(1)}\boldsymbol{E(t)} + \chi^{(2)}\boldsymbol{E(t)}\cdot\boldsymbol{E(t)} + \\ \chi^{(3)}\boldsymbol{E(t)}\cdot\boldsymbol{E(t)}\cdot\boldsymbol{E(t)} + \chi^{(3)}\boldsymbol{E(t)}\cdot\boldsymbol{E(t)}\cdot\boldsymbol{E(t)}\cdot\boldsymbol{E(t)} + \dots)\end{aligned} \tag{2.9}$$

with ϵ_0 the vacuum-permitivity and $\chi^{(n)}$ the n-th order susceptibility of the material. In general, $\chi^{(n)}$ is a tensor of rank (n+1), whose elements describe the materials (lack of) symmetries and its response to different polarization directions of $\boldsymbol{E}(t)$. To understand the effects used in the utilized processes, we can further restrict us to the second term: $\boldsymbol{P}(t) = \epsilon_0\chi^{(2)}\boldsymbol{E(t)}\cdot\boldsymbol{E(t)}$. We will further limit ourselves by treating $\boldsymbol{P}(t)$, $\boldsymbol{E}(t)$ and $\chi^{(n)}$ as scalar quantities for now. We will also assume, that the initial $E(t)$ is simply a sum of two cosine waves with differing frequencies ω_1 and ω_2: $E(t) = \frac{1}{2}(E_1 e^{-i\omega_1 t} + E_2 e^{-i\omega_2 t} + c.c.)$ with $c.c.$ being the complex conjugate. Utilizing all of that we obtain:

$$P(t) = \epsilon_0 \chi^{(2)} E(t) \cdot E(t) = \frac{1}{4}\epsilon_0 \chi^{(2)} (E_1^2 e^{-i2\omega_1 t} + E_2^2 e^{-i2\omega_2 t} + 2E_1 E_2 e^{-i(\omega_1+\omega_2)t} + 2E_1 E_2^{\cdot} e^{-i(\omega_1-\omega_2)t} + |E_1|^2 + |E_2|^2 + c.c.) \tag{2.10}$$

In Equation 2.10 we already find four different processes happening.
The $E_1^2 e^{-i2\omega_1 t} + E_2^2 e^{-i2\omega_2 t}$ terms correspond to "Second Harmonic Generation" SHG, where components with twice the initial frequency are generated.
The $2E_1 E_2 e^{-i(\omega_1+\omega_2)t} + 2E_1 E_2^{\cdot} e^{-i(\omega_1-\omega_2)t}$ terms correspond to "Sum Frequency Generation" SFG and "Difference Frequency Generation" DFG, respectively. The $|E_1|^2 + |E_2|^2$ terms cause an effect called "optical rectification". Of special interest is the DFG process, since it will be used to generate the $\lambda = 2$ µm pulses in the present work, as well as to amplify them to the required pulse energy for studying helium nanoplasma formation and relaxation by means of XUV fluorescence spectroscopy.

To see how the polarization in Equation 2.10 leads to new electric fields, we have to look at the non-linear wave-equation for a lossless, dispersionless and isotropic material, a detailed derivation of which can be found in [57]:

$$-\boldsymbol{\nabla}^2 \boldsymbol{E} + \frac{n^2}{c^2}\frac{\partial^2}{\partial t^2}\boldsymbol{E} = -\mu_0 \frac{\partial^2}{\partial t^2}\boldsymbol{P}^{NL} \tag{2.11}$$

With $\boldsymbol{P}^{NL}$ being the non-linear part of $\boldsymbol{P}(t)$. Utilizing Equation 2.11 and the expression for the DFG process derived above as well as further separating off the spatial oscillations of the electric field with $E_n = A_n \cdot e^{ik_n z}$ one can derive the coupled wave equations for the DFG process (details again in [57]):

$$\begin{aligned} \frac{dA_1}{dz} &= \frac{i\omega_1^2 \chi^{(2)}}{k_1 c^2} A_2 A_3 e^{i\Delta k} \\ \frac{dA_2}{dz} &= \frac{i\omega_2^2 \chi^{(2)}}{k_2 c^2} A_1 A_3^{\cdot} e^{i\Delta k} \\ \frac{dA_3}{dz} &= \frac{i\omega_3^2 \chi^{(2)}}{k_3 c^2} A_1 A_2^{\cdot} e^{i\Delta k} \end{aligned} \tag{2.12}$$

With $\omega_3 = \omega_1 - \omega_2$ and the phase matching relation $\Delta k = k_1 - k_2 - k_3$. The mechanism of phase matching will be explained in subsection 2.4.3. For now, we will simply assume perfect phase matching, which corresponds to $\Delta k = 0$. To get a better understanding of Equation 2.12, we have numerically simulated and displayed them in Figure 2.7. This simulated case deals with a typical situation, where we start with a strong pump beam (high $|A_1|^2$), a weak "signal" beam (low $|A_2|^2$) and without any "idler" beam (no $|A_3|^2$ at start).

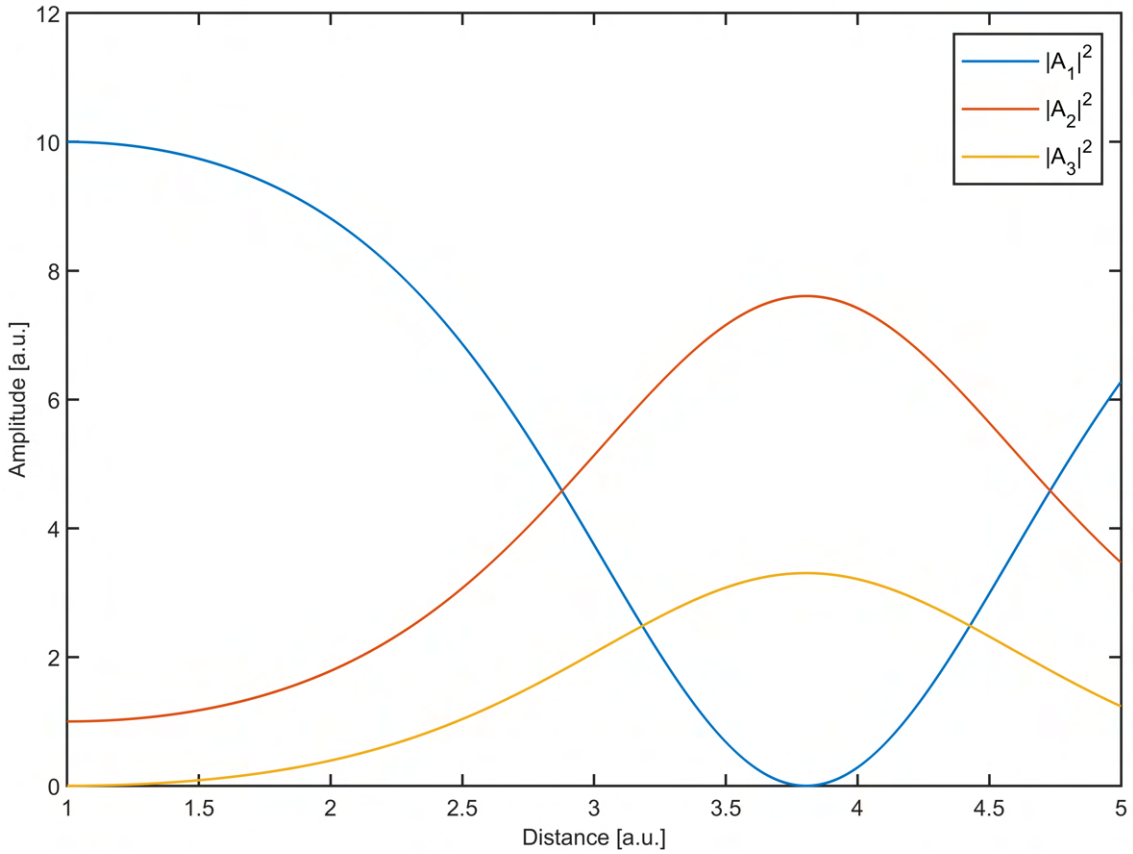

Fig. 2.7: Numerical simulations of Equation 2.12

In Figure 2.7 we see two effects. The generation of the difference frequency $|A_3|^2$ that wasn't present at the start and the simultaneous amplification of $|A_2|^2$ that was present at the start. The first effect is used in a so-called "DFG stage", where the initial 2 µm pulse is generated by utilizing a wavelength of $\lambda_1 = 680\,\text{nm}$ for $|A_1|^2$ and $\lambda_1 = 1030\,\text{nm}$ for $|A_2|^2$. The second effect is used in a so-called "Optical Parametric Amplifier" OPA, where the generated 2 µm pulse is amplified by acting as $|A_2|^2$, while $\lambda_1 = 1030\,\text{nm}$ is utilized as $|A_1|^2$.

The extension of the OPA principle is the so-called "Optical Parametric Chirped Pulse Amplifier" OPCPA. In practice, OPAs are limited in their possible amplification by the damage threshold of the non-linear material. Here, $|A_2|^2$ is amplified to the point of destroying the material. For CW beams used in the simulation shown in Figure 2.7 this is much less of an issue than for the femtosecond pulses used in the course of this work, since the peak of $|A_2|^2$ is of importance. In order to mitigate crystal damage, a "stretcher" is placed before the OPA. This device introduces GDD to the pulse, which chirpes the pulse and stretches it in time. The pulse can then be amplified up to the damage threshold of the OPA and afterwards be compressed again in a "compressor" which adds GDD to the pulse in a way to offset the GDD introduced by the stretcher. Ultimately, this yields short pulses with intensities far above the damage threshold of the OPA. The functionality of an OPCPA is also displayed in Figure 2.8:

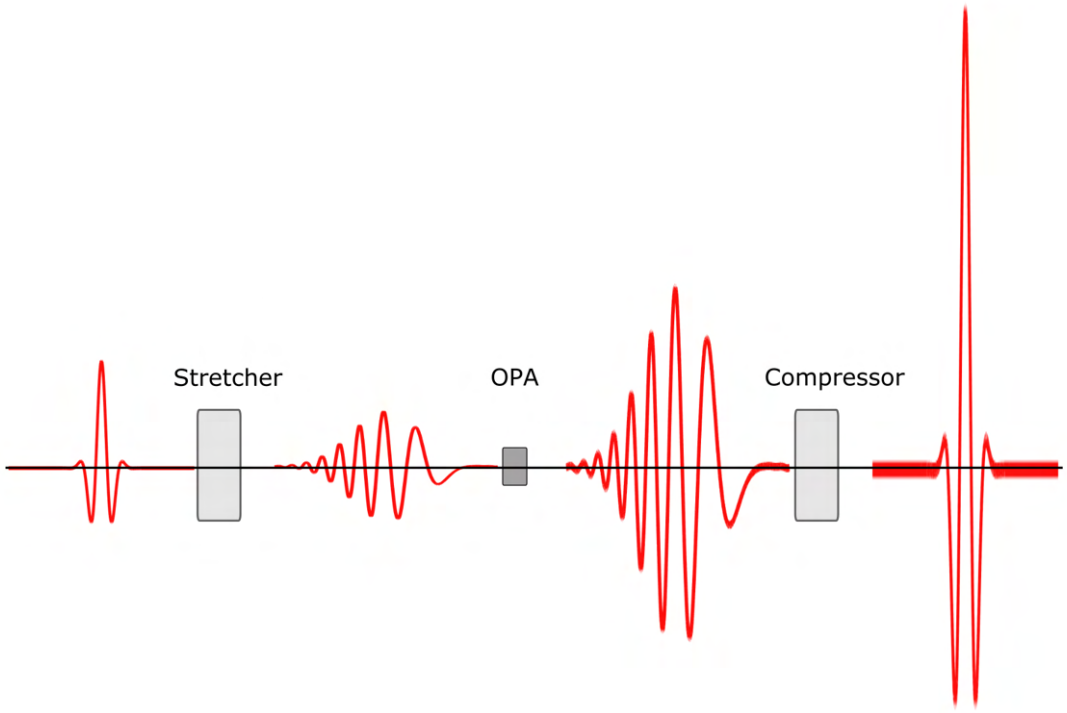

Fig. 2.8: Operation principle of an OPCPA consisting of stretcher, OPA and compressor.

The last effect that shall be mentioned is "Super Continuum Generation" SCG. It is a collection of different non-linear effects that result in a huge broadening of the spectrum of an input pulse. The process is not the focus of this work and details can be found elsewhere [57, 58]. It is used here to generate the $\lambda_1 = 680\,\mathrm{nm}$ light out of $\lambda_1 = 1030\,\mathrm{nm}$ pulses, which is used in the generation of the $2\,\mu\mathrm{m}$ pulses in the DFG stage.

2.4.3 Phase matching concept

In the above chapter on the DFG process the phase matching condition has been introduced: $\Delta k = 0$. In this section, we will further elaborate on this important concept. The idea is that any non-linear medium consists of not just one but many individual dipoles each radiating at the involved frequencies. These individual dipoles don't need to radiate light in phase with each other. However, only in the case of constructive interference between the light of all dipoles, efficient generation or amplification of frequencies occurs. Mathematically, this is the case, when the wave vectors of the beams involved add up to zero, i.e. $\Delta \boldsymbol{k} = \boldsymbol{k_1} - \boldsymbol{k_2} - \boldsymbol{k_3} = 0$. For

bulk material like the crystals used as OPAs, there are three methods of achieving phase matching. Let's start by assuming all beams are collinear and we can therefore neglect the vector nature of the wave vectors. In this case, the equation simplifies to:

$$\frac{n(\omega_1)\omega_1}{c} = \frac{n(\omega_2)\omega_2}{c} + \frac{n(\omega_3)\omega_3}{c} \tag{2.13}$$

considering $\omega_3 = \omega_1 - \omega_2$ and that $n(\omega)$ is usually a monotonously growing function. One notices that the phase matching condition cannot be fulfilled in regular non-birefringent materials. Obviously, the first solution to achieve phase matching is the use of birefringent materials. Such materials have a refractive index that depends on the polarization of the incoming light due to a susceptibility tensor $\chi^{(n)}$ that can no longer be assumed to be a scalar. If the difference in the refractive indices is large enough between the two or more directions, phase matching can be achieved by a method called "angle tuning". Here, the crystal axis is placed at an angle with respect to the propagation direction of the incoming light such that Equation 2.13 is fulfilled. Alternatively, some materials such as Lithium-Niobate display a strong dependence of the refractive index on the temperature of the crystal. Such crystals can fulfill Equation 2.13 via the second method called "Temperature Tuning". The third method is called "non-collinear phase matching" and utilizes the vector nature of $\Delta\boldsymbol{k} = \boldsymbol{k_1} - \boldsymbol{k_2} - \boldsymbol{k_3} = 0$ to achieve phase matching by using non-collinear input beams as displayed in Figure 2.9. An OPA utilizing this type of phase matching is called a "Non-collinear Optical Parametric Amplifier" NOPA.

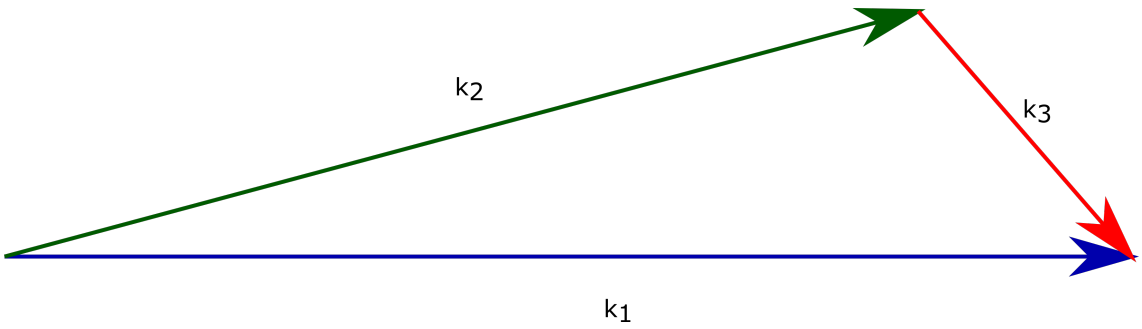

Fig. 2.9: Example of wavevectors in a non-colinear phasematching setup.

2.4.4 High-harmonic generation

One of the most noteworthy non-linear frequency up-conversion effects one encounters, when using strong-field ionization with a gas target is the process of "high-harmonic generation"(HHG). This is a non-pertubative process that converts energy from the drive laser into coherent and directed light with many times the interacting drive-laser frequency. The first model for this process was proposed by Corkum et

al. [59], which is known as the semi-classical "three-step model". Later on, Lewenstein et al. [60] expanded it into a fully quantum-mechanical model. As the name implies, the model separates the HHG process into three distinct steps as displayed in Figure 2.10:

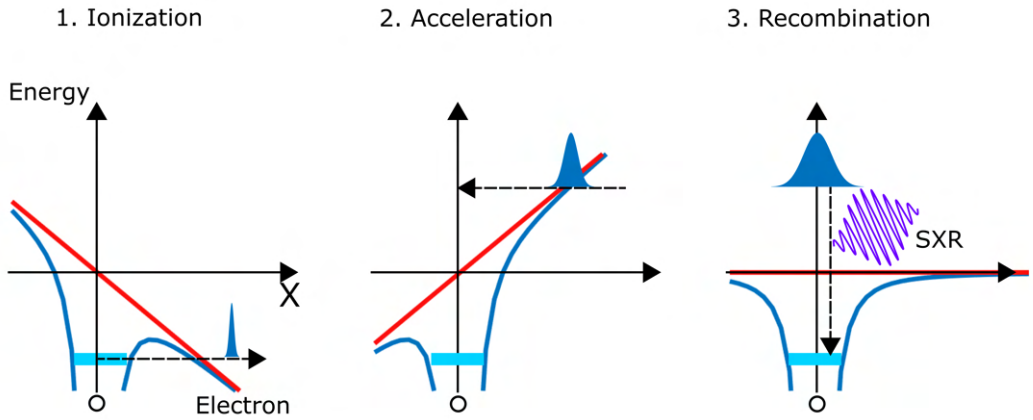

Fig. 2.10: Schematic depiction of the three-step model. Displayed is the potential induced by the field of the drive laser (red line), the resulting potential from drive laser and atomic potential (blue line), the initial energy level of the outermost bound electron (light blue), as well as the movement of the electron-wave-packet (blue gaussian)

In the initial ionization step of the three-step model the electric field of a drive laser is strong enough to deform the electric potential of an atom in order to allow for tunneling ionization. The released electron then propagates in the field of the laser. In the subsequent acceleration step the field of the drive laser causes the electron to be accelerated away from the nucleus until the field switches its sign. Now, the electron is accelerated back towards the nucleus. In the final recombination step the electron passes by the nucleus and recombines with it akin to a reverse photoelectric effect. Thereby, releasing its kinetic energy plus the ionization energy of the atom in the form of a photon with an odd integer multiple of the frequency of the drive-laser. HHG is an established technology for generating very short laser pulses with wavelengths in the deep ultraviolet, extreme ultraviolet and soft x-ray spectral ranges [61, 62, 63, 64, 65]. The maximum photon energy E_{cutoff} generated by the HHG process can be calculated with the formula:

$$E_{cutoff} = E_I + 3.17 \cdot U_p = E_I + 3.17 \cdot \frac{e^2 I}{2c\epsilon_0 m\omega_0^2} = E_I + 3.17 \cdot \frac{e^2 c}{2\epsilon_0 m} \cdot I\lambda^2 \quad (2.14)$$

with E_I the ionization potential of the atom (here helium), e the charge of the

electron, I the intensity of the drive laser, c the speed of light, ϵ_0 the vacuum-permitivity, ω_0 the center frequency of the drive laser and λ the wavelength of the drive laser. In order to achieve maximum photon energy, one is only left with maximizing the intensity I and the wavelength λ. There exists an upper limit for the usable intensity I, which will be explained later in this section leaving only increases in λ as a path towards higher photon energies. This is very unfortunate, since HHG efficiency using rare gas targets has a wavelength scaling of between $\lambda^{-5.5\pm0.5}$[66] and $\lambda^{-6.3\pm1.1}$[67]. Therefore, any increase in maximum photon energy by using a longer wavelength λ causes a dramatic reduction in generation efficiency. This is mostly caused by the electron wave packet expansion during the acceleration step (as can be seen in Figure 2.10), which reduces the recombination cross section during the recombination step. Using clusters as a target in an HHG source might be a route to alleviate this effect, by increasing the size of the target for recombination. While some publications on HHG using clusters as the target exist [68, 69, 70], they mainly focus on smaller clusters of heavier noble gasses like Xe, and Kr, where changes in cluster size are achieved by changing the stagnation pressure behind the gas nozzle.

To understand HHG and the unique environment that a cluster target might provide, one has to first look at the underlying physics in the case of atomic gas targets. Here, the concept of phase matching applies as well. The goal is again to achieve $\Delta k = 0$ as in the case of non-linear wave mixing, but here Δk has three different components [71]. The first one is Δk_{Gouy}, which arises due to a geometric wave vector mismatch caused by the focusing geometry required to reach the necessary intensity to start the HHG process. It has the form

$$\Delta k_{Gouy} = q\frac{\partial \phi_{Gouy}}{\partial z} = q\frac{\partial}{\partial z}(-arctan(\frac{z}{z_0})) \tag{2.15}$$

with ϕ_{Gouy} the Gouy phase, q the harmonic order, z the coordinate in the propagation direction and z_0 the focus position. The second term is $\Delta k_{dispersion}$ and it originates from the dispersion introduced by the neutral atoms and ionized electrons. Of note is that the dispersion of free electrons has the opposite sign of the dispersion of neutral atoms. The term takes the form:

$$\Delta k_{dispersion} = \frac{2\pi q}{\lambda}\frac{p}{p_0}\Delta\delta(1-\frac{\eta}{\eta_c}) \tag{2.16}$$

with λ being the wavelength of the drive laser, p the pressure of the gas target, p_0 the standard pressure (1013 mbar), $\Delta\delta$ the difference in refractive indices between fundamental and high-order harmonic, η the ionization fraction and η_c the critical ionization fraction. The critical ionization fraction marks the ionization fraction at which the dispersion introduced by the electrons exactly balances the dispersion contribution from the neutral atoms.

The third term involves the dipole phase and has the form

$$\Delta k_{Dipole} = -\alpha_q \frac{\partial I}{\partial z} \tag{2.17}$$

with α_q being a proportionality constant.

In the focus position of the laser bream path Equation 2.17 is zero and Equation 2.16 and Equation 2.15 can be combined with the phase matching condition to yield the formular for the required pressure of the gas in the focal spot:

$$p = p_0 \frac{\lambda^2}{2\pi^2 w_0^2 \Delta\delta(1 - \frac{\eta}{\eta_c})} \tag{2.18}$$

with w_0 being the focal spot size. This combined formula shows the existence of an upper limit for the usable intensity I of the drive laser pulse. Note, the ionization fraction η increases the higher the intensity of the laser I is. For too large I, it follows that $\frac{\eta}{\eta_c} > 1$ and therefore phase matching is no longer possible. Additionally, one sees from Equation 2.18 that the only parameter, which allows to actively change the phase matching condition is the pressure of the gas target p. This is one shortcoming of the published studies on HHG with cluster targets, where cluster size and pressure (particle density) could not be changed independently from each other.

The present setup to generate helium clusters and large droplets allows to control pressure and temperature independent from each other in order to generate clusters of a desired size at different particle densities. This means that there exists a pressure range for which the desired cluster size can be achieved by setting the correct temperature. The actual pressure inside the range can then be chosen in order to optimize the phase matching condition for different cluster sizes.

However, the above formulas and considerations for HHG apply to the case of atomic gas targets. In the case of clusters several different size-dependent regimes have to be considered, where the mechanism for the establishment of phase matching differs significantly. Their conditions are depicted in Figure 2.11.

On the first view, five different regimes for phase matching emerge, when using clusters as a target. The simplest regime is shown in Figure 2.11 a), where only atomic gas is considered. Here, all the above formulas apply and optimum phase matching by choosing the correct gas pressure is a well-established procedure. The gas-like regime depicted in Figure 2.11 b) is only slightly different. It includes small clusters, which contain only a few tens of atoms and where the size of the clusters and any propagation effects inside the clusters are negligible. Overall, the expectation is that phase matching still follows the formulas from the gas phase. The above-cited studies on HHG from clustered gas operate in this regime. The mixed regime in Figure 2.11 c) is perhaps the most challenging in order to derive a microscopic understanding. Here, the HHG process happens inside a few clusters of significant size. Propagation effects inside the nanoparticle can no longer be neglected as do surface effects like diffraction during entry and exit. Laser beam and interaction parameters also change on timescales comparable to the drive laser pulse duration in the generated nanoplasma as discussed in subsection 2.3.3. The bulk-like regime sketched in Figure 2.11 d) is characterized by the HHG process happening inside a single cluster with size comparable to the diameter of the laser focus. Here, propagation effects inside the cluster are expected to dominate. Surface effects are still significant, but less so than in the mixed regime, since in the latter more surfaces of smaller curvature are involved. Nevertheless, cluster effects like resonant heating still play a role on the timescale of the HHG process even in large droplets. The last regime is the bulk-liquid regime. Here, the cluster jet produces a regular liquid jet, with properties similar to bulk-liquid helium. Surface effects are further reduced compared to the earlier regimes since radii are of macroscopic size. Cluster effects like resonant heating and the trapping of quasifree electrons become also less important. Phase matching, as it is performed in the gas regime, has not been achieved in this regime, rather existing publications using water as the target calculate the distance over which coherent buildup of the HHG signal can be expected and adjust the target dimension accordingly [72, 73].

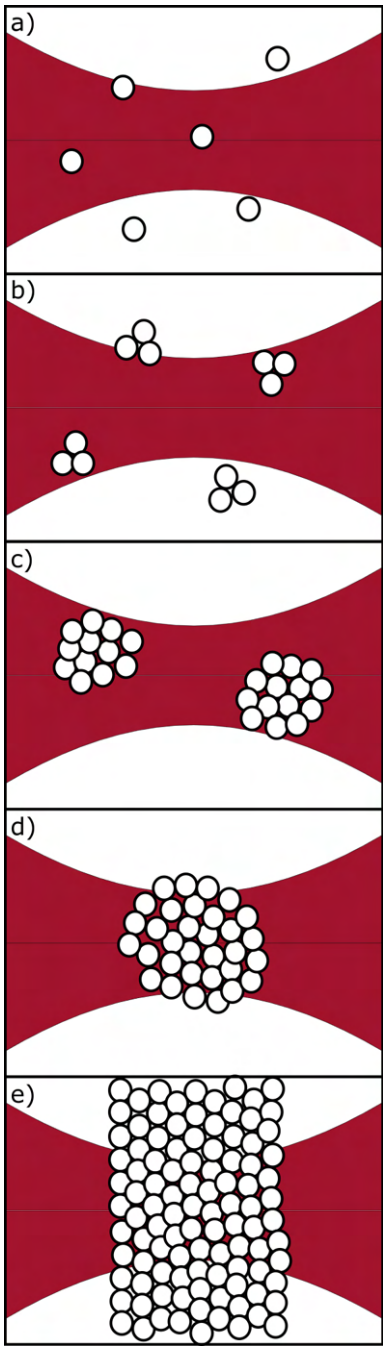

Fig. 2.11: Schematic depiction of the different regimes for phase matching of HHG that are defined by the size and particle density of clusters: a) gas regime with atomic emitters, b) gas-like regime, where small clusters can be treated like molecular gases to achieve phase matching, c) mixed regime, where HHG happens in a small number of clusters and size, shape and particle density affecting the HHG process significantly, d) bulk-like regime, where HHG happens inside a single cluster and e) the bulk-liquid regime (for details see main text)

Chapter 3

Experimental Setup

3.1 Laser systems

Two laser systems were utilized in this work. The first one is a commercial high-power femtosecond Pharos SP laser system made by "Light Conversion". It produces pulses with a central wavelength of 1030 nm, at a repetition rate of 5 kHz with a pulse energy of 1 mJ and variable pulse duration. The pulse duration could be varied by moving the motorized compressor grating inside the laser. Depending on the position of the grating the pulses would contain different amounts of dispersion causing them to get stretched in time. In order to characterize the pulse duration as a function of the grating position I measured the pulse duration using a commercial autocorrelator "pulsCheck" from "APE Angewandte Physik & Elektronik GmbH". The results are shown in Figure 3.1. As can be seen the pulse duration follows the expected increase according to Equation 2.7. For small amounts of added dispersion ($<$ 78,000 steps) the pulse duration increase is non-linear. Beyond that the pulse duration increases linearly with added dispersion. The minimum measured pulse duration was 180 fs, which matches the stated performance by the company.

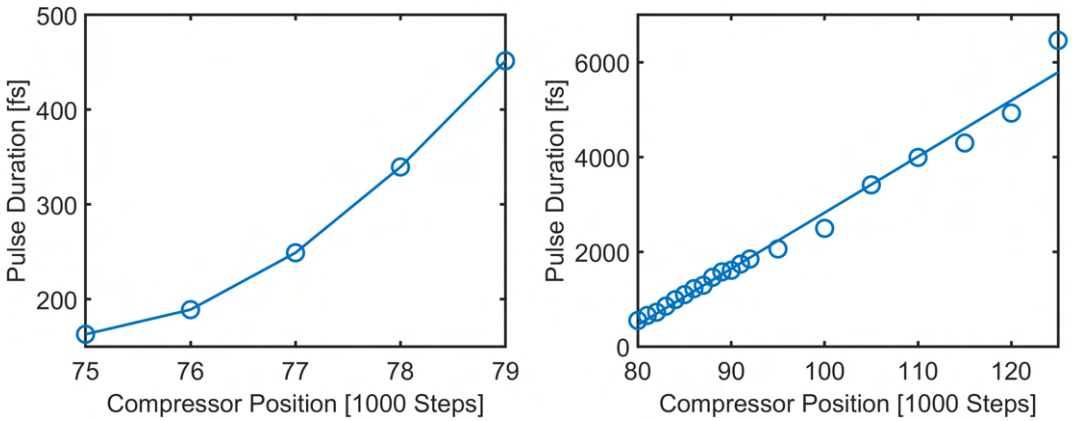

Fig. 3.1: Measured pulse duration via autocorrelation of the Pharos pulses as a function of the position of the compressor grating. The left figure shows the non-linear regime with small amounts of GDD, the right figure shows the linear regime with large amounts of GDD.

The second high-average power laser system delivering shorter pulses compared to the Pharos was built by me as a substantial part of this thesis work. It is an OPCPA system powered by a commercial pump laser from AMPHOS. The pump laser delivers pulses with a central wavelength of 1030 nm, a pulse energy of 1 mJ and a pulse duration of 800 fs at a repetition rate of 200 kHz. Those pulses are then split up to pump the multiple stages of the complex OPCPA setup. The overall layout is presented in Figure 3.2:

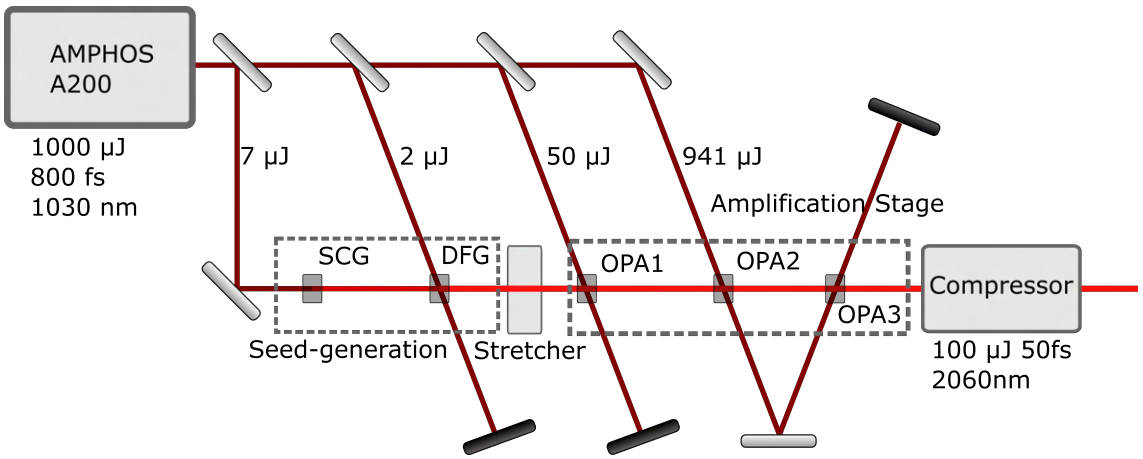

Fig. 3.2: Schematic layout of the OPCPA system consisting of a two-part seed-generation and a three-part amplification stage

In the first step, 7 µJ of the AMPHOS are used as a pump in a super-continuum generation (SCG) process in order to generate a broad spectrum around 650 nm wavelength (displayed in Figure 3.3) in a 14 mm long YAG crystal. The visible light then acts a pump in the following collinear DFG stage inside a Beta Barium Borat crystal (BBO) with a length of 5 mm. In the DFG stage 2 µJ of the 1030 nm pump acts as the seed. It generates an idler pulse with a spectrum as shown in Figure 3.3 and a pulse energy of 50 pJ. The spectrum has a center wavelength of 1920 nm and a FWHM of 270 nm supporting a minimum possible pulse duration of 19.8 fs.

BBO also acts as the material of choice for the non-linear crystals in the subsequent OPA stages for a number of reasons. First of all, its wide phase-matching range allows for the efficient amplification of light with a bandwidth spanning from 1800 nm all the way to 2250 nm. Other potential materials, such as Potassium Titanyle Arsenate ($KTiOAsO_4$, KTA), do not support such a wide spectrum for amplification. A second aspect are the thermal properties of BBO. Since we operate with an average pump power exceeding 190 W, the crystals need to be able to withstand the high thermal load. In our own experiments BBO has distinguished itself in this role as well. In order to achieve phase matching, we employed angle tuning with a theta angle of 20° between the crystal axis and the propagation direction in the DFG stage and 21.3° in the OPAs (1-3). In all stages, we focused the AMPHOS pump beam down to a spot size that results in a peak intensity of about 80 $\frac{GW}{cm^2}$.

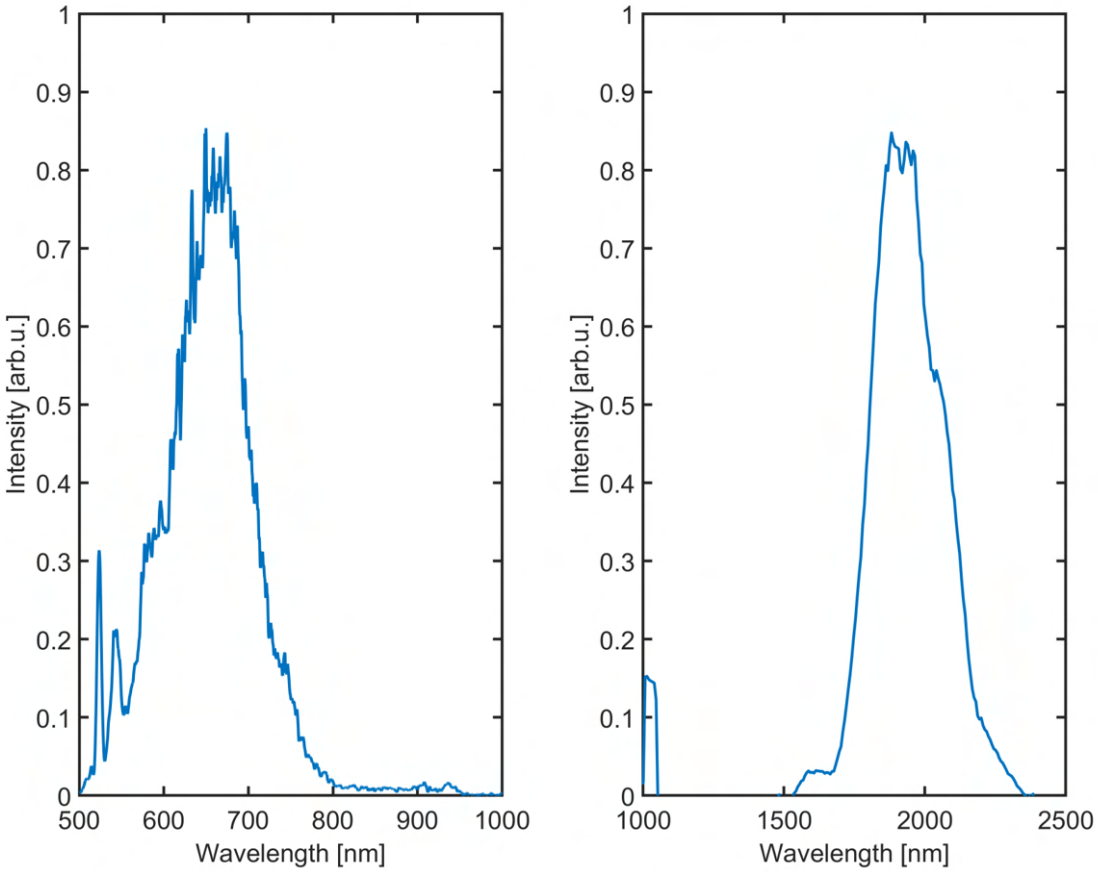

Fig. 3.3: Measured spectrum of the SCG source (left) and the DFG source (right). In the SCG spectrum one can see some SHG signal at 515 nm generated by the pump. However, the dominating part of the spectrum is the light generated via the SCG process that is centered around 650 nm. In the DFG spectrum one can see some of the remaining light at a wavelength of 1030 nm, while the dominating part of the spectrum is the light generated via the DFG process that is centered around 1920 nm.

The duration of the broadband pulses (1800 nm to 2250 nm) is then increased by adding a GDD of 2431 fs^2 in a 3 mm long stretcher made out of silicon. Afterwards, the stretched pulses act as the seed in non-collinear OPA1, which is a 5 mm long BBO crystal, where both seed and the 50 µJ pump pulse from the AMPHOS system pass twice. The output spectrum after OPA1 is shown in Figure 3.4 (left) and has a total energy of 1 µJ. It has a center wavelength of 2070 nm and a FWHM of 195 nm, which leads to a minimum possible pulse duration of 32.0 fs.

Finally, the amplified infrared (IR) pulses get further amplified in OPA2 and OPA3 using two BBO crystals with a length of 3 mm each. Both of which are pumped by the same 941 µJ that remains from the AMPHOS pump pulses. The resulting IR pulses have an energy of 100 µJ and the spectrum shown in Figure 3.4 (center). It has a center wavelength of 2100 nm and a FWHM of 260 nm, which leads to a minimum possible pulse duration of 25.3 fs.

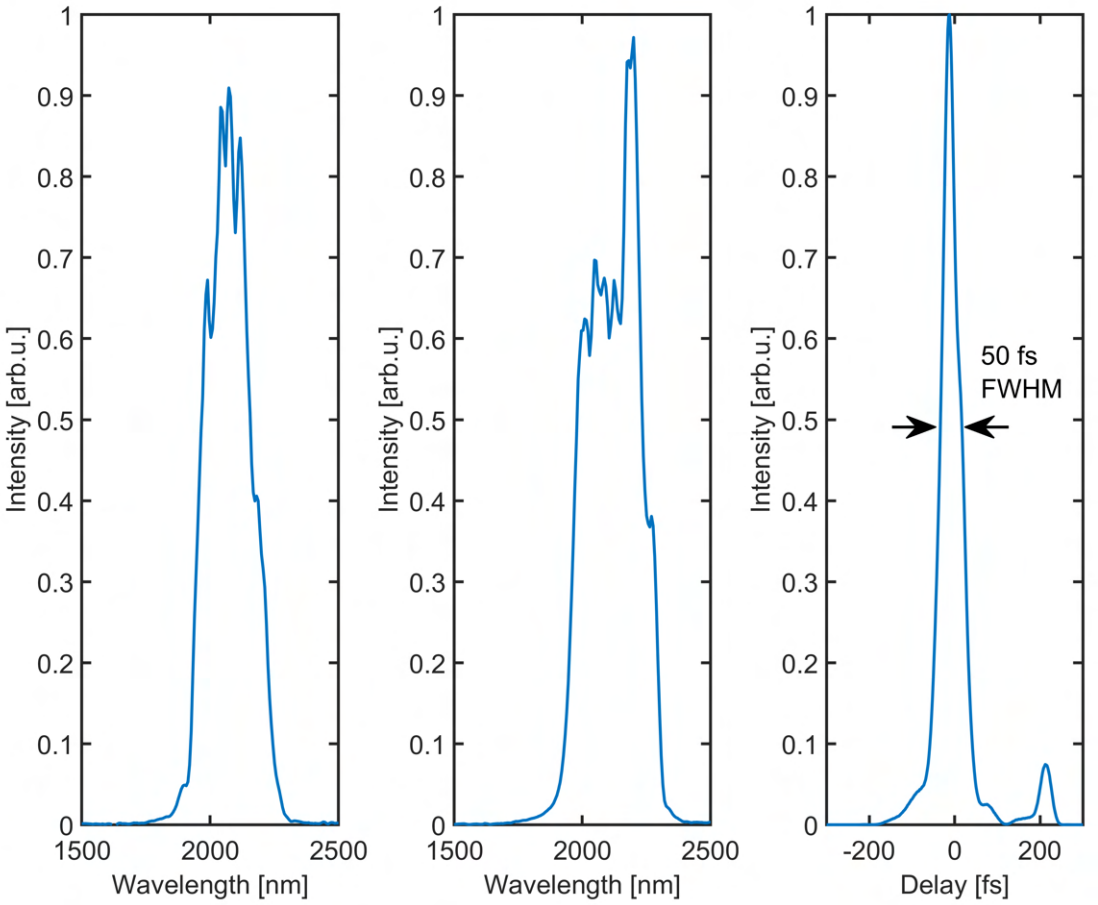

Fig. 3.4: Measured spectrum after OPA1 (left), after OPA3 (center) and the reconstructed temporal envelope after compression(right).

After the final amplification stage the IR pulses get compressed down to a "Full Width at Half Max" (FWHM) pulse duration of 50 fs using 50 mm of bulk IR-fused silica. Their duration is measured using a self-built frequency-resolved optical gating (FROG) device. The compression and measurement of the pulse duration were installed and performed by Phillip Merkl as part of our collaboration with Class 5 Photonics GmbH. The reconstructed intensity envelope in the time domain is shown in Figure 3.4 (right).

3.2 Cluster source

In order to generate helium clusters and large droplets, I used a Gifford-McMahon cryocooler made by "Sumitomo". This is a closed-cycle two-stage cryocooler with its first stage capable of reaching temperatures less than 40 K and with its second stage less than 4 K. A home-made cold head built from oxygen-free high-thermal-conductivity copper fits to the second stage. It contains the heating cartridge capable of up to 50 W of heating power, the stainless steel pipe for delivering helium into

the cold head, the stainless steel sintered filter with a pore size of 1 µm, the diode used for temperature measurement located directly at the nozzle and the electron microscope diaphragm with a 5 µm orifice (Plano), which acts as the nozzle through which the helium cluster beam leaves the cluster source. A sectional view is shown in Figure 3.5. Since the cold head alone would not be capable of reaching the desired temperature of 4 K due to excessive thermal radiation from the vacuum chamber walls, it is covered by a large heat shield, which is attached to the first stage operating at 40 K. The cryostat is shown in Figure 3.6.

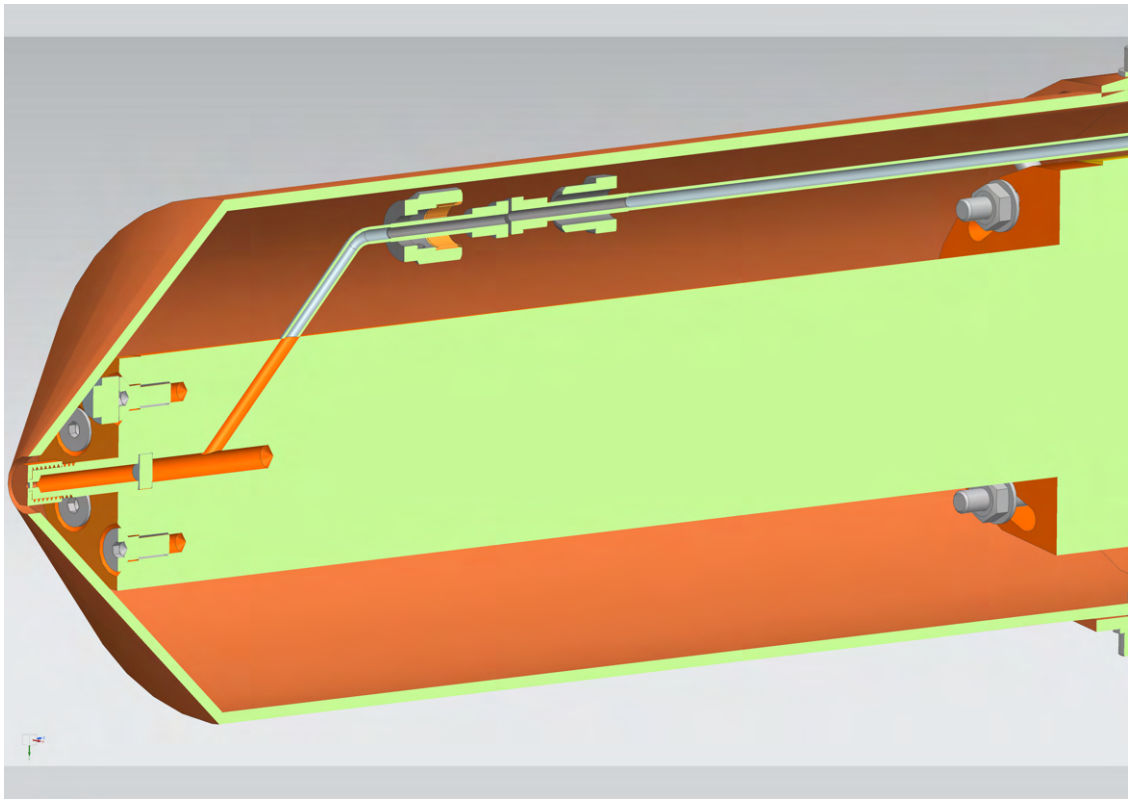

Fig. 3.5: Sectional view of the cryostats 3D model. The green part in the center is the solid copper block that is connected to the cold head of the cryostat. The outside cylinder is the heat shield that is connected to the first stage. In between them runs the helium supply pipe that continuously delivers helium gas to the reservoir inside the copper block. The reservoir is separated by a stainless steel sintered-filter with a pore size of 1 µm into a front and back part. The front part then connects to the orifice with a diameter of 5 µm.

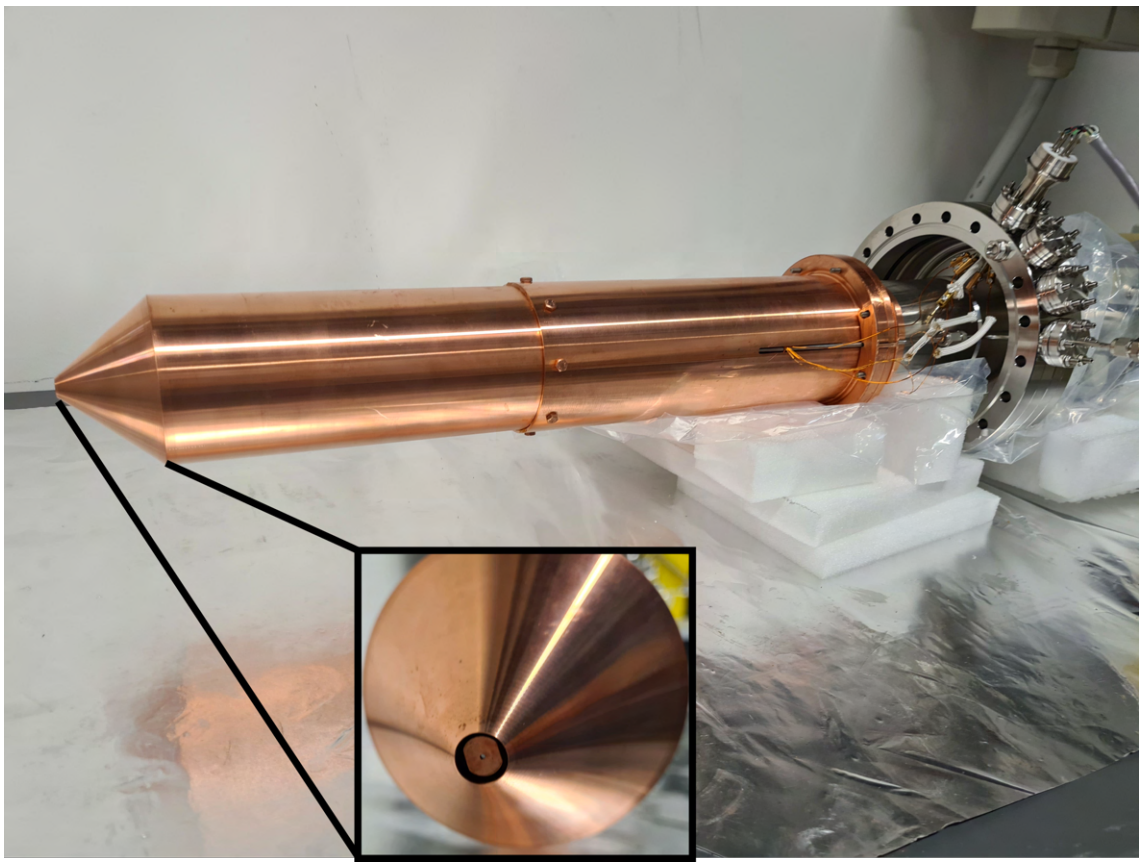

Fig. 3.6: Picture of the fully assembled cryostat with the outer copper parts constituting the heat shield. One can also see the helium pipe leaving the heat shield and connecting to the chamber feed through (horizontal), as well as the cables from the the diode and cartridge connecting to the electrical feed through (vertical). Insert: Picture of the nozzle of the cryostat with the conical copper part being the tip of the heat shield, the flat copper part belonging to the cold head and the small hole in it leading to the diaphragm containing the 5 µm orifice.

3.3 Vacuum system

The vacuum system consists of two chambers as displayed in Figure 3.7.

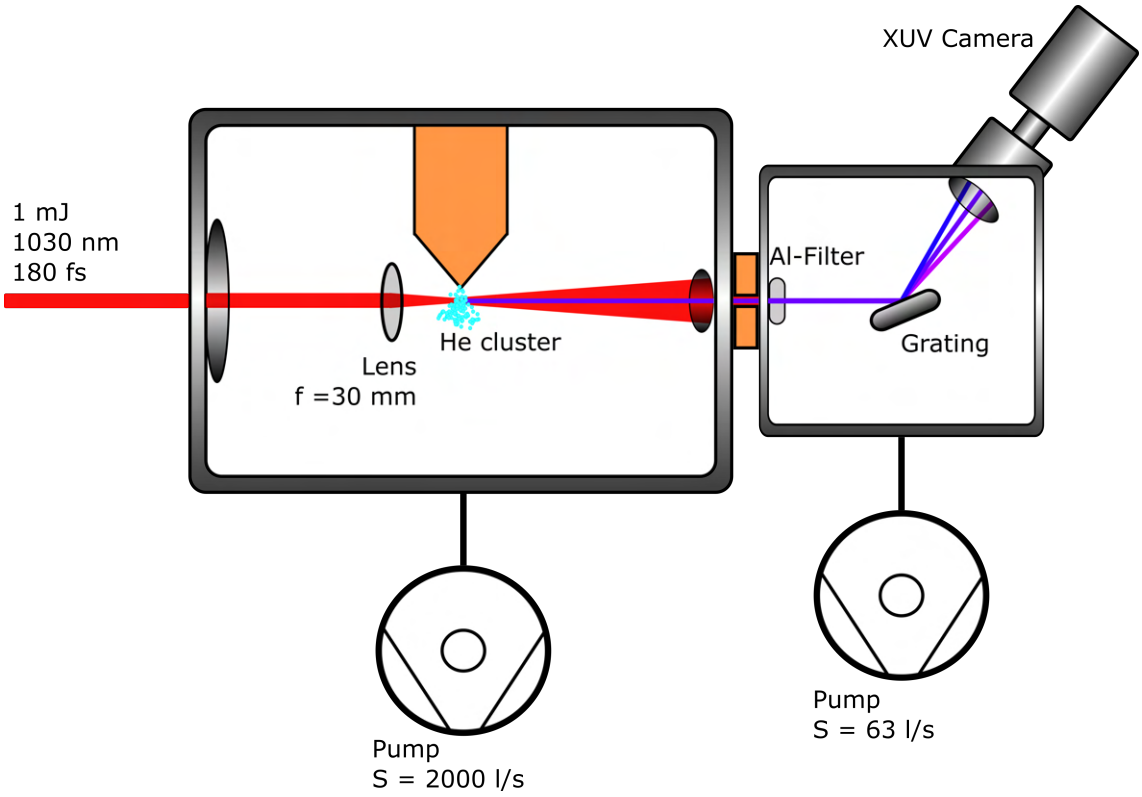

Fig. 3.7: Schematic depiction of the vacuum system with the first chamber on the left housing the cryostat and the second chamber on the right containing the spectrometer setup. The IR laser beam enters the left chamber from the left side and is focused onto the clusters via a lens with a focal length of 30 mm. The remaining IR photons and any generated XUV light passes into the second chamber, where an Al filter blocks the remaining drive laser power. A grating then disperses the generated XUV fluorescence onto the XUV camera.

The first chamber houses the cryostat and is pumped by a turbomolecular vacuum pump (Leybold) with a pumping speed of $S = 2000\,\mathrm{l/s}$ in order to keep the pressure in the chamber below 10^{-4} mbar. At higher pressures the heat conductivity of the helium gas in the chamber is too large for the cryostat to maintain temperatures less than 10 K. The target chamber also contains a lens with a focal length of 30 mm that focuses the incoming IR laser pulses onto the clusters after they leave the nozzle.

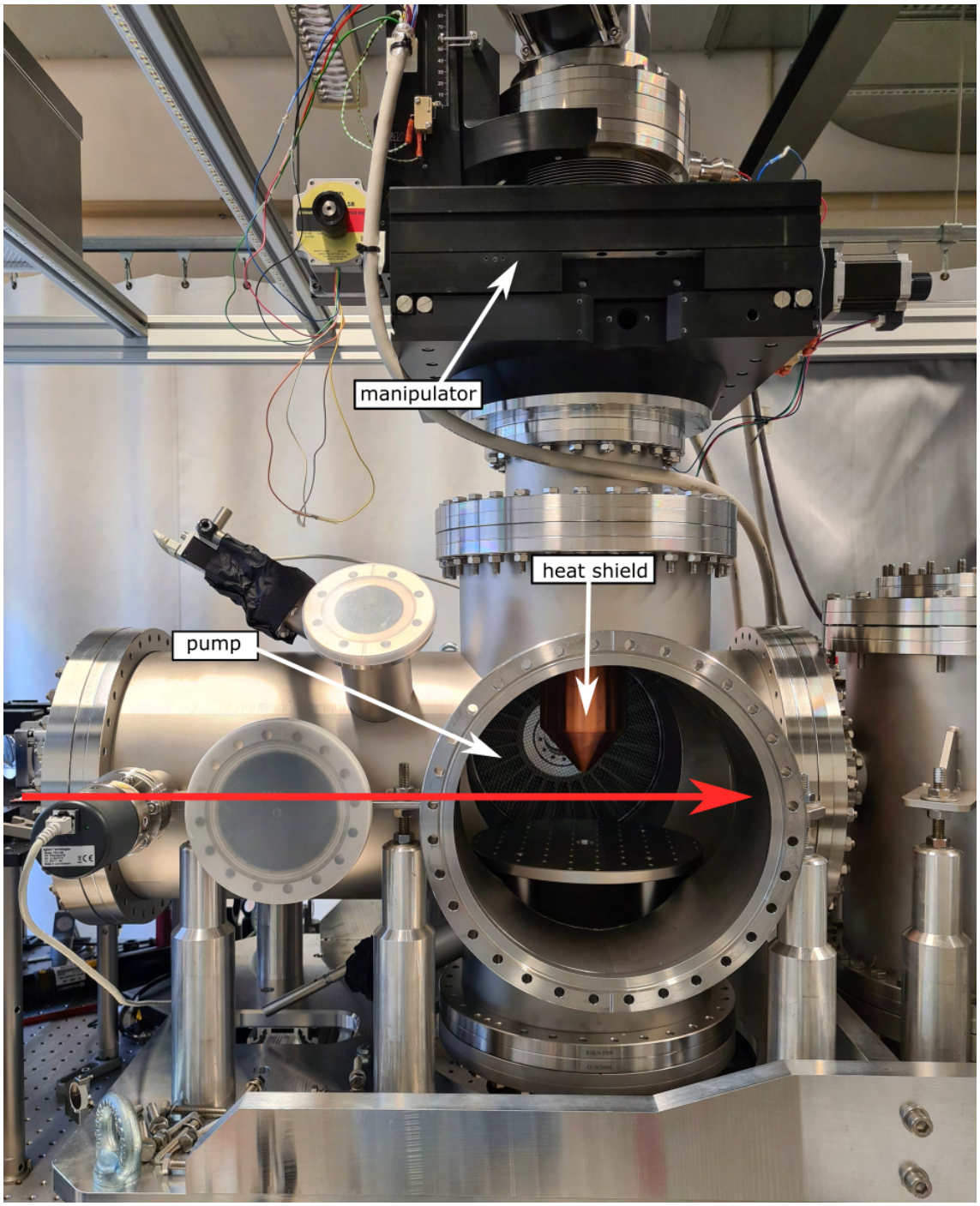

Fig. 3.8: Picture of the helium source chamber. The direction of the IR laser beam is shown as the red arrow. On the right side of the chamber one can see part of the spectrometer grating chamber.

The second chamber is the spectrometer chamber. It houses the XUV grating with 1200 groves per mm (Hitachi), as well as the XUV camera that is used to record the dispersed light (ANDOR). The grating is mounted on a linear and a rotation stage. The linear stage allows the grating to be moved vertically into and out of the generated XUV beam that passes the aperture. If the grating is moved out, then the XUV light passes into a third chamber dedicated to study light-matter interaction at short XUV and soft x-ray wavelength. The rotation stage allows the grating to be rotated around the vertical axis. This allows different parts of the spectrum to be projected onto the XUV camera. In order to reduce the amount of stray light impinging on the XUV camera, the inside of the chamber and all the interior components have been coated with graphite as can be seen in Figure 3.9:

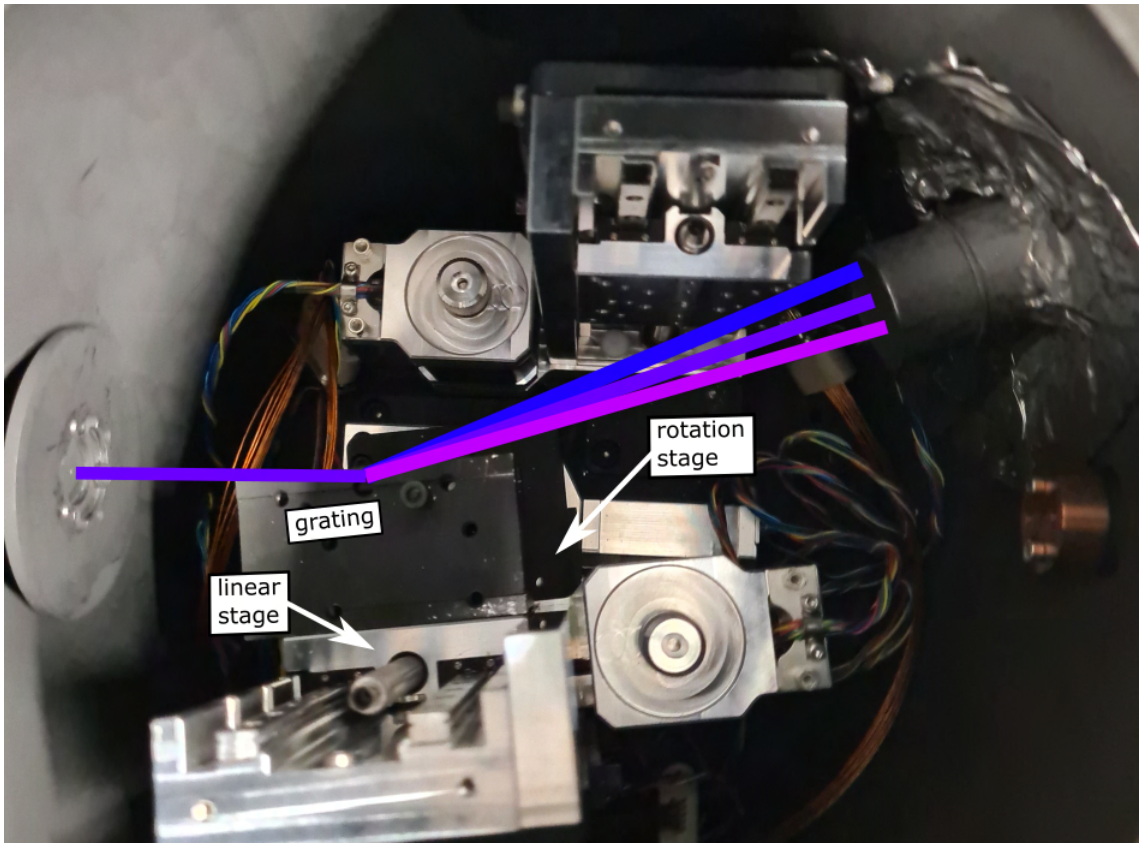

Fig. 3.9: Picture of the inside of the grating chamber. On the left side one sees the end-part of the IR laser absorber block (gray disc). The generated XUV light (purple line) enters the chamber and hits the grating. The light that is reflected of the grating propagates towards the XUV camera via the black tube in the upper right of the chamber.

The two chambers are separated by the IR absorber block. This block needs to fulfill several functions at once. First of all, it needs to act as a compression stroke between the two chambers that are operating at different vacuum pressures (10^{-4} mbar and 10^{-6} mbar, respectively) and therefore needs to minimize gas flow between the chambers by minimizing the effective aperture size. The second task is to suppress the remaining light of the IR drive laser, since the spectrometer detects all photons that propagate collinearly with the drive laser. This requires the use of a 200 nm thick aluminium foil as a transmission filter that lets XUV light pass but blocks 1030 nm and 2060 nm light. However, the foil alone cannot withstand the up to 20 W of power of the drive laser. Therefore, a small aperture has to be used to block most of the diverging IR drive laser and thereby most of the power. The remaining light then shines onto the foil minimizing the amount of stray 1030 nm or 2060 nm light that manages to enter the second chamber. Especially during evacuation of the chambers one has to be careful, because the pressure gradient might become to large for the foil to withstand. This can be remedied by installing venting holes into the absorber block that allows large pressure differentials to dissipate when venting and pumping down. However, this is in direct opposition to the first task, which was differential pumping. In order to mediate this conflict we designed the venting slits with several layers of stray light suppression in mind. The IR absorber block also has connectors for cooling water to reduce the heat load. The resulting design is shown in Figure 3.10.

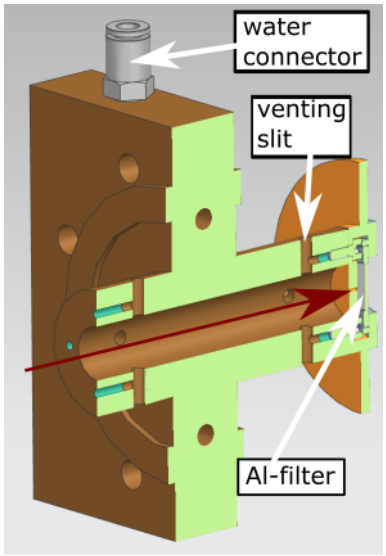

Fig. 3.10: Sectional view of the CAD model of the IR absorber block. The IR laser pulses and the generated XUV light enter the inner cylinder from the left side (red arrow). The aperture (bright orange) has a screen that extends to a larger radius than the cylinder does. This piece reduces the amount of scattered light that enters the chamber through the venting slits by requiring more bounces on surfaces before it gets into the second chamber.

3.4 XUV spectrometer

Special emphasis shall be put on the spectrometer geometry, since the aperture acts as a pinhole camera, which will be used to obtain spatial resolution along the vertical helium droplet beam axis. This is illustrated in Figure 3.11:

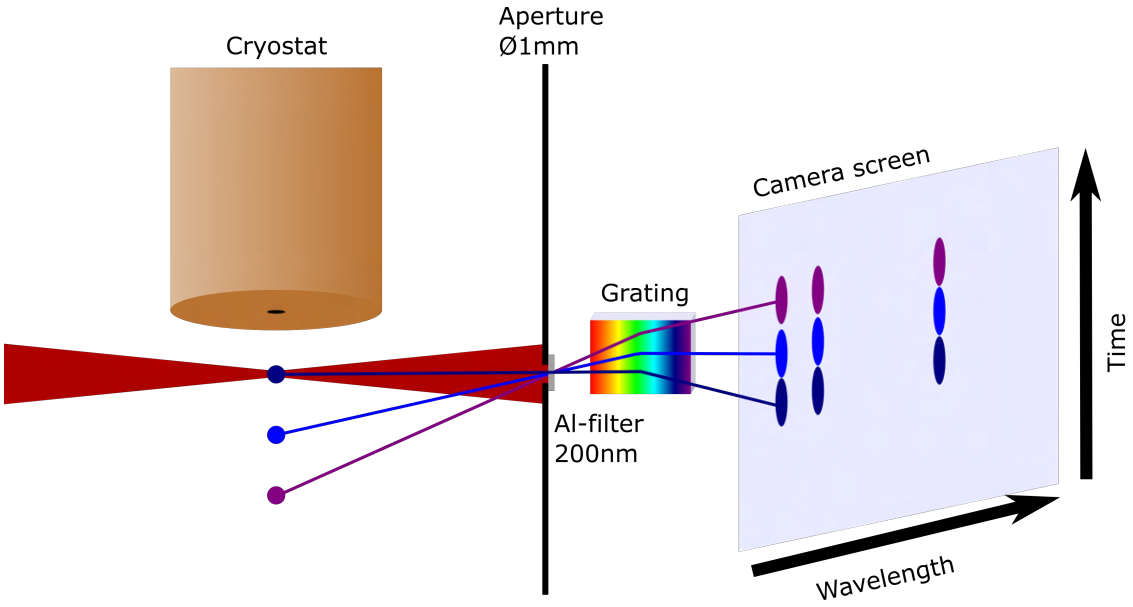

Fig. 3.11: Schematic depiction of the pinhole camera function of the spectrometer setup. Light, which is emitted further away from the cryostat nozzle (purple), is projected by the aperture onto a higher vertical position on the camera screen, than does light from closer to the nozzle (dark blue).

Atoms emit fluorescence light at different times depending on the lifetime of the electronically excited state. When they do, their vertical positions gets encoded via the geometry of the pinhole camera onto the vertical position of the camera pixel that detects the emitted fluorescence photon. From the distance between laser focus and aperture (284 mm) and the distance between aperture and camera screen (558 mm) one can calculate that photons emitted by a cluster, which has moved downwards by 1 mm are projected onto a vertical position on the chip (ΔS) by:

$$\Delta S = 1\,\text{mm} \times \frac{558\,\text{mm}}{284\,\text{mm}} = 1.96\,\text{mm} \tag{3.1}$$

Combining this relation with the fact that the camera has 512 pixel in the vertical direction and a single pixel has a size of 13 µm one can calculate the distance a cluster has traveled in the downward direction before the photon was emitted.

However, the finite size of the aperture also leads to a finite sized spot on the camera caused by photons emitted at identical times from the cluster. This smearing effect has to be taken into account when evaluating temporal information from the spatial position of the source point. This is also indicated in Figure 3.11 by the light from individual clusters spreading out vertically on the camera screen.

Chapter 4

Experimental Results

In this chapter, I analyze the fluorescence signal emitted in a wavelength range between 18 nm and 45 nm after illumination with the 180 fs long laser pulses at a central wavelength of 1030 nm as outlined in section 3.1. By moving the cryostat along the laser propagation axis (z-axis), the difference in radiative decay between clusters comprising on average 1.2×10^6 atoms and isolated atoms has been investigated.

4.1 Radiative decay in strong laser fields

The experimental procedure for comparing the radiative decay of ionized atoms and clusters is displayed in Figure 4.1. It utilizes the fact that the cluster jet is surrounded by a sheath of helium atoms that did not condense into clusters. By moving the cryostat so that the laser focus locates spatially either on the sheath of atoms or on the cluster jet, one can easily compare cluster and atomic fluorescence signal. The result is presented in Figure 4.2.

Looking at the radiative decay of atomic helium one can clearly see the $3p \rightarrow 1s$ fluorescence lines at 25.6 nm, $4p \rightarrow 1s$ at 24.3 nm, $5p \rightarrow 1s$ at 23.7 nm, as well as $6p \rightarrow 1s$ at 23.4 nm of He^+ ions. In the case of the focus position located spatially on the center of the cluster beam the same fluorescence lines show up with an overall higher signal strength. In addition, a new dominant contribution appears with a wide wavelength distribution that covers the spectral region from the $6p \rightarrow 1s$ fluorescence all the way to photon energies corresponding to the ionization potential of He^+ ions (22.78 nm or 54.4 eV). The additional broadband emission also has a different vertical profile compared to the fluorescence lines emitted from a beam of electronically excited atoms and ions, respectively. On the first view, one can see that it originates from fluorescing ions emitting further downstream from the nozzle than the initial 3 mm that separate the focus of the drive laser and the nozzle. The center of mass of the broadband emission, i.e. its source point is shifted to a larger distance of 3.3 mm. A vertical profile of the broadband emission for different

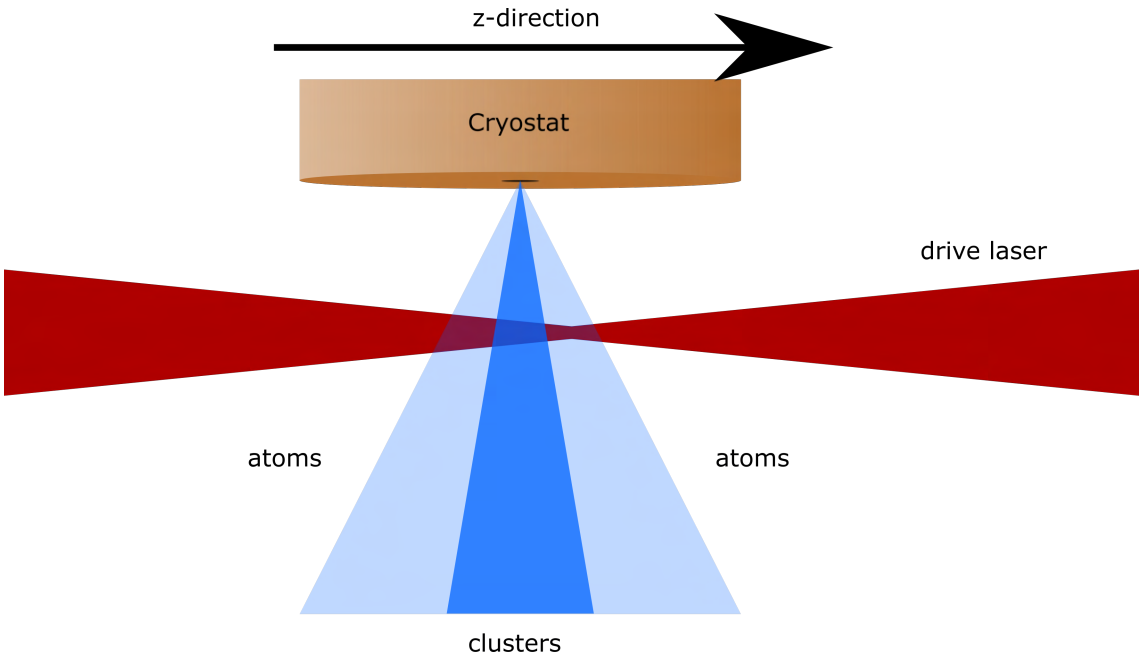

Fig. 4.1: Schematic depiction of the setup to seperate fluorescence signal from ionized atoms and clusters. The cryostat is moved along the propagation direction of the laser beam (z-direction). During this measurement the laser focus, i.e. the highest laser pulse intensity acts on atomic helium in the sheath around the cluster jet (light blue) or the cluster jet itself (dark blue).

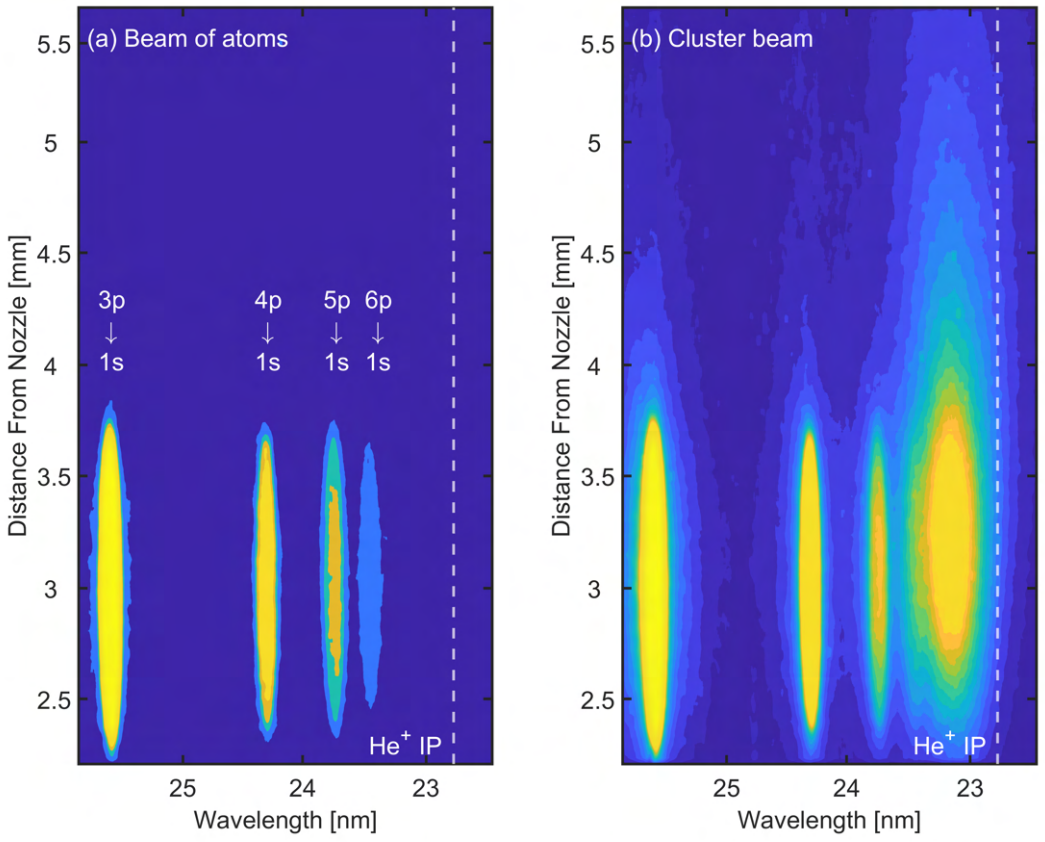

Fig. 4.2: Comparison between the camera pictures recorded with the laser focus located on the sheath of atomic helium a) and on the cluster jet b)

positions of the cryostat with respect to the laser focus is presented in Figure 4.3:

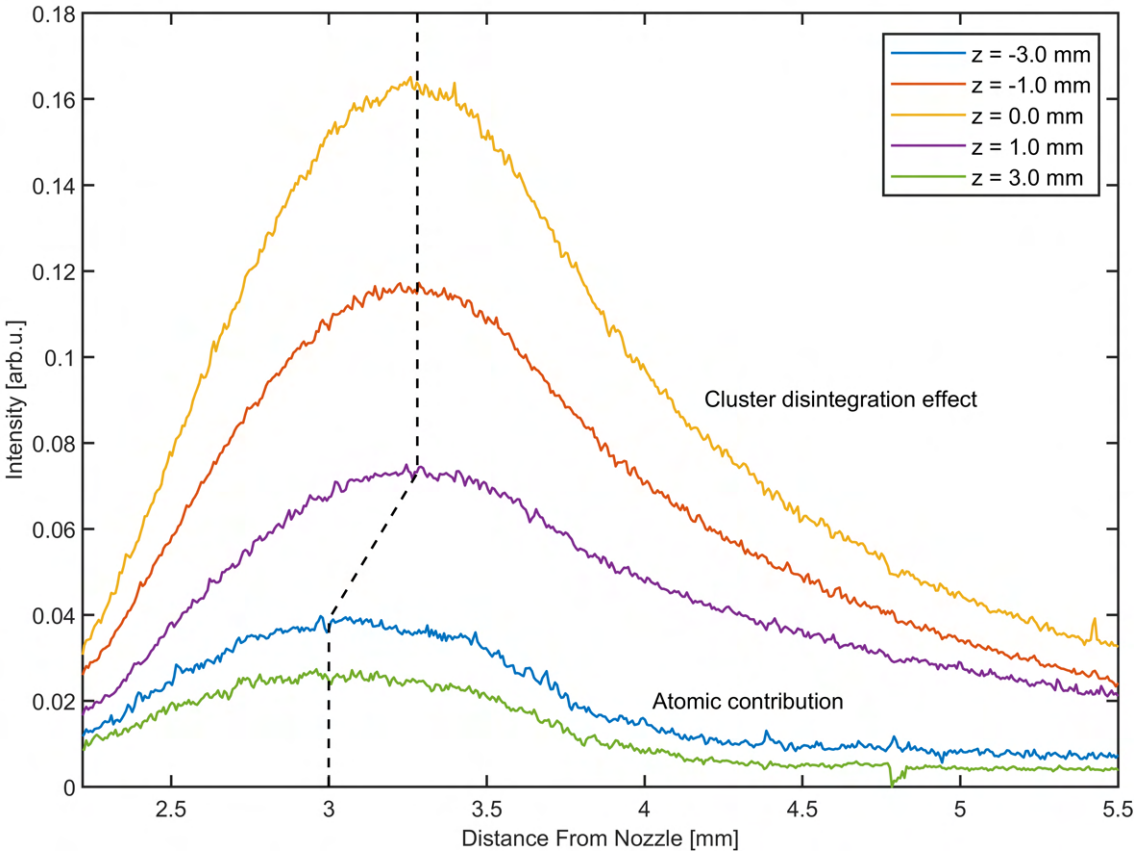

Fig. 4.3: Vertical profile of the broadband emission seen in Figure 4.2 for different horizontal positions of the cryostat along the z-axis. The profile was obtained by integrating the intensity of camera pixels, which record light within the wavelength range of 23.59 nm and 22.77 nm.

In Figure 4.3 it is apparent that the more the laser focus is positioned on the cluster beam (z = 0.0 mm) the stronger the overall fluorescence signal is, when scanning the laser focus horizontally between $z = 3.0\,\text{mm}$ and $z = -3.0\,\text{mm}$. The vertical center of mass of the new broadband emission is located at a distance of 3.3 mm from the nozzle compared to the regular (atomic) fluorescence signal at 3.0 mm downstream from the nozzle. Additionally, one observes that the vertical source point distance to the nozzle is not directly depended on the focus position as long as the focus is located within the central cluster jet, since the source point does not change between $z = -1.0\,\text{mm}$, $z = 0.0\,\text{mm}$ and $z = 1.0\,\text{mm}$. If the focus lies on the cluster beam position, the source point distance is always found 3.3 mm below the nozzle. Furthermore, a long tail towards even larger vertical distances appears once the focus position (highest laser intensity) impacts onto the cluster jet. A similar, but much smaller tail can be seen in the vertical readout of the $3p$-line as shown in Figure 4.4, which will be discussed later in this chapter.

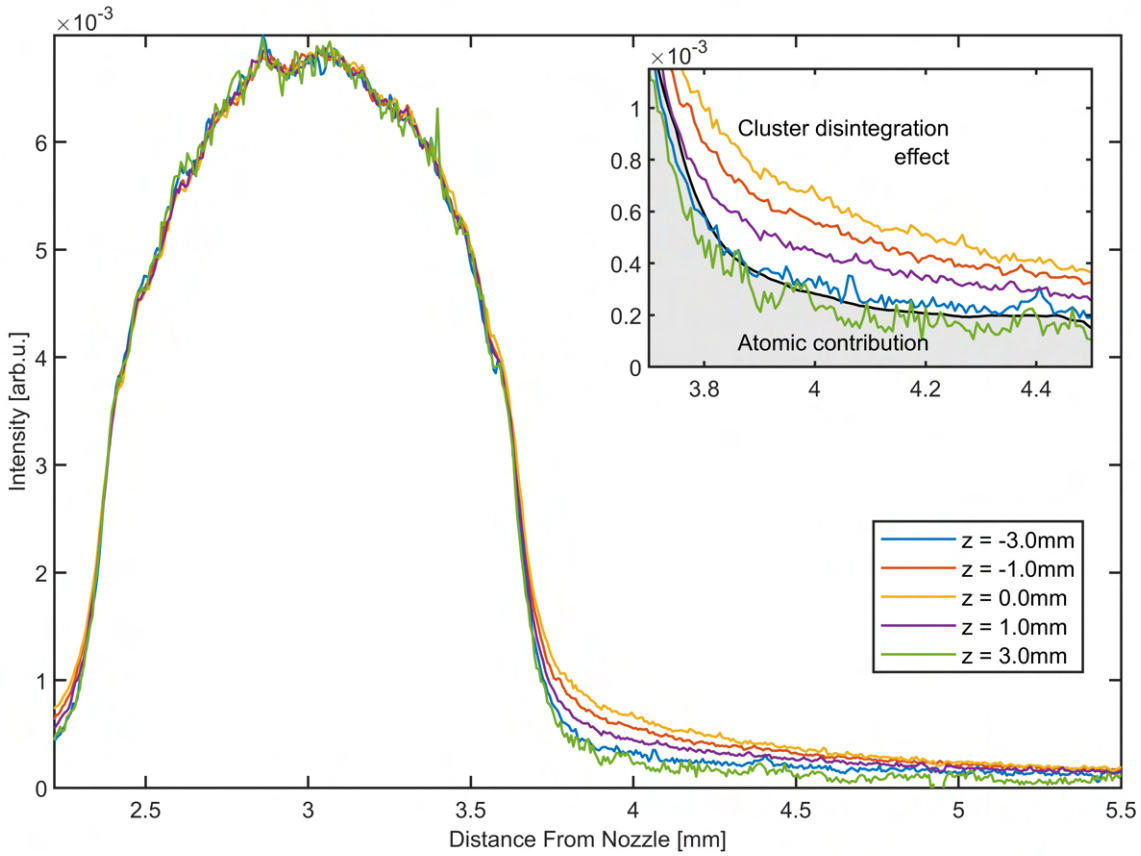

Fig. 4.4: Vertical readout of the $3p$-fluorescence line seen in Figure 4.2 for different horizontal positions of the cryostat along the z-axis. The profile was obtained by integrating the intensity of camera pixels, which record light within the wavelength range of 25.84 nm and 25.43 nm.

The origin of the broadband emission is the radiative transition of $n > 6$ states to the $1s$ state following the population of the higher states via three-body recombination (TBR) during the cooling down of the hot nanoplasma as described in subsection 2.3.4. Initially, the clusters are field-ionized by the intense laser pulse. During the outer ionization a positive cluster ion core is created, that prevents further outer ionization, while inner ionization continues. This leads to a trapping of quasifree electrons in illuminated helium clusters. During the expansion of the clusters driven by Coulomb and hydrodynamic forces the quasifree electrons cool down sufficiently for TBR to set in. This occurs at an electron temperature at which TBR proceeds according to the bottle neck model, where recombination happens predominantly into a small number of n-quantum number states above $n = 6$. These higher lying (Rydberg) states then radiativly decay into the $1s$-state. The photons from this decay show up on the camera spectrally above the $6p$-fluorescence line, which is only weakly populated upon interaction of intense IR pulses with the beam of helium atoms. The bottle neck model also explains the absence of the broadband Rydberg emission in the data recorded from atomic helium. Because quasifree electrons are trapped inside the helium cluster in a nanoplasma, the local plasma electron density is much higher than the average electron density inside the entire focal volume.

Obviously, the high electron density inside clusters promotes TBR resulting in the population of high-lying Rydberg states. In the case of illuminated helium gas, no such quasifree electrons exist. Here, the lack of local electron density maxima in the vicinity of laser-generated ions results in a much reduced TBR rate into Rydberg states, which explains the absence of the corresponding spectrally broad emission band. See Figure 4.5 for a symbolic depiction of the electron density distribution in the two different experimental scenarios.

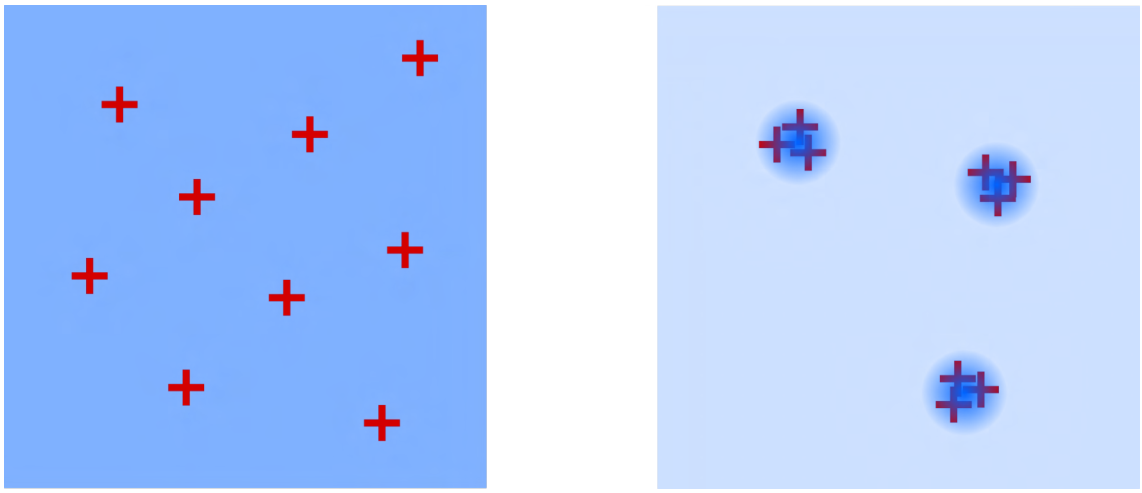

Fig. 4.5: Schematic display of electron density in ionized plasma when illuminating atoms (left) and clusters (right), respectively. The positive charges due to ions are display as red pluses, while the electron density is displayed in blue, with higher saturation meaning higher density.

The vertical displacement of the source point for the broadband emission from high-lying Rydberg states and the tail of the lower lying n-state fluorescence lines from illuminated helium clusters share a common origin. Its is an effect that is due to the cluster disintegration driven by Coulomb and hydrodynamic forces. The rapidly increasing net charge of the clusters in the course of the massive energy deposition and outer ionization accompanied by the continuously increasing temperature of the quasifree electrons lead to the expansion of the cluster. This results in individual ions gaining up to several keV of kinetic energy. During the time between a quasifree electron populating a p-state and its radiative transition to the $1s$-state the ion moves a distance away from the focus position of the IR laser beam generating the transient nanoplasma. The pinhole camera allows detection of the vertical component of this ion movement by projecting the fluorescence source point onto a different vertical position on the camera chip. Since this movement depends on the Coulomb explosion and hydrodynamic expansion of clusters, it does not show up in the measurements with atomic helium explaining the findings in Figure 4.2 a). Once the Coulomb explosion occurs, the distance an ion travels before radiating a photon only depends on the lifetime of the electronically excited state. Accordingly, the length of the tail should scale with the n-quantum number of the populated p-state. Qualitatively, we find exactly this behavior in our experiments as shown in Figure 4.6, where

the normalized vertical profiles of all detected fluorescence bands from illuminated clusters are plotted. The higher-lying p-state emissions do indeed show longer tails then the lower-lying ones. According to the literature, their lifetime vary from 374 ps for the 3p-state to 3.2 ns for the 6p-state [74]. Thus, the electronically excited ions with keV kinetic energy from the disintegrating cluster (nanoplasma) have more time to move away from the nozzle before radiative decay takes place.

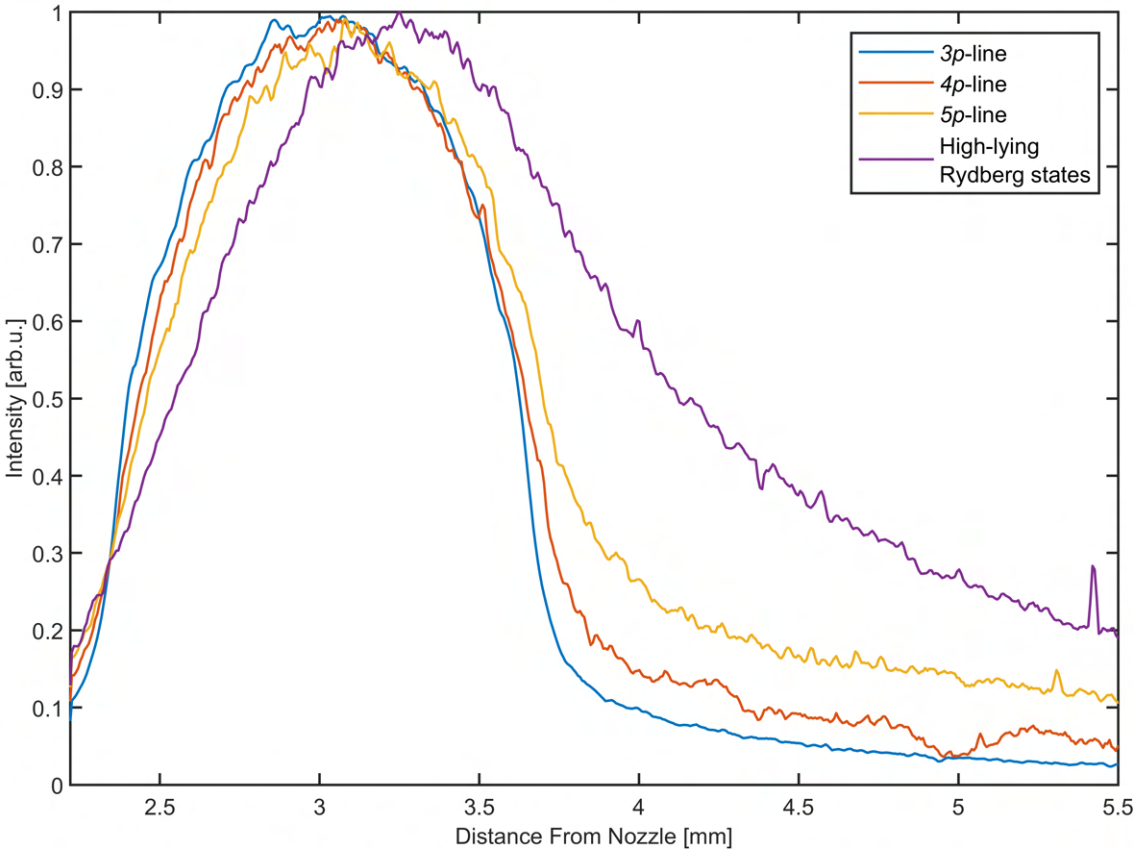

Fig. 4.6: Normalized vertical readout of the individual fluorescence lines including broadband Rydberg-state emission from illuminated helium clusters (recorded at z=0). The profiles were obtained by integrating the intensity of camera pixels, which record light within the wavelength range of 24.46 nm and 24.16 nm for the 4p-fluorescence line, 23.88 nm and 23.63 nm for the 5p-fluorescence line and the same ranges for the 3p-fluorescence line and the high-lying Rydberg states as shown in Figure 4.3 and Figure 4.4.

The population of high-lying Rydberg states involves additional steps compared to the lower-lying fluorescence lines. While the 3p-, 4p-, 5p- and to some extent also 6p-states are populated during the laser pulse interaction determined by the pulse length, the high-lying Rydberg states are populated somewhat later. This happens, when the expansion process has sufficiently cooled-down the quasifree electrons so that TBR can set in. Thus, the maximum of the Rydberg emission is reached once the nanoplasma potential is significantly lowered at reduced ion density and electron temperature. In other words, the electronically excited ions of the expanding helium nanoplasma have already moved a significant distance away from the focus position, before radiative decay takes place. This explains the spatial shift in the maximum

position of the fluorescence source point in Figure 4.6.

Finally, I would like to discuss the observation in Figure 4.2 that the long tails of the lower-lying fluorescence lines and the general shape of the broadband Rydberg emission are asymmetric with regards to the vertical axis, although the Coulomb explosion and hydrodynamic expansion that causes these dynamical processes is isotropic in nature. A possible and straight forward explanation is simply that closer towards the nozzle the ion and atom density markedly increases, which significantly enhances self-absorption. The effect might block the light emitted by ions that are pushed towards the nozzle by the Coulomb explosion resulting in the asymmetry we detect in Figure 4.2.

4.2 Cluster size dependence of energy deposition, dissipation and radiative decay

In the next set of measurements, I investigated the behavior of the population of high-lying Rydberg states as a function of cluster size $\hat{N}$ in the range of $1.2 \times 10^5 < \hat{N} < 1.6 \times 10^{10}$. For this study the z-position of the cryostat was set to the horizontal position along the laser beam propagation direction resulting in maximum signal strength of the broadband Rydberg emission. With the cluster jet located at the laser beam waist, the temperature of the cryostat was varied to change the average size of the generated clusters. An overview of different camera pictures recorded for different cluster sizes is shown in Figure 4.7 a)-f). Several trends can be identified, each of which will be discussed in the following chapters.

4.2.1 Spatial distribution of fluorescence emitters affected by the He nanoplasma expansion

Most prominent is the change in the spatial shape of the Rydberg emission. For small clusters it is elongated and stretches to the top of the camera chip. With increasing average size of the clusters, the broadband emission becomes less and less elongated and overall weaker compared to the intensity of the $3p$-fluorescence line. The Rydberg signal completely disappears for the largest clusters as shown in Figure 4.7 f). The change in the vertical extension points to a change in the recoil energies caused by the cluster disintegration. It is important to note that we measure the distance traveled before the emission of a fluorescence photon and the life time is independent of cluster size leaving only the kinetic energy of the ions as the changing variable. The reduction in kinetic energy with cluster size can also be seen in the vertical distributions of the $5p$-fluorescence line in Figure 4.7. The long tails become shorter the larger the clusters are as shown in Figure 4.8.

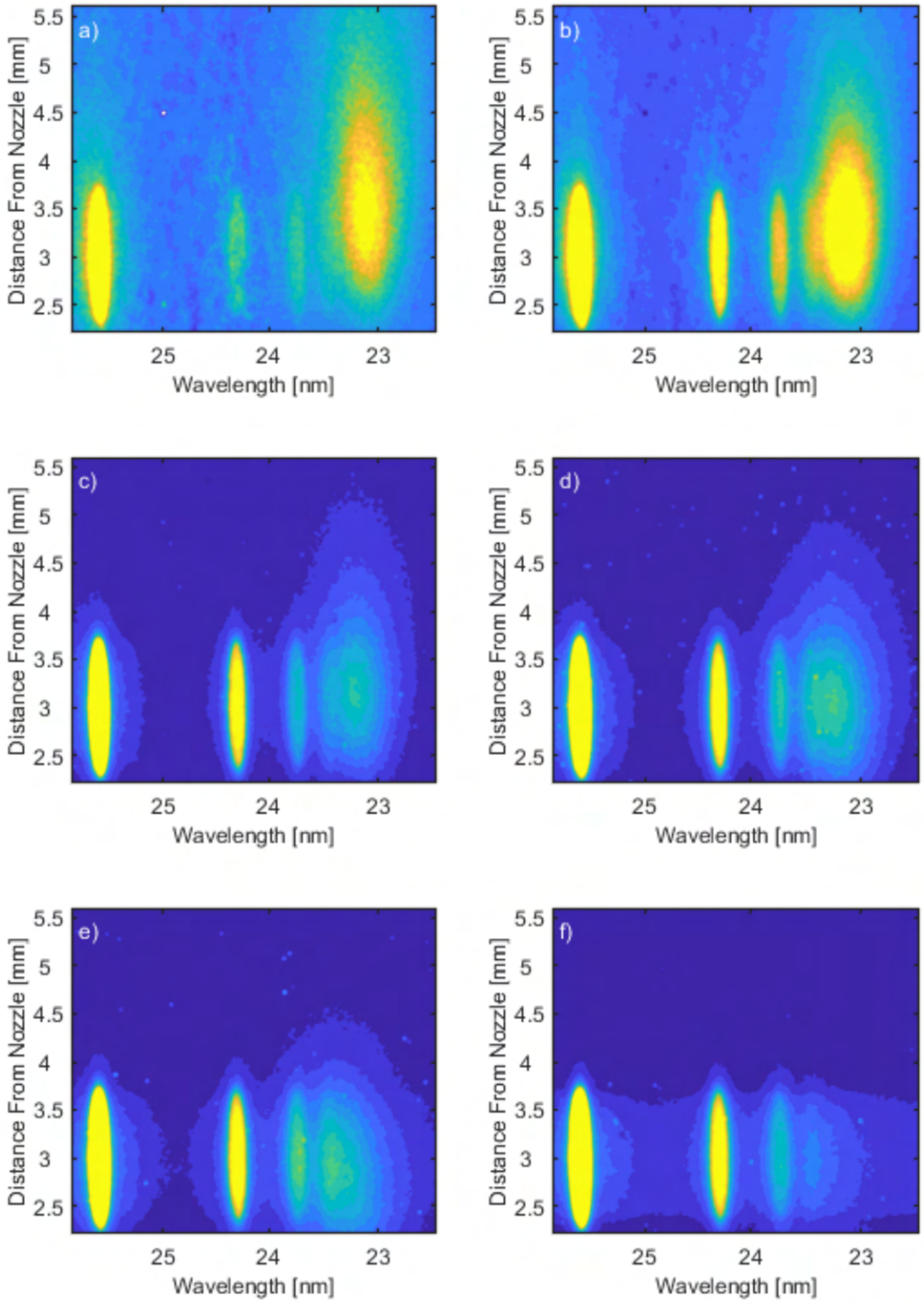

Fig. 4.7: Measured camera pictures for cluster beams with different average number of atoms per cluster: a) 1.2×10^5, b) 3.3×10^5, c) 2.7×10^6, d) 8.6×10^6, e) 2.3×10^8, f) 1.6×10^{10}. Each image is normalized to the intensity of the $3p$-fluorescence line

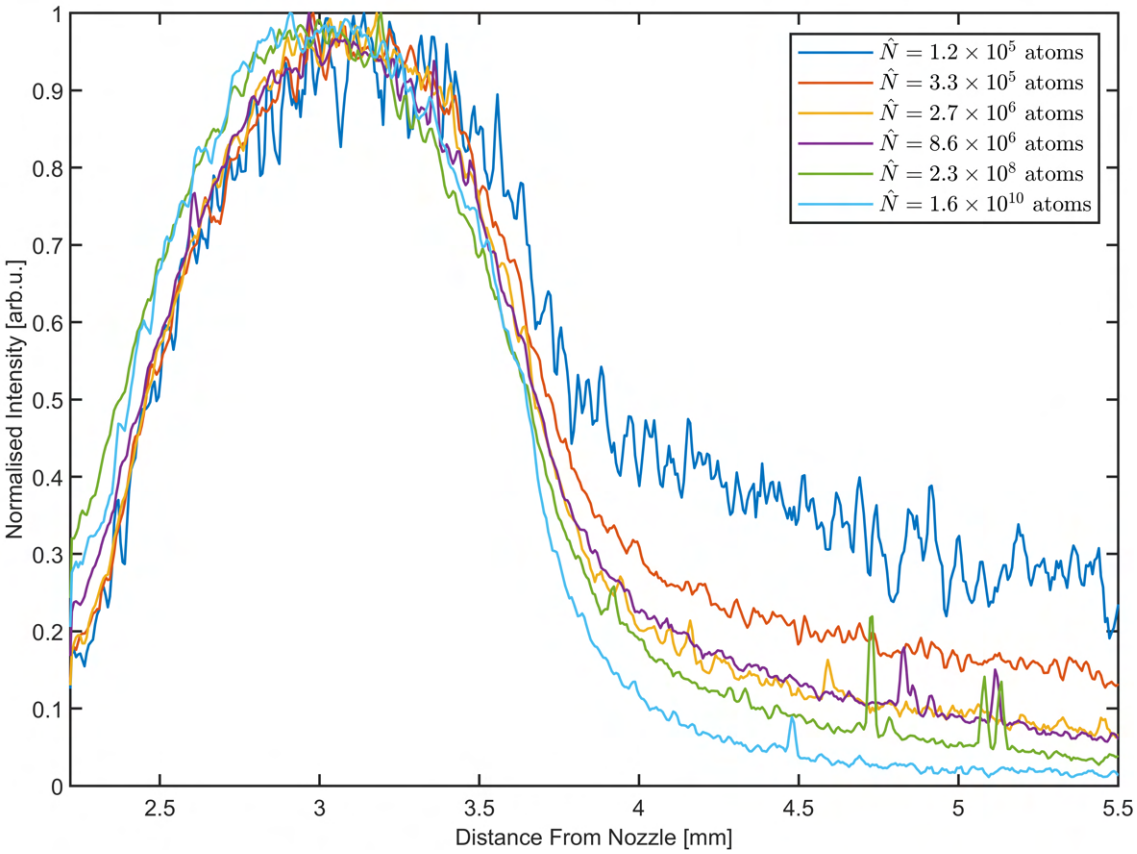

Fig. 4.8: Normalized vertical distributions of the 5*p*-line for the cluster sizes used in Figure 4.7

The change in the vertical distribution of the broadband Rydberg emission is even more pronounced. The total distance the ions travel before emitting a photon in this spectral range can be separated into two parts. The first part is the distance traveled as a He^{2+} ion until TBR populates one of the high-lying Rydberg-states. The second part is the distance traveled as a He^{+} ion until the electronically excited state radiates out the photon. As the cluster size is increased, the peak temperature of quasifree electrons in the transient nanoplasma drops, since the mismatch between resonant plasma heating condition and laser pulse duration becomes larger (see subsection 2.3.3). Since the peak electron temperature is lower, the cluster has expanded by a smaller amount, when the temperature has fallen to levels that cause TBR to populate the high-lying Rydberg-states. This reduces the first part of the distance the Rydberg ion travels before emitting a photon. The second part of the total distance is reduced for the same reason as for the lower-lying fluorescence lines. The line of argumentation is as follows. Lower peak electron temperature leads to lower average charge state of ions due to reduced electron impact ionization. This reduces the strength of the hydrodynamic expansion force and the strength of the Coulomb expansion force, respectively. The resulting lower kinetic energy of the ions reduces the distance traveled before radiative decay takes place. The overall result is that both the tail gets shorter and the spatial position of the maximum emission moves closer to the focus position 3 mm in front of the nozzle. This can be

seen in the vertical fluorescence distributions normalized to the maximum shown in Figure 4.9.

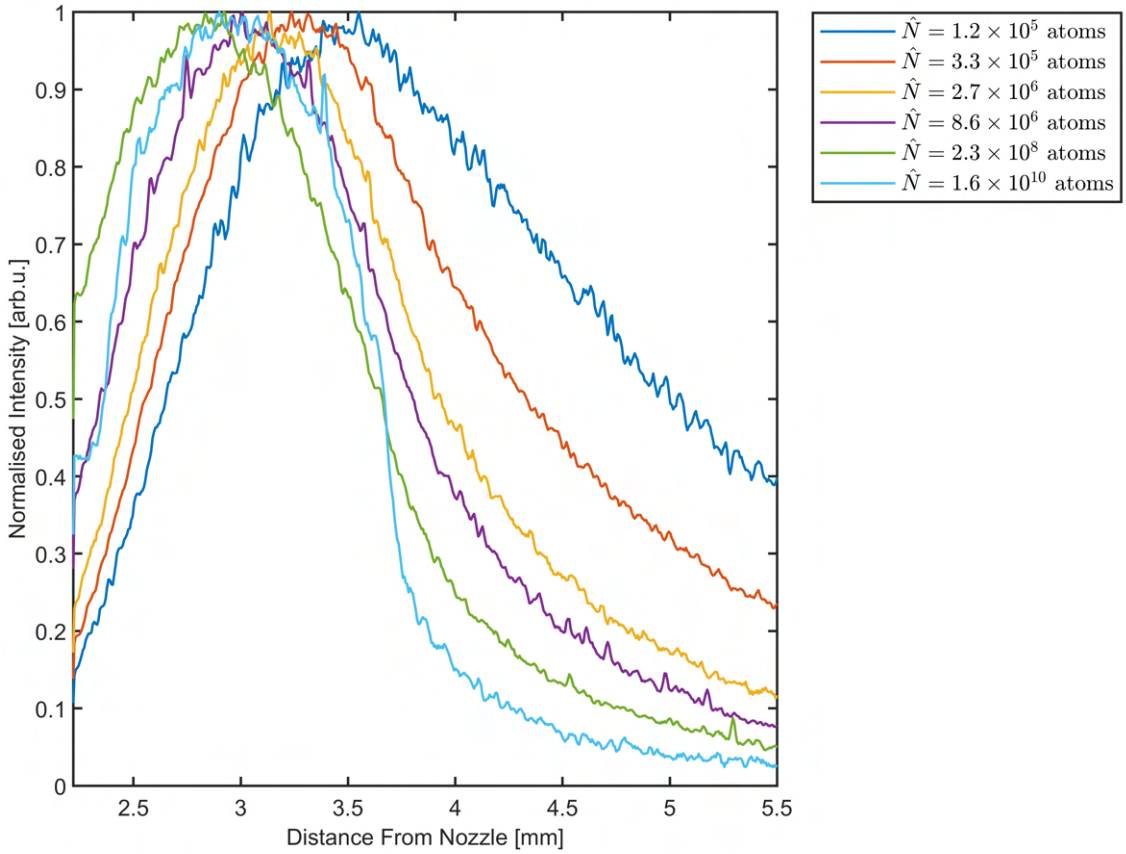

Fig. 4.9: Normalized vertical distributions of the broadband Rydberg emission as a function of cluster size

The distance from the nozzle of the center of mass of the Rydberg emission as a function of cluster size is shown in Figure 4.10. The center of mass of the source point is furthest away from the nozzle for clusters with an average size of 6.4×10^5 atoms. Both for smaller and larger clusters it shifts to smaller distances. The smaller distances from the nozzle point towards lower peak electron temperatures for cluster sizes other than 6.4×10^5 atoms. For larger clusters this observation is explained by the fact that the absorbed fraction of the laser pulse energy is distributed across more and more individual atoms and ions on top of the aforementioned mismatch between laser pulse duration and resonant plasma heating condition resulting in less efficient energy deposition. Therefore, peak electron temperature as well as kinetic energy per ion decreases with increasing number of atoms per cluster beyond 6.4×10^5. It results in the reduced travel distance from the nozzle before radiative decay. These dynamical processes can be observed directly in Figure 4.7 d) and e), where the effect of the long fluorescence tail is still clearly visible, yet the shift of the emission center is already gone. Clusters smaller than 6.4×10^5 atoms reach the resonant heating condition before the peak intensity of the drive laser is reached (see subsection 2.3.3). The corresponding mismatch in time between highest intensity of

the drive laser and most efficient absorption of laser light also reduces the amount of energy absorbed per atom. Less absorbed energy leads to a reduced kinetic energy of the ions and reduced peak electron temperature in the transient helium nanoplasma, which in turn results in a smaller Rydberg ion distance to the nozzle at the time of fluorescence photon emission.

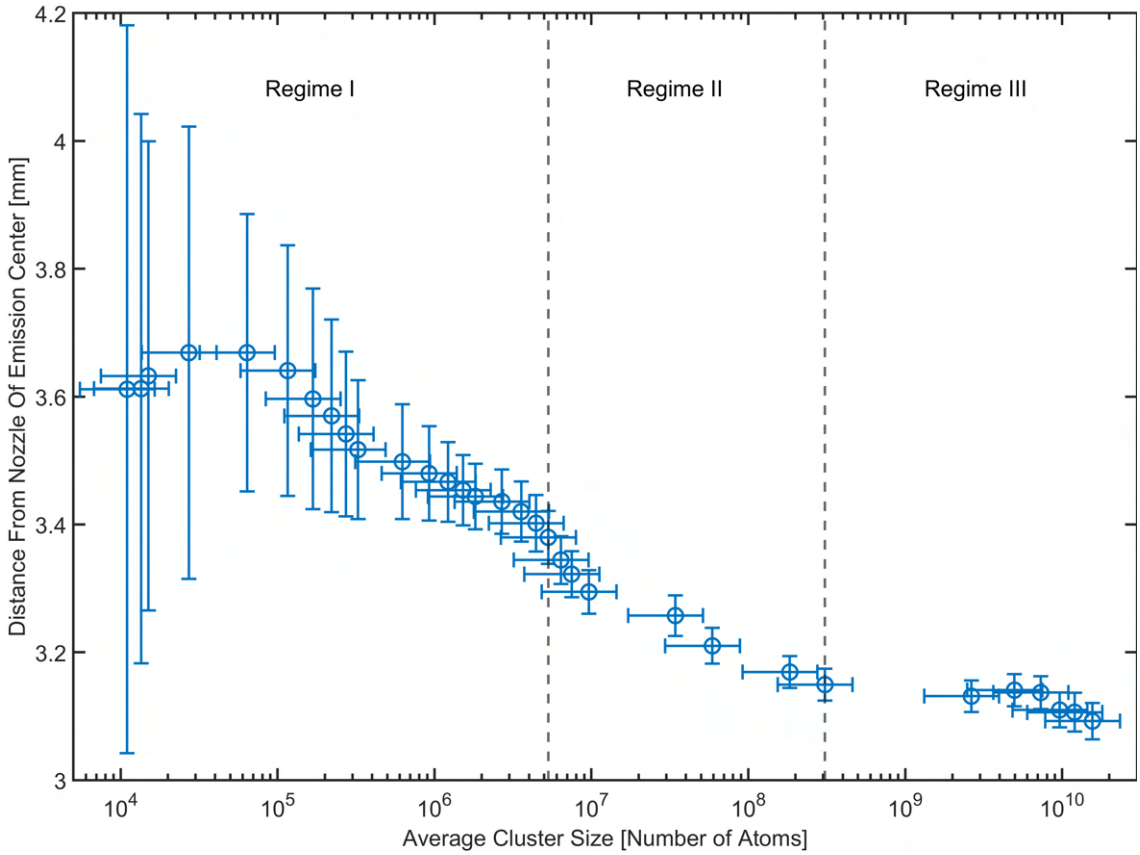

Fig. 4.10: Measured distance from the nozzle of the center of mass of the broadband Rydberg emission. The dashed lines mark the separation of the different cluster generation regimes (see section 2.1). The horizontal confidence intervals were obtained by assuming a width of the cluster size distribution equal to the average cluster size. The vertical error bars were obtained by assuming that each camera pixel has a confidence interval equal to the square root of its recorded intensity. Since overall intensity drops the smaller the average cluster size is, the larger the vertical confidence interval becomes.

4.2.2 Population and decay of electronically excited states in He nanoplasma as a function of cluster size

The second striking observation in Figure 4.7 is the change in the relative and absolute signal strength of the Rydberg emission with cluster size. Its total fluorescence yield increases by more than four orders of magnitude across the measured size range and the same holds true for the $3p$-fluorescence line. This observation is less apparent in Figure 4.7, since all images are normalized to the intensity of the $3p$-emission, but can still be seen by comparing the individual line strengths to the background. To make it clear, the strengths of these two prominent emission bands are plotted as

a function of cluster size in Figure 4.11 a). The dramatic signal increase is caused by the increased density of helium at lower nozzle temperature leading to an increased mass flow through the nozzle and into the focus volume. Additionally, the opening angle of the helium jet after leaving the nozzle decreases with lower temperatures and therefore with larger average cluster sizes. Both effects lead to a higher helium density in the focus volume resulting in a stronger fluorescence signal. For the largest average helium droplet size (Regime III) the total fluorescence yield does not increase further. The reason is that the individual clusters are large enough for the emission from inner parts of the droplet to be quenched by self absorption in outer shells or by collision-induced non-radiative decay processes.

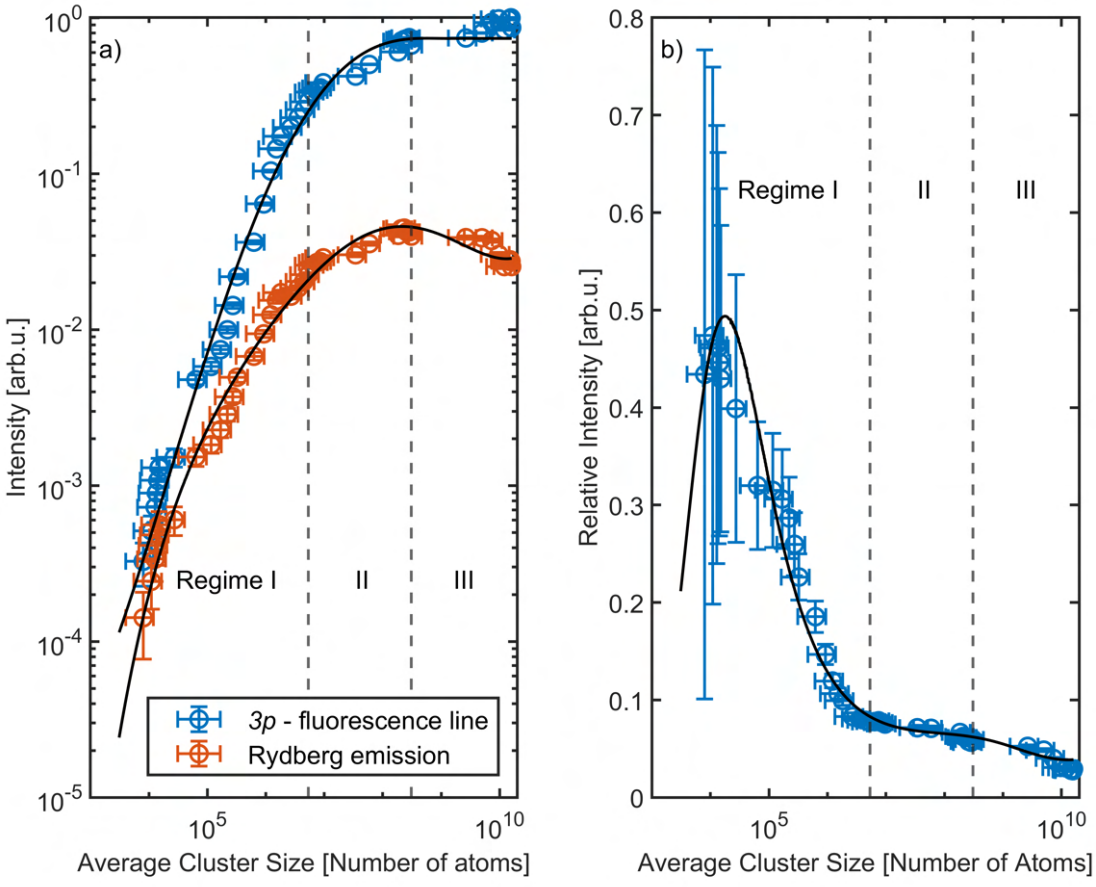

Fig. 4.11: a) Total yield of the $3p$-fluorescence line and the Rydberg emission measured as a function of average cluster size. b) The relative intensity of the Rydberg emission compared to the $3p$-fluorescence line as a function of average cluster size. The black solid lines are added as guide to the eye, while the dashed lines mark the separation of the different cluster generation regimes (see section 2.1).

More interesting is the relative signal strength of the Rydberg emission and the $3p$-fluorescence depending on the cluster size as displayed in Figure 4.11 b). It shows a clear and sharp maximum at an average cluster size comprising 1.1×10^4 atoms, a plateau across Regime II with average clusters size between 10^6 atoms and 2×10^8 atoms and a decay across Regime III. The sharp maximum in the relative population of Rydberg states is observed at a slightly different cluster size than the

optimal condition for efficient energy absorption (2.7×10^4 atoms) leading to the largest distance of the fluorescence source point from the laser focus as shown in Figure 4.10. However, due to the rather low fluorescence signal strength at these somewhat sizes the confidence intervals are large and overlap.

4.3 Radiative decay of clusters comprising 1.2×10^6 atoms

In the following section, the population of electronically excited Rydberg states due to three-body recombination in the laser-generated nanoplasma is studied as a function of pulse energy and pulse duration, i.e. peak intensity. The experiments where carried out at a cluster size of $\hat{N} = 1.2 \times 10^6$ atoms. The recorded fluorescence yields of the $3p$-line and the Rydberg emission are plotted in Figure 4.12 as a function of the laser pulse energy. As can be seen, the detected signal strength of both radiative decay channels scale linearly with the laser pulse energy.

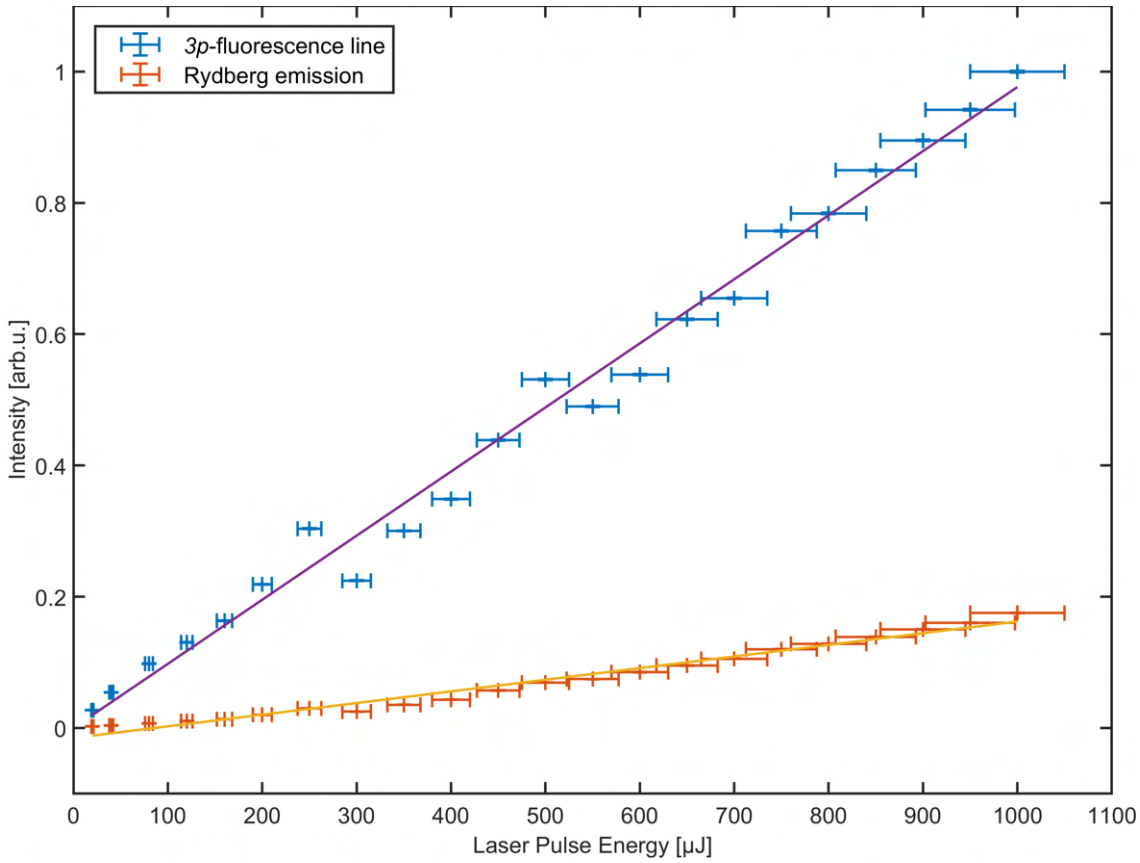

Fig. 4.12: Total fluorescence yield of the $3p$-fluorescence line and the Rydberg emission recorded as a function of laser pulse energy for clusters consisting of 1.2×10^6 atoms with a pulse duration of 180 fs. Both the $3p$ and the Rydberg emission show a linear dependence on the laser pulse energy as indicated by the linear fits.

Obviously, under these conditions the efficiency of thermal population of 3p states and three-body recombination into electronically excited Rydberg states scales linearly with the deposited energy into the nanoplasma. Repeating the same measurement but varying the pulse duration between 180 fs and 1.2 ps by adding varying amounts of GDD (see section 3.1) instead results in a different observation as displayed in Figure 4.13:

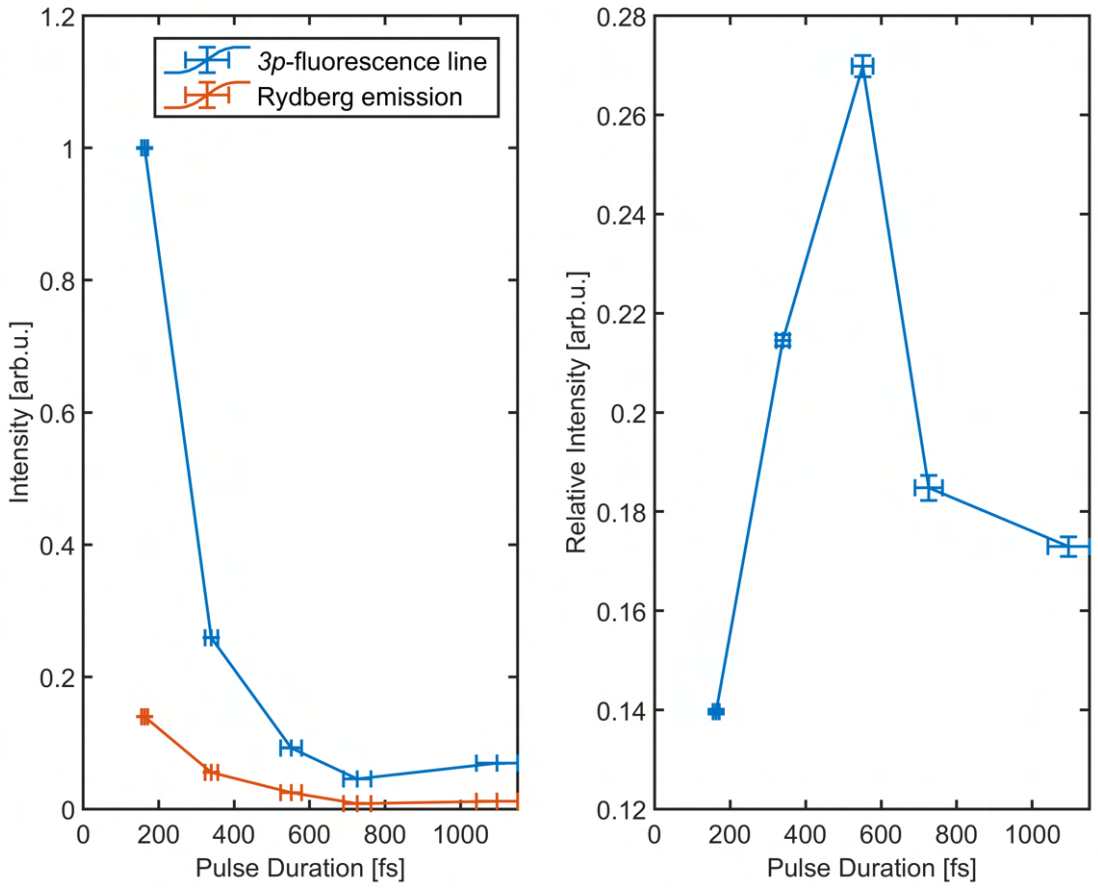

Fig. 4.13: Left: Total fluorescence yield of the 3p- and the Rydberg emission recorded as a function of laser pulse length for clusters consisting of 1.2×10^6 atoms and a pulse energy of 1000 µJ. Right: Ratio of the intensity of the Rydberg emission to the 3p-fluorescence line.

Here, one can clearly see that both the strength of the 3p-fluorescence line and the Rydberg emission decreases, when the clusters interact with pulses of the same energy but longer duration. This is to be expected since longer pulses with the same energy result in lower laser peak intensity and thus less efficient energy absorption. Note, the plasma heating rate scales with the ponderomotive potential (subsection 2.3.2) and therefore also with the intensity of the drive laser. When plotting the relative strength of these emissions from electronically excited states populated in the transient nanoplasma as a function of laser pulse duration (as done in Figure 4.13 right) a more interesting behavior is revealed. The Rydberg emission is strongest relative to the 3p-fluorescence at a pulse duration of 500 fs. This points to a stronger sensitivity of the three-body recombination rate into electron-

ically excited Rydberg states to the resonant plasma heating condition compared to the thermal 3p population. Since in the present measurement the clusters are larger than those generating the strongest Rydberg emission with a pulse duration of 180 fs, one expects slightly longer pulses to reach the resonant condition for efficient laser energy absorption. This is exactly what is observed.

4.4 Emergence of an XUV cluster continuum

For the largest helium droplets the Rydberg emission disappears completely. Instead, a new extremely broad continuum spectrum emerges. This can be seen in Figure 4.7 f). The appearance of the cluster continuum as a function of cluster size is displayed in Figure 4.14:

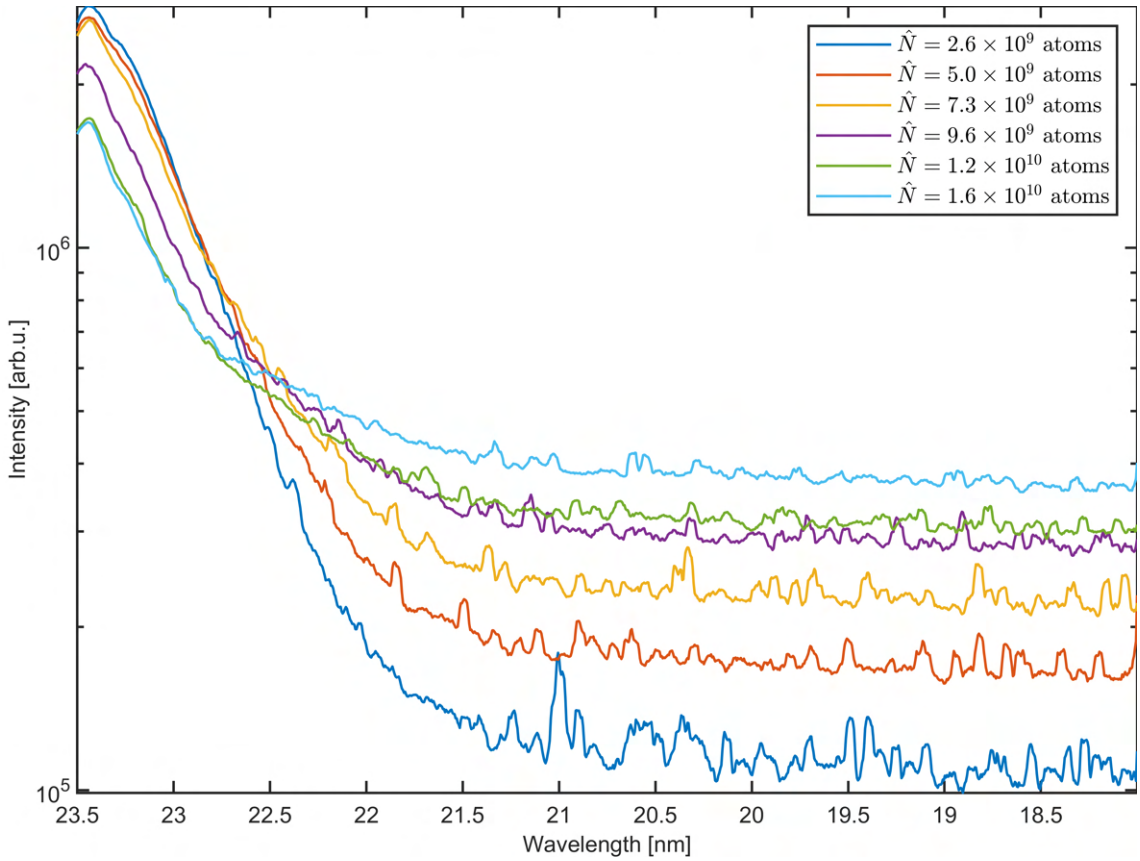

Fig. 4.14: XUV emission spectrum recorded for the largest clusters ranging from 2.6×10^9 atoms to 1.6×10^{10} atoms per cluster

The emission spectrum has an intensity profile that is completely flat across the entire detection range of the spectrometer spanning from the transmission edge of the Al-filter at 70 eV to minimum photon energy that can still be projected onto the camera by the grating, which is 21 eV.

To further analyze this broad emission band, I varied the pulse energy of the IR laser and measured the recorded signal strength of the cluster continuum in the

wavelength range between 31.46 nm and 40.55 nm compared to the 2*p*-fluorescence yield between 29.52 nm and 29.58 nm. The result is displayed in Figure 4.15:

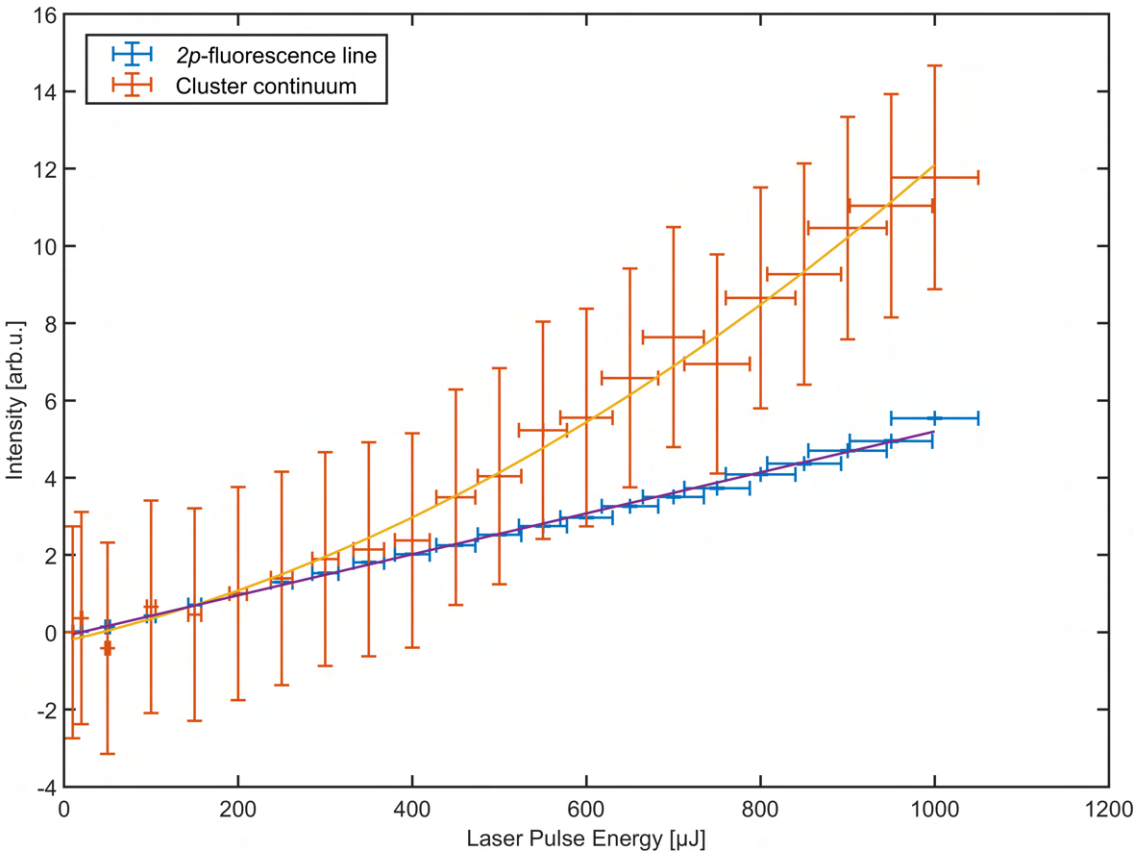

Fig. 4.15: Fluorescence yield of the 2*p*-fluorescence line and the cluster continuum detected as a function of laser pulse energy as well as a linear fit for the 2*p*-line intensity and a quadratic fit for the intensity of the broad cluster continuum.

In Figure 4.15 one can see that the intensity of the 2*p*-fluorescence line scales linearly with the energy of the laser pulses, while the cluster continuum scales quadratically with pulse energy. Explaining the origin of this cluster continuum has proven challenging. Its completely flat intensity profile rules out simple explanations like stemming from the recombination of thermal quasifree electrons or via bremsstrahlung emitted from the inside of the hot nanoplasma. In a recent publication, the authors mention the generation of a broad XUV emission spectrum, when using xenon clusters larger than 1 µm in diameter as target [75]. However, in the cited work the emission is much more structured as opposed to the flat spectrum observed here. The authors argue that it results from the overlap of many Xenon fluorescence lines emitted from different charge states of the atoms similar to the known XUV emission from solid targets [76].

In our experimental study of radiative decay in laser-driven helium nanoplasma this explanation does not apply, since helium atoms do not offer any additional fluorescence lines at wavelengths shorter than 22 nm. I conclude that additional measurements using different setups are necessary to understand the underlying

physics of the cluster continuum. First of all, further insight can be gained by utilizing a soft x-ray spectrometer capable of detecting the maximum photon energy generated in helium nanoplasma. One also needs to figure out, if this continuum is exclusively emitted in the direction of the drive laser pulse propagation or if it follows a different angular distribution or if the emission is isotropic. Another avenue for experimental investigation is the cluster size distribution. The present setup always generates a broad distribution of cluster sizes with a width on the order of the average cluster size. It is possible that only clusters of a certain size generate the broad spectrum and that the increase in the signal strength corresponds to a larger fraction of clusters meeting the size criterion. Ideally, one would utilize a cluster source capable of generating size-selected droplets with a laser system and spectrometer capable of single-shot operation.

Investigating the broad spectrum from the theoretical side poses its own number of hurdles. First of all, the XUV cluster continuum appears for the largest helium droplets beyond 2.6×10^9 atoms. In this case, the droplet diameter is of the same order of magnitude as the wavelength of the drive laser (8 µm to 1.03 µm) making the use of the dipole approximation questionable. Second of all, surface effects of the droplet have to be taken into account since the radius of curvature is also on the scale of µm. Third in line, are laser beam propagation effects inside the helium cluster. Those prove difficult to model, since basic constants such as the complex refractive index for helium clusters at soft x-ray and XUV wavelengths have not been measured and published. Fourth comes the fact that the cluster can no longer be assumed to turn into a homogeneous plasma complicating the modeling significantly. Finally, the large number of electrons and ions involved makes most simulation tools unavailable for the investigation of this process, as outlined in the earlier chapter on the hierarchy of models (see subsection 2.2.1).

4.5 Search for high-harmonic generation in helium droplets

By using the 180 fs long laser pulses with a central wavelegnth of 1030 nm no HHG light has been detected for all investigated cluster sizes that correspond to the mixed, bulk-like and bulk-liquid phase matching regimes as shown in Figure 2.11. The likely reason is the use of pulses with a duration of 180 fs, which corresponds to 52 optical cycles at a wavelength of 1030 nm. With such a large number of cycles it is likely that the cluster has been transformed into a helium nanoplasma before the peak intensity is reached, where efficient generation of XUV light might occur. Furthermore, once the nanoplasma is created it is not given that the phase relation between drive laser field and generated XUV light is still intact. The loss of this

relation would prevent the phase matching condition to be fulfilled. For the gas and gas-like regime, Equation 2.18 gives the reason for the lack of HHG signal. Given the wavelength $\lambda = 1030\,\mathrm{nm}$ and the spot size of $6\,\mu\mathrm{m}$, we obtain a minimum phase matching pressure of $p = 1013\,\mathrm{mbar} \cdot \frac{(1030\,\mathrm{nm})^2}{2\pi^2(6\,\mu\mathrm{m})^2} = 4.5\,\mathrm{mbar}$. Considering that the gas nozzle has a diameter of $5\,\mu\mathrm{m}$ and we apply a pressure of $20\,\mathrm{bar}$ and assuming an opening angle of 45° for the gas jet, we obtain the $4.5\,\mathrm{mbar}$ at a distance from the nozzle of $166\,\mu\mathrm{m}$. This is much closer to the nozzle than the $3\,\mathrm{mm}$ used in the experiment. Even when considering that we can cool-down the gas to $30\,\mathrm{K}$ before clustering sets in and therefore obtain the same gas density as if we applied $200\,\mathrm{bar}$ to the nozzle, we would still have to put the focus closer than $527\,\mu\mathrm{m}$ to the nozzle. Because of the geometry of the cryostat heat shield, this was not possible. Therefore, we could not achieve phase matching in the gas and gas-like regime with our setup.

4.6 First steps towards the interaction of helium clusters with few-cycle laser pulses

Since significant changes in the energy deposition and redistribution processes can be suspected when using drive laser pulses with a much smaller number of cycles, we utilized $50\,\mathrm{fs}$ pulses with a central wavelength of $2060\,\mathrm{nm}$ for the final set of measurements. Thereby, we reduce the number of optical cycles in the interaction with helium clusters from 52.5 for $180\,\mathrm{fs}$ pulses at $1030\,\mathrm{nm}$ discussed in section section 3.1 to 7.3 cycles for the present set of laser parameters. The recorded camera pictures for different cluster sizes are presented in Figure 4.16.

Two key findings are revealed by this data. First, the Rydberg emission is present for an average cluster size smaller than 3.1×10^8 atoms and its vertical extension decreases as the cluster size increases. For larger clusters it disappears completely. This trend is similar to the results from the earlier measurements with the $180\,\mathrm{fs}$ $1030\,\mathrm{nm}$ laser pulses. The similarity can be explained as follows. Since the Rydberg emission is caused by quasifree electrons recombining via TBR in corresponding electronically excited states and the vertical extension is an indication of the cluster disintegration, its behavior should not change significantly with drive laser parameters, as long as the overall heating of the nanoplasma remains essentially the same.

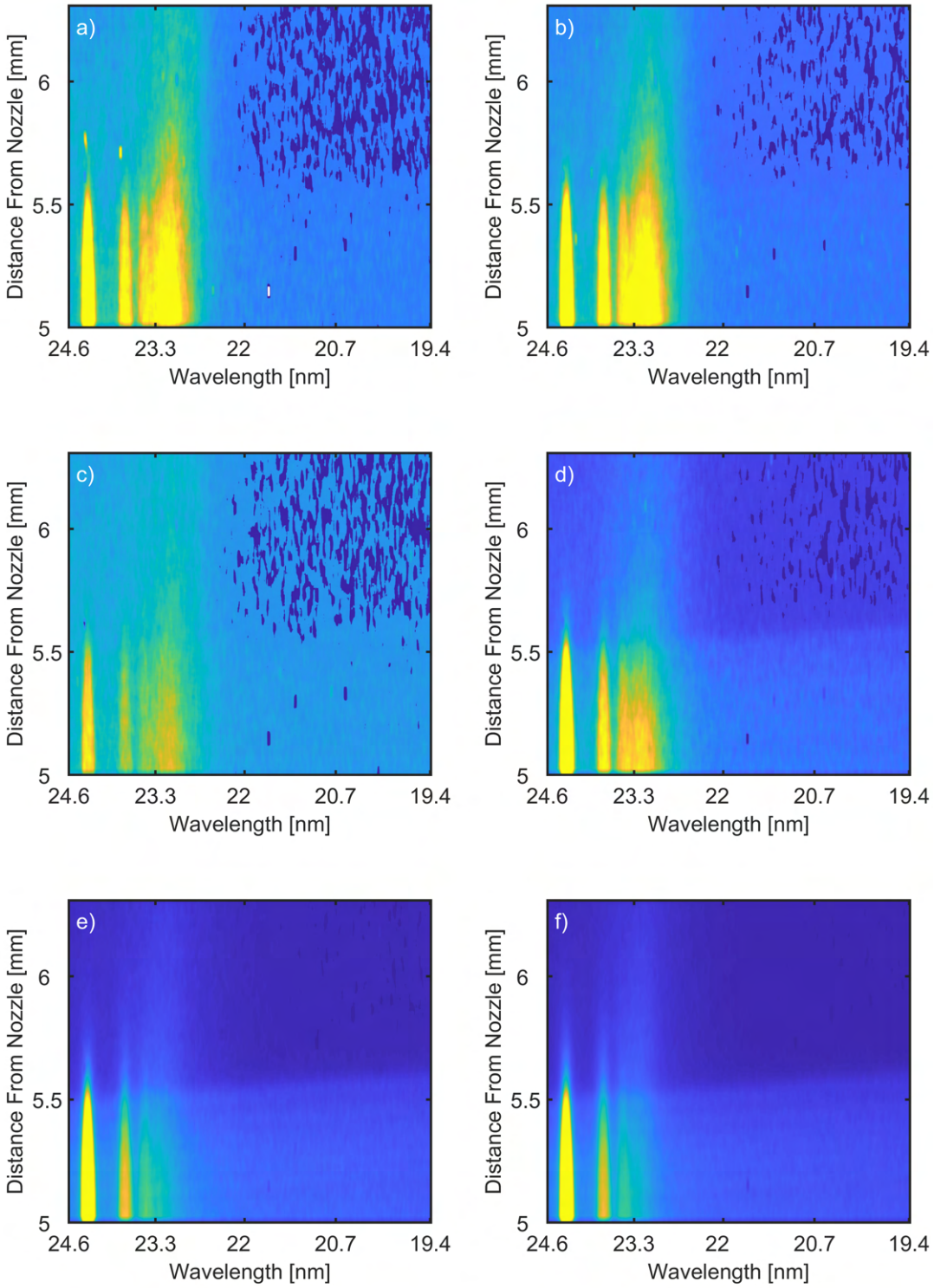

Fig. 4.16: Measured camera pictures for cluster beams with different average number of atoms generated at different temperatures of the cryostat: a) 7.5×10^6 atoms, b) 9.6×10^6 atoms, c) 5.9×10^7 atoms, d) 3.1×10^8 atoms, e) 1.6×10^{10} atoms, f) more than 1.6×10^{10} atoms. The distance from the nozzle has increased compared to Figure 4.7, since the focus was positioned 5 mm away from the nozzle in these measurements.

Much more surprising is the second finding. When the number of optical cycles in the laser-cluster interaction is reduced by a factor of 7.3, the XUV cluster continuum shows up at much smaller cluster sizes (7.5×10^6 atoms as opposed to 2.6×10^9 atoms). Furthermore, there exists an optimal cluster size at which the XUV cluster continuum is strongest relative to the strength of the fluorescence lines. This is shown in Figure 4.17, where the relative signal strength of the cluster continuum and the 3*p*-fluorescence line is plotted as a function of the temperature of the cryostat, i.e. the cluster size. Different from the previous results discussed in chapter 4 this figure does not use cluster size as the variable, since no size calibration is available in the literature for temperatures below 5.5 K (1.6×10^{10} Atoms). Here the maximum for the relative signal strength is observed in contrast to the 180 fs laser pulse interaction at a central wavelength of 1030nm. In the later measurements the relative strength of the XUV cluster continuum kept increasing with larger and larger clusters up to the largest clusters our source could generate at T = 4 K (see Figure 4.14).

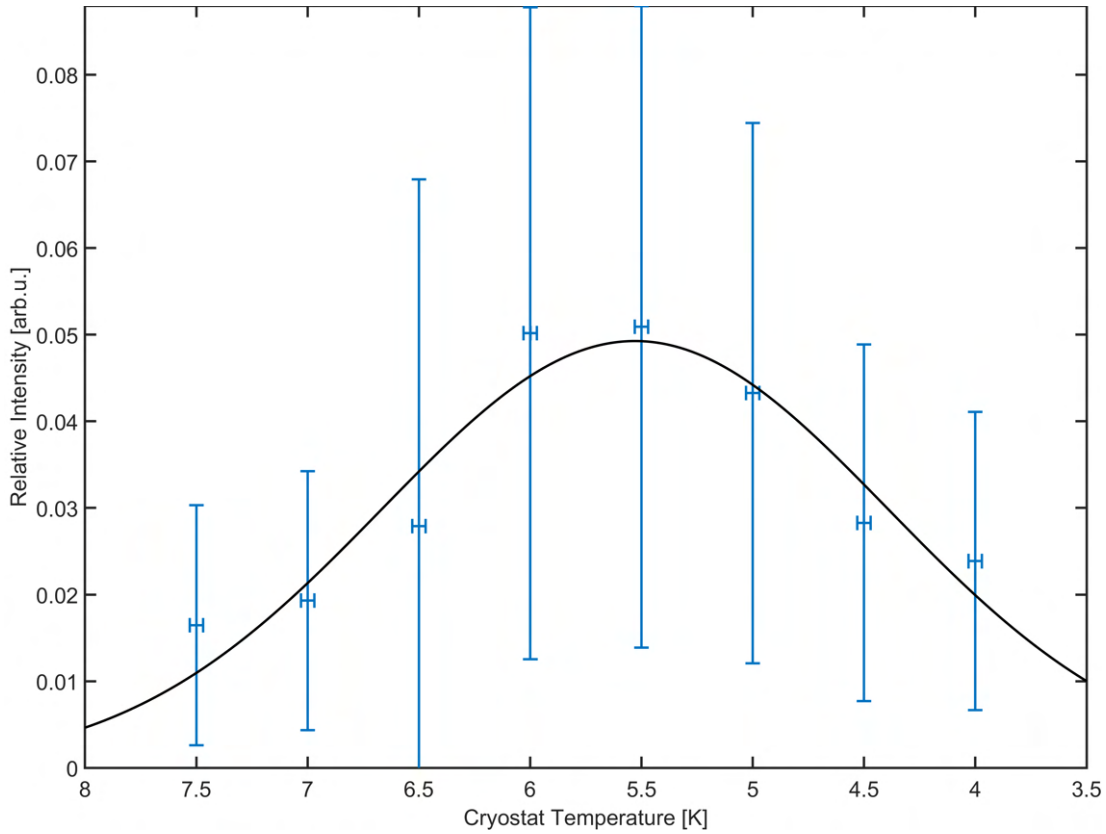

Fig. 4.17: Relative intensity of the XUV cluster continuum and the 3*p*-fluorescence line as a function of cryostat temperature with a guide to the eye in black. This figure uses cryostat temperature instead of average cluster size on the x-axis, since [77] only provides a temperature to size scaling down to 5.5 K (1.6×10^{10} atoms) and not below.

The change in the cluster size dependence of the XUV cluster continuum by three orders of magnitude when illuminating the clusters with significantly shorter pulses could point to a generation mechanism happening on a much shorter timescale than

the laser pulse duration, i.e. before a significant disintegration of the cluster has taken place. Looking back at the nanoplasma dynamics summarized in Figure 2.3, one sees that the cluster expansion can be separated into two phases. In the early phase ($< 50\,\mathrm{fs}$) the cluster starts to expand very slowly, while the electron temperature rises steadily. In the disintegration phase ($> 50\,\mathrm{fs}$) the electron temperature rises sharply due to the resonant heating condition being fulfilled, which causes the rapid increase in the cluster radius. The time it takes until the resonant heating condition is fulfilled increases with the average size of the clusters, as we have observed and discussed in section 4.3. This is equivalent to the early phase (slow expansion) lasting longer. Since the duration of the laser pulses remains unchanged, the result is that a larger fraction of the laser pulse energy interacts with the cluster during the early phase. This would explain why the XUV cluster continuum requires large clusters when generated with 180 fs pulses to show up. It is because the cluster size would need to be large enough to sufficiently delay the fast disintegration phase for the 180 fs long pulses to mostly interact with the rather intact cluster during its early phase. With the 50 fs pulses this requirement is lessened, since the duration of the pulses is short with respect to the overall nanoplasma dynamics. In addition, the switch from a laser with a central wavelength of 1030 nm to 2060 nm obviously results in the frequency of the light being halved. This trivial aspect has important implications. It means that the time at which resonant heating of the nanoplasma sets in ($\omega_{las} = \omega_{Mie}$) is significantly delayed (see subsection 2.3.2). The consequence is a longer early phase with a rather intact cluster, since the cluster needs to expand to a larger size, before resonant heating sets in. As a result, smaller clusters would have most of the energy of the shorter pulses interact with them during the early phase despite their much smaller size and therefore shorter early phase, since the other factor more than compensate.

This hypothesis of an XUV continuum generation process in helium clusters on a timescale comparable or shorter than the laser pulse duration would also agree with the experimental observation that in none of the pinhole camera measurements the continuum emission shows any vertical extension. This indicates a process that is significantly faster than any fluorescence processes ($\ll 300\,\mathrm{ps}$). However, it is clear that more measurements (see section 4.4) and theoretical support are necessary in order to formulate a proper model explaining the XUV cluster continuum generation and its properties.

Chapter 5

Conclusion

Utilising fluorescence spectroscopy to investigate energy absorption and dissipation in helium clusters and large droplets irradiated with intense femtosecond laser pulses at wavelengths of either 1030 nm or 2060 nm has revealed a number of interesting phenomena. First of all, it is clearly observed, how the cluster environment opens up an additional relaxation pathway in the laser-generated nanoplasma via three-body recombination (TBR). This is shown in Figure 4.2 by comparing the emitted XUV-spectrum of clusters with that of atoms in the gas phase. Here, the nanoplasma-specific relaxation pathway results in the population of high-lying Rydberg states of helium ions, which radiatively decay to the ionic ground state resulting in a broadband emission of XUV photons. Our spectrometer setup, which also acts as a pinhole camera, allowed us to make qualitative statements about the relative time frame of the TBR relaxation pathway in a nanoplasma compared to the regular fluorescence decay also present in atomic helium gas. On the one hand, TBR takes significantly longer, since the cluster has to expand before high-lying Rydberg-states are efficiently populated by low-energy quasifree plasma electrons via TBR. On the other hand, lower-lying fluorescence states in irradiated helium atoms and clusters are populated during the drive laser interaction (see section 4.1). By varying the size of the clusters, we were able to study the size-dependent behavior of resonant plasma heating, since the TBR relaxation pathway is much more sensitive to the temperature of quasifree electrons than is regular fluorescence from thermal excitation of the electronically excited states (see section 4.2). We were able to corroborate the electron-temperature sensitivity of TBR by influencing the resonant heating condition using different laser pulse parameters. In these experiments, we observed the same increase in the prevalence of TBR relaxation compared to regular fluorescence once the resonant heating condition is optimally fulfilled (see section 4.3). For the largest clusters we could generate ($> 1.6 \times 10^9$ atoms) a new XUV cluster continuum and we studied its properties to the best of the abilities of our current experimental setup (see section 4.4). We did not detect any light stemming from an HHG pro-

cess mediated by clusters (see section 4.5). However, when we switched to shorter drive laser pulses with twice the central wavelength and therefore far fewer cycles of the interacting electric field, the behavior of the XUV cluster continuum changed markedly. In this final experimental campaign, we were able to observe the cluster continuum even at sizes three orders of magnitude smaller than with the 180 fs long drive laser pulses. We hypothesised a qualitative model that may point towards the relevant timescales of the observed emission (see section 4.6). However, in the future much more investigative effort is needed both from an experimental but also from a theoretical side, in order to fully understand the origin of the novel XUV cluster continuum.

List of Figures

Bibliography

[1] V.P. Krainov and M.B. Smirnov. "Cluster beams in the super-intense femtosecond laser pulse". In: *Physics Reports* 370.3 (2002), pp. 237–331. ISSN: 0370-1573. DOI: https://doi.org/10.1016/S0370-1573(02)00272-7. URL: https://www.sciencedirect.com/science/article/pii/S0370157302002727.

[2] U. Saalmann, Ch. Siedschlag, and J.M. Rost. "Mechanisms of cluster ionization in strong laser pulses". In: *Journal of Physics B: Atomic, Molecular and Optical Physics* 39.4 (Jan. 2006), R39. DOI: 10.1088/0953-4075/39/4/R01. URL: https://dx.doi.org/10.1088/0953-4075/39/4/R01.

[3] Th. Fennel et al. "Laser-driven nonlinear cluster dynamics". In: *Rev. Mod. Phys.* 82 (2 June 2010), pp. 1793–1842. DOI: 10.1103/RevModPhys.82.1793. URL: https://link.aps.org/doi/10.1103/RevModPhys.82.1793.

[4] S.R. Krishnan et al. "Photoionization of clusters in intense few-cycle near infrared femtosecond pulses". In: *Phys. Chem. Chem. Phys.* 16 (19 2014), pp. 8721–8730. DOI: 10.1039/C3CP55380A. URL: http://dx.doi.org/10.1039/C3CP55380A.

[5] B. Schütte et al. "Strong-field ionization of clusters using two-cycle pulses at 1.8 μm". In: *Scientific Reports* 6.1 (Dec. 2016), p. 39664. ISSN: 2045-2322. DOI: 10.1038/srep39664. URL: https://doi.org/10.1038/srep39664.

[6] H. Wabnitz et al. "Multiple ionization of atom clusters by intense soft X-rays from a free-electron laser". In: *Nature* 420.6915 (Dec. 2002), pp. 482–485. ISSN: 1476-4687. DOI: 10.1038/nature01197. URL: https://doi.org/10.1038/nature01197.

[7] J. Schulz et al. "Energy absorption of free rare gas clusters irradiated by intense VUV pulses of a free electron laser". In: *Nuclear Instruments and Methods in Physics Research Section A: Accelerators, Spectrometers, Detectors and Associated Equipment* 507.1 (2003). Proceedings of the 24th International Free Electron Laser Conference and the 9th Users Workshop., pp. 572–576. ISSN: 0168-9002. DOI: https://doi.org/10.1016/S0168-9002(03)00923-9. URL: https://www.sciencedirect.com/science/article/pii/S0168900203009239.

[8] T. Laarmann et al. “Interaction of argon clusters with intense VUV-laser radiation: the role of electronic structure in the energy-deposition process”. In: *Phys. Rev. Lett.* 92 (14 Apr. 2004), p. 143401. DOI: 10.1103/PhysRevLett.92.143401. URL: https://link.aps.org/doi/10.1103/PhysRevLett.92.143401.

[9] T. Laarmann et al. “Emission of thermally activated electrons from rare gas clusters irradiated with intense VUV light pulses from a free electron laser”. In: *Phys. Rev. Lett.* 95 (6 Aug. 2005), p. 063402. DOI: 10.1103/PhysRevLett.95.063402. URL: https://link.aps.org/doi/10.1103/PhysRevLett.95.063402.

[10] M. Hoener et al. “Charge recombination in soft x-ray laser produced nanoplasmas”. In: *Journal of Physics B: Atomic, Molecular and Optical Physics* 41.18 (Sept. 2008), p. 181001. DOI: 10.1088/0953-4075/41/18/181001. URL: https://doi.org/10.1088/0953-4075/41/18/181001.

[11] C. Bostedt et al. “Ultrafast x-ray scattering of xenon nanoparticles: imaging transient states of matter”. In: *Phys. Rev. Lett.* 108 (9 Feb. 2012), p. 093401. DOI: 10.1103/PhysRevLett.108.093401. URL: https://link.aps.org/doi/10.1103/PhysRevLett.108.093401.

[12] H. Thomas et al. “Explosions of Xenon Clusters in Ultraintense Femtosecond X-Ray Pulses from the LCLS Free Electron Laser”. In: *Phys. Rev. Lett.* 108 (13 Mar. 2012), p. 133401. DOI: 10.1103/PhysRevLett.108.133401. URL: https://link.aps.org/doi/10.1103/PhysRevLett.108.133401.

[13] T. Gorkhover et al. “Nanoplasma Dynamics of Single Large Xenon Clusters Irradiated with Superintense X-Ray Pulses from the Linac Coherent Light Source Free-Electron Laser”. In: *Phys. Rev. Lett.* 108 (24 June 2012), p. 245005. DOI: 10.1103/PhysRevLett.108.245005. URL: https://link.aps.org/doi/10.1103/PhysRevLett.108.245005.

[14] E. Springate et al. “Electron kinetic energy measurements from laser irradiation of clusters”. In: *Phys. Rev. A* 68 (5 Nov. 2003), p. 053201. DOI: 10.1103/PhysRevA.68.053201. URL: https://link.aps.org/doi/10.1103/PhysRevA.68.053201.

[15] E.M. Snyder, S.A. Buzza, and A.W. Castleman Jr. “Intense field-matter interactions: multiple ionization of clusters”. In: *Phys. Rev. Lett.* 77 (16 Sept. 1996), pp. 3347–3350. DOI: 10.1103/PhysRevLett.77.3347. URL: https://link.aps.org/doi/10.1103/PhysRevLett.77.3347.

[16] M. Lezius et al. “Explosion dynamics of rare gas clusters in strong laser fields”. In: *Phys. Rev. Lett.* 80 (2 Jan. 1998), pp. 261–264. DOI: 10.1103/PhysRevLett.80.261. URL: https://link.aps.org/doi/10.1103/PhysRevLett.80.261.

[17] A. McPherson et al. “Multiphoton-induced x-ray emission at 4–5 keV from Xe atoms with multiple core vacancies”. In: *Nature* 370.6491 (Aug. 1994), pp. 631–634. ISSN: 1476-4687. DOI: 10.1038/370631a0. URL: https://doi.org/10.1038/370631a0.

[18] T. Ditmire et al. “Nuclear fusion from explosions of femtosecond laser-heated deuterium clusters”. In: *Nature* 398.6727 (Apr. 1999), pp. 489–492. ISSN: 1476-4687. DOI: 10.1038/19037. URL: https://doi.org/10.1038/19037.

[19] B. Schütte et al. “Low-energy electron emission in the strong-field ionization of rare gas clusters”. In: *Phys. Rev. Lett.* 121 (6 Aug. 2018), p. 063202. DOI: 10.1103/PhysRevLett.121.063202. URL: https://link.aps.org/doi/10.1103/PhysRevLett.121.063202.

[20] B. Schütte et al. “Observation of correlated electronic decay in expanding clusters triggered by near-infrared fields”. In: *Nature Communications* 6.1 (Oct. 2015), p. 8596. ISSN: 2041-1723. DOI: 10.1038/ncomms9596. URL: https://doi.org/10.1038/ncomms9596.

[21] M. Kelbg et al. “Auger emission from the Coulomb explosion of helium nanoplasmas”. In: *The Journal of Chemical Physics* 150.20 (2019), p. 204302. DOI: 10.1063/1.5089943. eprint: https://doi.org/10.1063/1.5089943. URL: https://doi.org/10.1063/1.5089943.

[22] B. Schütte et al. “Tracing electron-ion recombination in nanoplasmas produced by extreme-ultraviolet irradiation of rare-gas clusters”. In: *Phys. Rev. Lett.* 112 (25 June 2014), p. 253401. DOI: 10.1103/PhysRevLett.112.253401. URL: https://link.aps.org/doi/10.1103/PhysRevLett.112.253401.

[23] Y. Hahn. “Electron - ion recombination processes - an overview”. In: *Reports on Progress in Physics* 60.7 (July 1997), p. 691. DOI: 10.1088/0034-4885/60/7/001. URL: https://dx.doi.org/10.1088/0034-4885/60/7/001.

[24] P. Mansbach and J. Keck. “Monte carlo trajectory calculations of atomic excitation and ionization by thermal electrons”. In: *Phys. Rev.* 181 (1 May 1969), pp. 275–289. DOI: 10.1103/PhysRev.181.275. URL: https://link.aps.org/doi/10.1103/PhysRev.181.275.

[25] S. X. Hu. “Three-body recombination of atomic ions with slow electrons”. In: *Phys. Rev. Lett.* 98 (13 Mar. 2007), p. 133201. DOI: 10.1103/PhysRevLett.98.133201. URL: https://link.aps.org/doi/10.1103/PhysRevLett.98.133201.

[26] H. Buchenau et al. “Mass spectra and time-of-flight distributions of helium cluster beams”. In: *The Journal of Chemical Physics* 92.11 (1990), pp. 6875–6889. DOI: 10.1063/1.458275. eprint: https://doi.org/10.1063/1.458275. URL: https://doi.org/10.1063/1.458275.

[27] F. Della Sala and A. Görling. “Excitation energies of molecules by time-dependent density functional theory based on effective exact exchange Kohn–Sham potentials”. In: *International Journal of Quantum Chemistry* 91.2 (2003), pp. 131–138. DOI: https://doi.org/10.1002/qua.10425. eprint: https://onlinelibrary.wiley.com/doi/pdf/10.1002/qua.10425. URL: https://onlinelibrary.wiley.com/doi/abs/10.1002/qua.10425.

[28] L. ç Serra and A. Rubio. “Core polarization in the optical response of metal clusters: generalized time-dependent density-functional theory”. In: *Phys. Rev. Lett.* 78 (8 Feb. 1997), pp. 1428–1431. DOI: 10.1103/PhysRevLett.78.1428. URL: https://link.aps.org/doi/10.1103/PhysRevLett.78.1428.

[29] F. Fehrer et al. “Linear and non-linear response of embedded Na clusters”. In: *Applied Physics A* 82.1 (Jan. 2006), pp. 151–159. ISSN: 1432-0630. DOI: 10.1007/s00339-005-3353-7. URL: https://doi.org/10.1007/s00339-005-3353-7.

[30] E. Giglio, E. Suraud, and P.-G. Reinhard. “Semi-classical description of ionic and electronic dynamics in metal clusters”. In: *Annalen der Physik* 514.4 (2002), pp. 291–308. DOI: https://doi.org/10.1002/andp.20025140402. eprint: https://onlinelibrary.wiley.com/doi/pdf/10.1002/andp.20025140402. URL: https://onlinelibrary.wiley.com/doi/abs/10.1002/andp.20025140402.

[31] T. Fennel, G.F. Bertsch, and K.-H. Meiwes-Broer. “Ionization dynamics of simple metal clusters in intense fields by the Thomas-Fermi-Vlasov method”. In: *The European Physical Journal D - Atomic, Molecular, Optical and Plasma Physics* 29.3 (June 2004), pp. 367–378. ISSN: 1434-6079. DOI: 10.1140/epjd/e2004-00035-1. URL: https://doi.org/10.1140/epjd/e2004-00035-1.

[32] J. Köhn et al. “Non-resonant absorption enhancement in laser-excited simple metal clusters through electron-electron collisions”. In: *Phys. Rev. A* 77 (3 Mar. 2008), p. 033202. DOI: 10.1103/PhysRevA.77.033202. URL: https://link.aps.org/doi/10.1103/PhysRevA.77.033202.

[33] C. Rose-Petruck et al. “Ultrafast electron dynamics and inner-shell ionization in laser driven clusters”. In: *Phys. Rev. A* 55 (2 Feb. 1997), pp. 1182–1190. DOI: 10.1103/PhysRevA.55.1182. URL: https://link.aps.org/doi/10.1103/PhysRevA.55.1182.

[34] I. Last and J. Jortner. “Quasiresonance ionization of large multicharged clusters in a strong laser field”. In: *Phys. Rev. A* 60 (3 Sept. 1999), pp. 2215–2221. DOI: 10.1103/PhysRevA.60.2215. URL: https://link.aps.org/doi/10.1103/PhysRevA.60.2215.

[35] K. Ishikawa and T. Blenski. “Explosion dynamics of rare-gas clusters in an intense laser field”. In: *Phys. Rev. A* 62 (6 Nov. 2000), p. 063204. DOI: 10.1103/PhysRevA.62.063204. URL: https://link.aps.org/doi/10.1103/PhysRevA.62.063204.

[36] C. Siedschlag and J.M. Rost. “Enhanced ionization in small rare-gas clusters”. In: *Phys. Rev. A* 67 (1 Jan. 2003), p. 013404. DOI: 10.1103/PhysRevA.67.013404. URL: https://link.aps.org/doi/10.1103/PhysRevA.67.013404.

[37] T. Fennel, L. Ramunno, and T. Brabec. “Highly charged ions from laser-cluster interactions: local-field-enhanced impact ionization and frustrated electron-ion recombination”. In: *Phys. Rev. Lett.* 99 (23 Dec. 2007), p. 233401. DOI: 10.1103/PhysRevLett.99.233401. URL: https://link.aps.org/doi/10.1103/PhysRevLett.99.233401.

[38] T. Ditmire et al. “Interaction of intense laser pulses with atomic clusters”. In: *Phys. Rev. A* 53 (5 May 1996), pp. 3379–3402. DOI: 10.1103/PhysRevA.53.3379. URL: https://link.aps.org/doi/10.1103/PhysRevA.53.3379.

[39] H.M. Milchberg, S.J. McNaught, and E. Parra. “Plasma hydrodynamics of the intense laser-cluster interaction”. In: *Phys. Rev. E* 64 (5 Oct. 2001), p. 056402. DOI: 10.1103/PhysRevE.64.056402. URL: https://link.aps.org/doi/10.1103/PhysRevE.64.056402.

[40] C. Jungreuthmayer et al. “Intense VUV laser cluster interaction in the strong coupling regime”. In: *Journal of Physics B: Atomic, Molecular and Optical Physics* 38 (2005), pp. 3029–3036.

[41] D. Buchta et al. “Extreme ultraviolet ionization of pure He nanodroplets: Mass-correlated photoelectron imaging, Penning ionization, and electron energy-loss spectra”. In: *The Journal of Chemical Physics* 139.8 (2013), p. 084301. DOI: 10.1063/1.4818531. eprint: https://doi.org/10.1063/1.4818531. URL: https://doi.org/10.1063/1.4818531.

[42] B. Schütte et al. “Rare-gas clusters in intense extreme-ultraviolet pulses from a high-order harmonic source”. In: *Phys. Rev. Lett.* 112 (7 Feb. 2014), p. 073003. DOI: 10.1103/PhysRevLett.112.073003. URL: https://link.aps.org/doi/10.1103/PhysRevLett.112.073003.

[43] M.V. Ammosov, N.B. Delone, and V.P. Krainov. “Tunnel ionization of complex atoms and of atomic ions in an alternating electromagnetic field”. In: *Jetp Letters* (1986).

[44] L.V. Keldysh. "Ionization in the field of a strong electromagnetic wave". In: *J. Exp. Theor. Phys.* 20.5 (1965), pp. 1307–1314.

[45] V. Véniard, R. Taieb, and A. Maquet. "Atomic clusters submitted to an intense short laser pulse: A density-functional approach". In: *Phys. Rev. A* 65 (1 Dec. 2001), p. 013202. DOI: 10.1103/PhysRevA.65.013202. URL: https://link.aps.org/doi/10.1103/PhysRevA.65.013202.

[46] C. Siedschlag and J.M. Rost. "Electron release of rare-gas atomic clusters under an intense laser pulse". In: *Phys. Rev. Lett.* 89 (17 Oct. 2002), p. 173401. DOI: 10.1103/PhysRevLett.89.173401. URL: https://link.aps.org/doi/10.1103/PhysRevLett.89.173401.

[47] V.P. Krainov. "Inverse stimulated bremsstrahlung of slow electrons under Coulomb scattering". In: *Journal of Physics B: Atomic, Molecular and Optical Physics* 33.8 (Apr. 2000), p. 1585. DOI: 10.1088/0953-4075/33/8/309. URL: https://dx.doi.org/10.1088/0953-4075/33/8/309.

[48] M. Brack. "The physics of simple metal clusters: self-consistent jellium model and semiclassical approaches". In: *Rev. Mod. Phys.* 65 (3 July 1993), pp. 677–732. DOI: 10.1103/RevModPhys.65.677. URL: https://link.aps.org/doi/10.1103/RevModPhys.65.677.

[49] P.-G. Reinhard and E. Suraud. "Field amplification in Na clusters". In: *The European Physical Journal D - Atomic, Molecular, Optical and Plasma Physics* 3.2 (Aug. 1998), pp. 175–178. ISSN: 1434-6079. DOI: 10.1007/s100530050161. URL: https://doi.org/10.1007/s100530050161.

[50] Th. Fennel et al. "Plasmon-enhanced electron acceleration in intense laser metal-cluster interactions". In: *Phys. Rev. Lett.* 98 (14 Apr. 2007), p. 143401. DOI: 10.1103/PhysRevLett.98.143401. URL: https://link.aps.org/doi/10.1103/PhysRevLett.98.143401.

[51] Y. Hahn. "Electron - ion recombination processes - an overview". In: *Reports on Progress in Physics* 60.7 (July 1997), pp. 691–759. DOI: 10.1088/0034-4885/60/7/001. URL: https://doi.org/10.1088/0034-4885/60/7/001.

[52] M. Stobbe. "Zur Quantenmechanik photoelektrischer Prozesse". In: *Annalen der Physik* 399.6 (1930), pp. 661–715. DOI: https://doi.org/10.1002/andp.19303990604. eprint: https://onlinelibrary.wiley.com/doi/pdf/10.1002/andp.19303990604. URL: https://onlinelibrary.wiley.com/doi/abs/10.1002/andp.19303990604.

[53] L.H. Andersen and J. Bolko. "Radiative recombination between fully stripped ions and free electrons". In: *Phys. Rev. A* 42 (3 Aug. 1990), pp. 1184–1191. DOI: 10.1103/PhysRevA.42.1184. URL: https://link.aps.org/doi/10.1103/PhysRevA.42.1184.

[54] R. Trebino et al. “Measuring ultrashort laser pulses in the time-frequency domain using frequency-resolved optical gating”. In: *Review of Scientific Instruments* 68.9 (1997), pp. 3277–3295.

[55] C. Iaconis and I.A. Walmsley. “Spectral phase interferometry for direct electric-field reconstruction of ultrashort optical pulses”. In: *Optics letters* 23.10 (1998), pp. 792–794.

[56] V.V. Lozovoy, I. Pastirk, and M. Dantus. “Multiphoton intrapulse interference. IV. Ultrashort laser pulse spectral phase characterization and compensation”. In: *Optics letters* 29.7 (2004), pp. 775–777.

[57] R.W. Boyd and D. Prato. *Nonlinear Optics*. Elsevier Science, 2008. ISBN: 9780080485966. URL: https://books.google.de/books?id=uoRUi1Yb7ooC.

[58] A. Dubietis, A. Couairon, and G. Genty. “Supercontinuum generation: introduction”. In: *J. Opt. Soc. Am. B* 36.2 (Feb. 2019), SG1–SG3. DOI: 10.1364/JOSAB.36.000SG1. URL: http://josab.osa.org/abstract.cfm?URI=josab-36-2-SG1.

[59] P.B. Corkum. “Plasma perspective on strong field multiphoton ionization”. In: *Physical review letters* 71.13 (1993), p. 1994.

[60] M. Lewenstein et al. “Theory of high-harmonic generation by low-frequency laser fields”. In: *Physical Review A* 49.3 (1994), p. 2117.

[61] S. Hädrich et al. “Single-pass high harmonic generation at high repetition rate and photon flux”. In: *Journal of Physics B: Atomic, Molecular and Optical Physics* 49.17 (Aug. 2016), p. 172002. DOI: 10.1088/0953-4075/49/17/172002. URL: https://dx.doi.org/10.1088/0953-4075/49/17/172002.

[62] J. Li et al. “53-attosecond X-ray pulses reach the carbon K-edge”. In: *Nature Communications* 8.1 (Aug. 2017), p. 186. ISSN: 2041-1723. DOI: 10.1038/s41467-017-00321-0. URL: https://doi.org/10.1038/s41467-017-00321-0.

[63] V. Cardin et al. “Self-channelled high harmonic generation of water window soft x-rays”. In: *Journal of Physics B: Atomic, Molecular and Optical Physics* 51.17 (Aug. 2018), p. 174004. DOI: 10.1088/1361-6455/aad49c. URL: https://dx.doi.org/10.1088/1361-6455/aad49c.

[64] F. Silva et al. “Spatiotemporal isolation of attosecond soft X-ray pulses in the water window”. In: *Nature Communications* 6.1 (Mar. 2015), p. 6611. ISSN: 2041-1723. DOI: 10.1038/ncomms7611. URL: https://doi.org/10.1038/ncomms7611.

[65] T. Popmintchev et al. “Bright coherent ultrahigh harmonics in the keV x-ray regime from mid-infrared femtosecond lasers”. In: *Science (New York, N.Y.)* 336.6086 (June 2012), pp. 1287–1291. ISSN: 0036-8075. DOI: 10.1126/science.1218497. URL: https://doi.org/10.1126/science.1218497.

[66] J. Tate et al. “Scaling of wave-packet dynamics in an intense midinfrared field”. In: *Phys. Rev. Lett.* 98 (1 Jan. 2007), p. 013901. DOI: 10.1103/PhysRevLett.98.013901. URL: https://link.aps.org/doi/10.1103/PhysRevLett.98.013901.

[67] A.D. Shiner et al. “Wavelength scaling of high harmonic generation efficiency”. In: *Phys. Rev. Lett.* 103 (7 Aug. 2009), p. 073902. DOI: 10.1103/PhysRevLett.103.073902. URL: https://link.aps.org/doi/10.1103/PhysRevLett.103.073902.

[68] C. Vozzi et al. “Cluster effects in high-order harmonics generated by ultrashort light pulses”. In: *Applied Physics Letters* 86.11 (2005), p. 111121. DOI: 10.1063/1.1888053. eprint: https://doi.org/10.1063/1.1888053. URL: https://doi.org/10.1063/1.1888053.

[69] Y. Tao et al. “Cluster size dependence of high-order harmonic generation”. In: *New Journal of Physics* 19.8 (Aug. 2017), p. 083017. DOI: 10.1088/1367-2630/aa8029. URL: https://dx.doi.org/10.1088/1367-2630/aa8029.

[70] B. Bódi et al. “High harmonic generation on noble gas clusters”. In: *Opt. Express* 27.19 (Sept. 2019), pp. 26721–26727. DOI: 10.1364/OE.27.026721. URL: https://opg.optica.org/oe/abstract.cfm?URI=oe-27-19-26721.

[71] J. Rothhardt et al. “Absorption-limited and phase-matched high harmonic generation in the tight focusing regime”. In: *New Journal of Physics* 16.3 (2014), p. 033022.

[72] Z. Yin, T.T. Luu, and H.J. Wörner. “Few-cycle high-harmonic generation in liquids: in-operando thickness measurement of flat microjets”. In: *Journal of Physics: Photonics* 2.4 (Oct. 2020), p. 044007. DOI: 10.1088/2515-7647/abb0ef. URL: https://dx.doi.org/10.1088/2515-7647/abb0ef.

[73] T.T. Luu et al. “Extreme–ultraviolet high–harmonic generation in liquids”. In: *Nature Communications* 9.1 (Sept. 2018), p. 3723. ISSN: 2041-1723. DOI: 10.1038/s41467-018-06040-4. URL: https://doi.org/10.1038/s41467-018-06040-4.

[74] W. L. Wiese and J. R. Fuhr. “Accurate atomic transition probabilities for hydrogen, helium, and lithium”. In: *Journal of Physical and Chemical Reference Data* 38.3 (2009), pp. 565–720. DOI: 10.1063/1.3077727. eprint: https://doi.org/10.1063/1.3077727. URL: https://doi.org/10.1063/1.3077727.

[75] K.A. Janulewicz et al. “Broadband soft X-ray source from a clustered gas target dedicated to high-resolution XCT and X-ray absorption spectroscopy”. In: *Opt. Express* 30.26 (Dec. 2022), pp. 47867–47878. DOI: 10.1364/OE.477726. URL: https://opg.optica.org/oe/abstract.cfm?URI=oe-30-26-47867.

[76] A. von Wezyk et al. “Target materials for efficient plasma-based extreme ultraviolet sources in the range of 6 to 8 nm”. In: *Journal of Physics D: Applied Physics* 52.50 (Oct. 2019), p. 505202. DOI: 10.1088/1361-6463/ab4317. URL: https://dx.doi.org/10.1088/1361-6463/ab4317.

[77] L.F. Gomez et al. “Sizes of large He droplets”. In: *The Journal of Chemical Physics* 135.15 (2011), p. 154201. DOI: 10.1063/1.3650235. eprint: https://doi.org/10.1063/1.3650235. URL: https://doi.org/10.1063/1.3650235.

Acknowledgements

Special thanks to my current and former group members: Andreas Przystawik, Sergey Usenko, Samuel Hartwell, David Schwickert, Dian Diaman, Cheng Luo, Slawomir Skruszewicz, Mahesh Namboodiri, Markus Jakob, Daniel Junge, Ekaterina Izotova, Luis Carretero and Tim Laarmann as well as my coworkers from Class 5 Photonics: Phillip Merkl, Bastian Manschwetus, Mark Prandolini, Michael Schulz, Jan Heye Buss and Robert Riedel

Eidesstattliche Versicherung / Declaration on oath

Hiermit versichere ich an Eides statt, die vorliegende Dissertationsschrift selbst verfasst und keine anderen als die angegebenen Hilfsmittel und Quellen benutzt zu haben.

Hamburg, den April 1, 2023

Unterschrift des Doktoranden